DPhil. Thesis

Diabatic jet and storm track feedbacks

Henrik Stormark Auestad

Supervised by Professor Tim Woollings and Professor Paulo Ceppi

Balliol College

Atmospheric, Oceanic and Planetary Physics
Department of Physics
University of Oxford

Hillary 2026

Abstract

Condensation and freezing of water releases latent heat that influences the atmospheric circulation across a wide range of scales and through multiple mechanisms. On all scales, the precise location of latent heating is crucial in determining its effects. As the atmosphere warms, latent heating is expected to intensify, which makes it increasingly important to understand its role in the climate system. Yet we lack a theory that reconciles the many ways in which latent heating shapes the atmospheric circulation.

In this thesis, I take a step towards meeting this challenge by mapping the relationship between latent heating and atmospheric circulation across spatio-temporal scales. On synoptic scales, I identify an asymmetric dependence on meridional wind, with heating concentrated on the warm flank of the jet, energising the flow. In spatio-temporal averages, this asymmetry is smeared out, and the mean heating instead appears on the cold flank and therefore appears as an energy sink.

Diabatic heating enters the thermodynamic energy equation as a linear source term. It may therefore seem sufficient to diagnose the mean latent heating alone — as many studies have done — to assess the total effect of latent heating on the mean atmospheric circulation. However, because heating is itself coupled to the dynamics, it introduces a nonlinearity: latent heating depends on vertical velocity, which in turn depends on horizontal temperature advection, which is not accounted for when averaging.

Here, I use novel atmospheric general circulation model experiments to isolate the effects of coupled heating–dynamics interactions from those of climatological latent heating. I show that the nonlinear coupling between latent heating and the dynamics enhances climatic zonal asymmetries, increases the efficiency of eddy heat fluxes, intensifies the strongest storms by $\sim 20\%$, and sustains the peak intensity of the strongest storms despite baroclinicity weakening under global warming.

Statement of originality

This thesis is based on three peer-reviewed publications led by me, Henrik Auestad (H.A.), with contributions from Tim Woollings (T.W.), Paulo Ceppi (P.C.), Abel Shibu (A.S.), Clemens Spensberger (C.S.), Thomas Spengler (T.S.), and Andrea Marcheggiani (A.M.).

For Chapter 3, based on Auestad et al. (2024), H.A. conducted the data analysis, visualised the results, and prepared the original draft. C.S. provided the cross-sections of the instantaneous two-dimensional jets and the infrastructure required to compute the 10-day low-pass jets. H.A., T.W., P.C., C.S., T.S., and A.M. contributed to the conceptualisation of the study, as well as to the review and editing of the manuscript.

For Chapters 4–5, based on Auestad et al. (2025) and Auestad et al. (accepted; npj Climate and Atmospheric Science), H.A. set up and ran the model experiments, conducted the data analysis, visualised the results, and wrote the original draft. A.S. tracked cyclones and computed the cyclone potential vorticity composites. H.A., P.C., and T.W. conceptualised the studies and reviewed the manuscripts. A.S. also contributed to reviewing the manuscript on which Chapter 5 is based.

Acknowledgements

First of all, Tim Woollings and Paulo Ceppi, thank you for the brilliant supervision. I have really enjoyed doing this degree. I am greatly appreciative of your support, patience, fun and fruitful research ideas, willingness to stretch a travel budget, and thoughtful consideration for working from home during the ski season. I also think the research came out alright. Five stars.

It has been great spending the past few years at AOPP, all due to the fantastic people there; from the research group, Matt, Rob, Rhid, and Scott, to name a few. I must also thank my co-authors who contributed to the research in this thesis. Thank you, Abel Shibu, Clemens Spensberger, Andrea Marcheggiani, and Thomas Spengler. Also, thank you, Thomas and Camille Li, for welcoming me at GFI when I have been in Bergen.

College has been an absolute rollercoaster. Thank you to all my eccentric friends in Balliol, including everyone who came sailing and skiing, and everyone yet to come, Harry and the Band, the Megaron: former, present, and future bar managers, all Megaron Olympics athletes and those who have memorial disciplines named after them; pre-mortem, the Holywell Manor Barbecue and Booker, Balliol Fine Pictures, the night porters Steve and Mark, the Japanese Empress, and everyone else.

Thank you to Norwegian taxpayers who make higher education possible for everyone in Norway, and to Aker Scholarship, which made coming to Oxford possible for me.

Last but not least, thank you to my parents, grandparents, Øyvind, and Karen; you are simply amazing from A to Å. Thank you, Calouste, and family in London, for always keeping me updated on the latest about swords, catapults, and the Gauls. And thank you, Lisa. You are incredible, absolutely invaluable, and ”hel ved”.

Contents

List of Tables

List of Figures

Chapter 1

Introduction

The fundamental theories of mid-latitude atmospheric dynamics, mostly developed in the 20th century, consider a dry atmosphere: unaffected by water, in particular ignoring the diabatic heating and cooling associated with phase transitions between water vapour, liquid water, and ice. Such diabatic effects were not deemed unimportant, but they complicate the governing equations, thereby making the equations more opaque and making simple theories harder to extract from the equations alone. With the advent of enhanced computational power and improved observations, considerable effort has been invested over the past 30 years in modelling experiments and advanced data analysis to understand the effects of diabatic heating and cooling on weather and climate in the mid-latitudes. These efforts aim to close the gap between dry dynamical theory and observations.

Moisture in the mid-latitude atmosphere can be thought of as seasoning added to a dish representing the dry dynamics. It is not clear, however, whether this seasoning provides a subtle flavour or dominates the flavours of the dish. As temperatures increase and more water vapour is circulated in the atmosphere, it is likely that the seasoning becomes increasingly flavourful.

In this thesis, I examine how latent heating, the heat released when water vapour condenses, affects the mid-latitude atmospheric circulation. In Chapter 2, I describe essential aspects of dry atmospheric dynamics, providing the context in which I will examine the role of moisture. I then discuss aspects of moist atmospheric dynamics that are relevant to the scientific work presented in this thesis. This thesis is based on the following three publications.

In Auestad et al. (2024), described in Chapter 3, we show that latent heating is concentrated where the jet stream transports warm, moist air poleward. This heating sharpens the jet and amplifies upper-tropospheric waves, implying a coupled relationship between the heating and the dynamics. This coupling has been overlooked in some previous attempts to understand the impact of latent heating on climate.

In Auestad et al. (2025), described in Chapter 4, we present a new modelling experiment that demonstrates how the coupling between latent heating and the dynamics shapes climate. The coupling strengthens storms and promotes their poleward propagation. Our results suggest that inadequate representation of this coupling contributes to long-standing biases in climate models.

In Auestad et al. (2026), described in Chapter 5, we quantify the effect of the coupling between latent heating and the dynamics on storm intensity and eddy kinetic energy in a global warming experiment. Latent heating affects storm intensity both through direct amplification and through changes to the environmental conditions for storm growth. In this study, we approximately isolate the former effect and quantify its contribution to changes in storm intensity as the atmosphere warms and the hydrological cycle intensifies.

In Chapter 6, I synthesise, contextualise, and criticise the scientific work of Chapters 3-5, before I give an outlook.

Chapter 2

Background

The Background section is written with the help of Pedlosky (1987) and Vallis (2017) — unless cited otherwise.

2.1 Basic equations and scales of motion

2.1.1 Assumptions

Motion in the ocean and atmosphere is, to a good approximation, described as (i) locally hydrostatic: the vertical gradient in pressure is balanced by gravity and (ii) shallow: horizontal motion is orders of magnitude larger than vertical motion. By assuming (i), (ii), and the fluid in question to be inviscid, the atmospheric and oceanic equations of motion reduce to the inviscid primitive equations of motion

$$\frac{\partial \boldsymbol{u}}{\partial t} + (\boldsymbol{u}_3 \cdot \nabla_z)\boldsymbol{u} + f(\boldsymbol{k} \times \boldsymbol{u}) = -\frac{1}{\rho}\nabla_z p, \tag{2.1}$$

$$\frac{\partial p}{\partial z} = -\rho g, \tag{2.2}$$

$$\frac{\partial \rho}{\partial t} + \nabla \cdot (\rho \boldsymbol{u_3}) = 0, \tag{2.3}$$

where $\boldsymbol{u}$ equals the horizontal velocity vector $(u, v, 0)$, $\boldsymbol{u}_3$ the full three dimensional velocity vector (u, v, w), k is the vertical unit vector, ρ is the density, ∇ is the gradient operator and ∇_z is the gradient operator evaluated at constant height, p is pressure, and g is the gravitational acceleration, $f = 2\Omega \sin(\phi)$ is the Coriolis frequency, where Ω is the rotation rate of the Earth and ϕ is the latitudinal coordinate (Vallis 2017).

Equation 2.1 is the horizontal momentum equation, Eq. 2.2 is hydrostatic balance and figures as the vertical momentum equation, and Eq. 2.3 is the mass conservation equation.

Whether (i) and (ii) [and therefore Eq. 2.1–2.3] are good approximations depend on the *aspect ratio*, which is the characteristic vertical length scale L divided by the characteristic horizontal length scale H, H/L. In the atmosphere, mid-latitude *large-scale* motion has a characteristic horizontal length scale of $L \sim 1000$ km. The troposphere height H is ~ 10 km; thus (i) and (ii) are good approximations as the aspect ratio is small.

To show why a small aspect ratio justifies (ii), we assume that the fluid is incompressible (although the same result can be obtained from the weaker *Boussinesq* assumption). For an incompressible fluid, conservation of mass, Eq. 2.3, yields

$$\nabla \cdot \boldsymbol{u} + \frac{\partial w}{\partial z} = 0. \tag{2.4}$$

The first term scale as U/L and the second term as W/H, where U and W are the characteristic horizontal and vertical velocities, respectively. From mass conservation of an incompressible fluid, the characteristic magnitude of W is therefore $W = (H/L)U$. Thus, for small aspect ratios, the vertical velocities are small compared to the horizontal velocities and (ii) is justified (Vallis 2017).

A similar scaling argument applied to the vertical momentum equation shows that

$(H/L)^2$ is proportional to the advective terms divided with the vertical pressure gradient term. A small aspect ratio therefore implies that the latter term largely balances the gravity and (i) is justified (Vallis 2017).

Whether (i) is true in a stratified fluid also depends on the Froude number, which compares the horizontal motion to the stratification over the fluid depth. A small Froude number implies that the vertical stratification suppresses the vertical motion (Vallis 2017). Again, (i) and (ii) both remain valid for L, H, and the typical mid-latitude stratification. This exercise can be repeated for oceanic scales of motion and stratification, but this thesis focuses on the atmosphere.

2.1.2 Rossby number

In addition to the characteristic horizontal length scale, L, we defined the characteristic horizontal velocity, $U \sim 10$ m s^{-1}, and we define the advective timescale, $L/U = 10^5$ s $\sim$ 1 day. The first two terms in Eq. 2.1 thus scale as

$$\frac{U^2}{L} \sim 10^{-4} \text{ m s}^{-2}, \tag{2.5}$$

while the third term scales as

$$fU \sim 10^{-3} \text{ m s}^{-2}, \tag{2.6}$$

where the Coriolis term $f \sim 10^{-4}$ s^{-1}. The third term is an order of magnitude larger than the first two terms and must therefore be balanced by the fourth term in Eq. 2.1, the pressure gradient term. The ratio of (2.5) and (2.6) yields the non-dimensional Rossby number,

$$Ro = \frac{U}{fL}, \tag{2.7}$$

that expresses the ratio of inertial forces to rotation. The Rossby number is inversely proportional to the Coriolis parameter. The inertial forces therefore dominate close to the equator, where f is small. The Coriolis parameter f increases towards the poles; for large-scale atmospheric flow in the mid-latitudes, $Ro \sim 10^{-1}$, and rotation dominates the inertial forces (Vallis 2017).

2.2 The Rossby radius of deformation

The Rossby radius of deformation (R_d) is an important length scale and a fascinating quantity that appears explicitly in many rotating fluids problems including gravity.

2.2.1 Shallow water

In the shallow water equations, which describe an inviscid fluid with constant, uniform density, whose horizontal motion occurs on length scales far larger than the depth of the fluid, the Rossby radius of deformation is

$$R_d = \frac{\sqrt{gH}}{f}, \tag{2.8}$$

where g is the gravitational acceleration, H is the depth of the shallow-water layer and f is, as before, the Coriolis frequency, or planetary vorticity. Thus, R_d is the ratio of the shallow water gravity wave speed to the Coriolis parameter. The shallow water R_d is the horizontal distance over which the pressure gradient force balances the Coriolis force (Holton and Hakim 2013; also discussed below),

$$f v_g = \frac{1}{\rho} \frac{\partial p}{\partial x}\bigg|_z, \tag{2.9}$$

$$f u_g = -\frac{1}{\rho}\frac{\partial p}{\partial y}\bigg|_z, \tag{2.10}$$

where u_g and v_g are the zonal and meridional geostrophic winds (Vallis 2017). This relationship is called geostrophic balance and is the lowest energy state (potential + kinetic energy) of the linearised shallow water equations (Vallis 1992). Geostrophic balance dominate the extratropical atmosphere, where the Rossby number is small.

Geostrophic adjustment

In the shallow-water approximation, the pressure gradients are expressed as gradients in surface elevation. In the real atmosphere, the net radiative heating at the equator and the net cooling at the poles cause large and initially unbalanced pressure gradients. The rotation of the system ensures that unbalanced pressure gradients settle into geostrophic balance. This adjustment process is called geostrophic adjustment: excess energy stored in the unbalanced pressure gradient radiates away as gravity waves or cascades to smaller scales ultimately dissipated by viscosity. When the dust settles, the dominant horizontal winds are left approximately geostrophic over length scales of $\sim R_d$ (Vallis 1992).

Thus, due to the rotation of the Earth, atmospheric motion self-organises on horizontal scales $\sim R_d$. In the midlatitudes, this motion manifests as Rossby waves and vortices in approximately geostrophic balance that make up our day-to-day weather. Rossby waves are particular to rotating fluids; they oscillate on spatial gradients of *potential vorticity*.

Potential vorticity

Potential vorticity comprises the planetary vorticity, the relative vorticity, and a representation of the moment of inertia of the rotating body, here taken to be a fluid element. The planetary vorticity is the vorticity due to the rotation of Earth, whose magnitude is approximately $f = 2\Omega\sin(\phi)$. The relative vorticity is the vorticity of the wind field itself, with the largest contribution coming from the horizontal winds, $\zeta = \partial v/\partial x - \partial u/\partial y$. In the shallow-water approximation, the moment of inertia of the rotating body is represented by the depth of the fluid, h. Fluid particles that move across spatial gradients in either term may compensate for the environmental changes in potential vorticity by changing the relative vorticity and the structure of the rotating body such that

$$\left(\frac{\partial}{\partial t} + \boldsymbol{u}\cdot\boldsymbol{\nabla}\right)\left(\frac{\zeta + f}{h}\right) = 0 \tag{2.11}$$

(Vallis 2017). Under certain flow configurations, the compensation between the terms will set up a *Rossby wave.* Neglecting variations in h and assuming a uniform westerly background zonal flow, $\overline{u}$, the dispersion relation for linear *barotropic* Rossby waves yields

$$\omega = \overline{u}k - \frac{\beta k}{k^2 + l^2}, \tag{2.12}$$

where k and l are the zonal and meridional wave numbers and we have made the beta-plane approximation, namely that $f = f_0 + \beta y$, where f_0 and $\beta = df/dy$ are constants evaluated at a fixed latitude (Vallis 2017). The phase and group velocities that follow from the dispersion relation (Eq. 2.12) reveal that changes in potential vorticity due to meridional excursions (zonal wave number $k \neq 0$) sets up a westward propagating Rossby wave relative to the westerly background flow. The zonal background flow imposes a Doppler shift on the wave.

In shallow water, if a fluid particle travels a distance l and $l \ll R_d$, then the fluid particle will not experience any significant changes in surface elevation; the geostrophically adjusted surface elevation varies over spatial scales $\sim R_d$. If $l \gg R_d$, the potential vorticity variations are dominated by changes in the planetary vorticity. This scaling is appropriate for so-called *planetary geostrophic motion*: rarely relevant in the atmosphere but important for oceanic dynamics (Vallis 2017).

For horizontal motion of scales similar to the deformation radius, $l \sim R_d$, relative vorticity and vortex stretching (changes in surface elevation in shallow water) contribute similarly to changes in potential vorticity, while the planetary vorticity becomes increasingly important as the particle makes larger meridional excursions. Horizontal motion of scales similar to the deformation radius characterises the weather systems in the midlatitudes and implies that the weather systems feature horizontal motion that is large enough to 'communicate' through the vertical extent of the troposphere.

2.2.2 Stratification

The most important dynamical concepts of the mid-latitude weather systems are described by so-called *quasi-geostrophic* scaling of the governing equations. Quasi-geostrophic scaling assumes a small Rossby number and the characteristic length scale of motion to be similar to R_d, considering the terms of zeroth- and first-order Rossby number. In the quasi-geostrophic *continuously stratified* equations, the Rossby radius of deformation is given by

$$R_d = \frac{NH}{f}, \tag{2.13}$$

where H is the scale height and N is the Brunt–Väisälä frequency, which measures the vertical stratification of the atmosphere (Vallis 2017). Like gH in Eq. 2.8, NH is proportional to the velocity of the fastest gravity and Kelvin waves in a stratified atmosphere. Without going into the details, Kelvin wave crest amplitude has an e-folding length scale of R_d, normal to the propagation direction (Pedlosky 1987).

The deformation radius has several case dependent interpretations. One possible interpretation is that, in the geostrophic adjustment problem, it reflects the competition between the horizontal redistribution of mass by gravity waves and the Coriolis force.

The continuously stratified deformation radius relates the scales of the horizontal and vertical motions. In the quasi-geostrophic equations, vertical motion is a response to temperature advection by the geostrophic winds (Hoskins et al. 1978). The stratification acts against vertical motion; in a highly stratified atmosphere (N is large), fluid particles need to travel further parallel to the temperature gradients in order to advect the temperature needed to trigger vertical motion, compared to a weakly stratified atmosphere (N is small). Analogous to shallow water, for horizontal motion $\sim R_d$, relative vorticity and stratification similarly influence potential vorticity.

Vertical motion is key for the existence and growth of mid-latitude weather systems. The vertical motion converts potential energy stored in the atmosphere — ultimately constructed by the radiative imbalance between the tropics and the poles — into kinetic energy organised in vortices that are the low- and high-pressure systems that make up our weather (Lorenz 1955). This conversion process is called *baroclinic instability* (Eady 1949) and is discussed in Section 2.4.

2.3 Latent heat

About 71 % of the surface of Earth is covered by oceans. From a global perspective, there is therefore no shortage of liquid water sources from which water evaporates and subsequently circulates through the atmosphere as vapour. Evaporation, the phase change from liquid to gas, requires an input of energy to overcome the molecular forces that structure molecules in their respective states. When water vapour condenses, transitioning from gas to liquid, a similar amount of energy is released (Vallis 2017). Condensation in the atmosphere manifests as clouds and precipitation, and the resulting heat release significantly influences mid-latitude atmospheric dynamics (e.g. Hoskins and Valdes 1990; Wernli and Gray 2024), which is also the topic of this thesis.

The *specific humidity* of an air parcel is defined as the ratio of the mass of water vapour to the total mass of air and vapour within the parcel, $q = m^v/(m^d + m^v)$, where m^v is the mass of vapour and m^d is the mass of dry air. Treating both gases as ideal gases, the total pressure within the air parcel is the sum of the partial pressures, defined as the pressure the corresponding gas would exert if it occupied the volume alone. The vapour pressure can be written as

$$e = \frac{qp}{q + \epsilon(1 - q)}, \tag{2.14}$$

where p is the total pressure and ϵ is the ratio of gas constant of dry air to the gas constant of water vapour, $\epsilon = R^d/R^v$ (Vallis 2017).

Considering a system of water vapour over a a plane liquid water surface at constant temperature in equilibrium: the air above the surface is *saturated* and condensation and evaporation occur at the same rate. Varying the temperature, the saturation vapour pressure, e_s, changes according to the *Clausius-Clapeyron relation*,

$$\frac{de_s}{dT} = \frac{L_v e_s}{R^v T^2}, \tag{2.15}$$

where T is temperature and L_v is the latent heat of vapourisation, that is, the energy per mass released at condensation or required for evaporation. Since L_v and R^v are positive, the saturation vapour pressure increases with increasing temperatures. The amount of water that is stable in the form of vapour in an air parcel therefore decreases with decreasing temperatures (Vallis 2017).

Adiabatically ascending air parcels experience decreasing temperatures according to pressure decreases (assuming a hydrostatic atmosphere; Eq. 2.2). If the air parcel

Table 2.1: Latent heat at $T = 0°$ C

Name	Process	Symbol	Value
Vapourisation	Liquid $\leftrightarrow$ vapour	L_v	$2.501 \times 10^6\ J\ kg^{-1}$
Fusion	Ice $\leftrightarrow$ liquid	L_f	$0.334 \times 10^6\ J\ kg^{-1}$
Sublimation	Ice $\leftrightarrow$ vapour	L_s	$2.834 \times 10^6\ J\ kg^{-1}$

contains sufficient water vapour, it becomes saturated at the level where the saturation pressure equals the vapour pressure of the air parcel. Condensation and latent heat release then occur in the presence of a plane liquid surface (Vallis 2017).

In the absence of a plane liquid surface, the air may become supersaturated, that is, $e > e_s$. If droplets or aerosols are present, they provide surfaces onto which the vapour can condense. The varying surface tension of curved droplets and the structure of aerosols complicate the process, such that most condensation occurs under supersaturated conditions (and some condensation occurs in subsaturated air). There is usually no shortage of aerosols in the atmosphere to facilitate condensation (Wang 2013).

In addition to condensation and evaporation, water also changes phase between ice, vapour, and liquid. The respective processes and their latent heat at $T = 0°$ C are given in Table 2.1 (WMO 1966). Although the latent heats vary with temperature, they are often treated as constants in weather and climate models and latent heat release is typically modelled as the amount of water that changes phase times the latent heat of the respective process (Holton and Hakim 2013). In this thesis, I primarily focus in the latent heating due to condensation, which is an order of magnitude larger than that of fusion. Still, all phase changes are accounted for in the model experiments decoupling latent heat release in Chapters 4 and 5.

2.4 Baroclinic instability

2.4.1 Baroclinicity

A fluid is *baroclinic* when its density is not solely a function of pressure, so that the pressure and density gradients are misaligned. This configuration implies a displacement between the geometric centre of a fluid element and the centre of mass of the fluid element, such that the pressure gradient force acts as a torque intending to rotate the fluid element around its centre of mass (Kundu 2008).

In a dry atmosphere, density depends on both pressure and temperature and can therefore be baroclinic. For large-scale atmospheric motion, baroclinicity implies that the vertical distance between isobars varies horizontally, and the resulting pressure gradient forces prompt a rotation in the fluid, which is balanced by the Coriolis force. Yet, the mass displacement on pressure surfaces, that is, the baroclinicity, relative to the mass rearrangement implied by the resulting pressure gradient forces, represents a reservoir of potential energy crucial for the existence of weather systems.

Baroclinicity affecting the large-scale atmospheric flow has important implications for steady-state geostrophic winds, as expressed by the thermal wind balance:

$$f\boldsymbol{k} \times \frac{\partial \boldsymbol{u_g}}{\partial p} = \boldsymbol{\nabla}_p \alpha = \frac{R}{p} \boldsymbol{\nabla}_p T, \tag{2.16}$$

where R is the ideal gas constant, $\alpha = 1/\rho$, and $\boldsymbol{\nabla}_p$ is the horizontal gradient taken at constant pressure; pressure is used as the vertical coordinate. The thermal wind balance states that if density, or equivalently temperature, varies along surfaces of constant pressure, then the geostrophic wind must vary with height. Consequently, the decrease in temperature from the tropics toward the poles is associated with westerly geostrophic winds that strengthen with height. In the real atmosphere, the strongest large-scale horizontal temperature gradients in the sub- and extratropics are accompanied by upper-tropospheric jet streams that obey the thermal wind balance.

2.4.2 Dry baroclinic instability

Baroclinic instability, first described by Charney (1947) and Eady (1949), is essentially the act of *eddies* to equilibrate unstable mean horizontal and vertical temperature gradients and consequently the vertical wind shear (Schneider and Walker 2006). Eddies are anomalies from temporal or spatial means and typically take the form of waves and the high-frequency part of the turbulence spectrum (to the extent the data resolution allows it). Eddies that form in a baroclinic wave reinforce themselves and grow unstable as they exchange warm air with cold air in the process of equilibrating the temperature gradients.

Unstable baroclinic waves have a vertical structure that 'leans into' the vertical wind shear (Fig. 2.1 a; Eady 1949; Marshall et al. 2012). The Charney-Stern-Pedlosky necessary condition for baroclinic instability gives four different configurations that may facilitate a baroclinically unstable wave (Charney and Stern 1962; Pedlosky 1964). Most relevant for Earth is westerlies that increase with height and temperatures that decrease poleward, for which an unstable baroclinic wave is characterised by an upper-level trough of anomalously low potential vorticity lying to the west of a near-surface warm-air anomaly. The cyclonic circulation around the surface warm anomaly advects low potential vorticity air southward into the upper level, while the circulation around the upper-level trough advects warm air northward into the surface anomaly. In this way, the upper- and lower-level anomalies reinforce one another, grow in amplitude, and spin up.

Crucial to this self-reinforcing mechanism are the ascent of warm air and the descent of cold air induced by advection. From an energy perspective, horizontal temperature advection converts available potential energy from the atmospheric mean state into eddy available potential energy (Lorenz 1955). In the eddy state, warm air is lighter and cold air denser than their surroundings. These density anomalies then rearrange vertically, converting eddy available potential energy into eddy kinetic energy. As defined by Lorenz (1955), mean available potential energy is the energy difference between the atmospheric mean state and a reference state in which parcels have been adiabatically rearranged into the minimum energy configuration of the system.

The horizontal scale of the disturbance must be comparable to, or larger than, the Rossby radius of deformation to induce sufficient vertical motion and trigger baroclinic instability. Indeed, the Eady (1949) model predicts that the most unstable mode has a wavelength of $\sim 1.6\ R_d$. Consequently, eddy energy is injected into the midlatitudes at length scales of order R_d, which is the characteristic length scale of the mid-latitude circulation (Schneider and Walker 2006).

The model of Eady (1949) predicts that baroclinic waves grow at a rate proportional to the vertical geostrophic wind shear divided by the vertical stratification, known as the *Eady growth rate*. In this thesis, we measure baroclinicity as the slope of an isentropic surface: the horizontal gradient of potential temperature divided by the vertical gradient of potential temperature, the latter representing static stability. The Eady growth rate is proportional to the horizontal temperature gradient via the thermal wind relation, and inversely proportional to static stability. Thus, the isentropic slope can be used as a proxy for the potential for baroclinic growth (Papritz and Spengler 2015).

2.4.3 Moist baroclinic instability

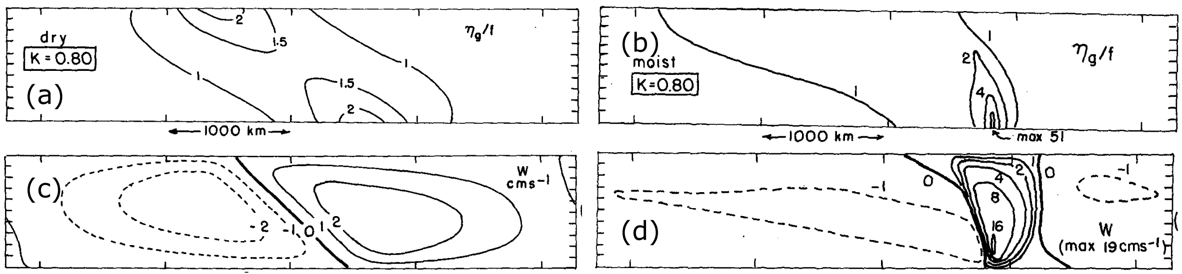

Figure 2.1: Eady-like moist and dry baroclinic instability. From Wernli and Gray (2024), who composed the figure using Figs. 6 and 7 in Emanuel et al. (1987). Shown are the relative vorticity of the dry wave (a) and the moist wave (b), as well as vertical velocities of the dry wave (c) and moist wave (d).

The previous description of baroclinic instability assumes a dry atmosphere. In that case, a baroclinically growing wave exhibits roughly symmetric areas of ascent and descent. In a moist atmosphere, there is sufficient water vapour to reach saturation in the regions of ascent. For baroclinic waves growing in such moist environments, the region of ascent narrows and intensifies, while the downdraft widens and weakens; this enhances the growth rate and reduces the length scales of the unstable waves (Fig. 2.1; Emanuel et al. 1987).

Latent heating is responsible for the asymmetric vertical velocities. Condensation occurs in moist, ascending air and releases latent heat, which further enhances the ascent. The ascending air effectively experiences weaker stratification: an effect that is absent in subsaturated descending air, resulting in a skewed distribution of vertical velocities (O'Gorman 2011). Vorticity advection further enhances this skewness, enabling more localised and intense ascent than in dry dynamics alone (Kohl and O'Gorman 2024).

Latent heating also imposes an asymmetry on the upper-level waves in the troposphere. Diabatically enhanced ascent increases the transport of relatively low–potential-vorticity air into the upper troposphere, which is deposited in and amplifies the ridges of the upper-level waves (Methven 2015). The resulting divergent outflow also causes the ridges to grow at the expense of the troughs (Teubler and Riemer 2021).

Moisture in the atmosphere introduces a distinct category of baroclinic waves (Parker and Thorpe 1995). Diabatic heating generates positive potential vorticity below the heating maximum; in this way, latent heating can produce positive vorticity in the lower troposphere. In a sufficiently moist and baroclinic region, the diabatically generated vortex induces slantwise ascent that triggers further latent heating and again generates positive potential vorticity downstream of the original vortex, causing the vortex to propagate toward the heating it generates (Boettcher and Wernli 2013). Such diabatic Rossby waves may interact with upper-level troughs and quickly grow unstable.

In summary, moisture tends to enhance baroclinic growth, reduce the energy-containing length scales, and increase mid-latitude waviness. In the next section, I discuss the practical implications of baroclinic instability, namely the formation of mid-latitude storm tracks and their role in the global atmospheric circulation. Relevant effects of moisture on storm tracks are discussed in Section 2.6.

2.5 A mid-latitude perspective on the atmospheric circulation

Baroclinically unstable waves grow most effectively when they span the full vertical extent of the troposphere. An integral component of such a wave is the upper-level jet stream, which facilitates the troughs and ridges that connect to the storms below. Storm tracks and jets are therefore closely interlinked.

Jets are typically classified as either subtropical or eddy-driven. I will first describe the subtropical jet before discussing storm tracks, the eddy-driven jet, and the role of storm tracks in the global circulation.

2.5.1 The Hadley cell and the subtropical jet streams

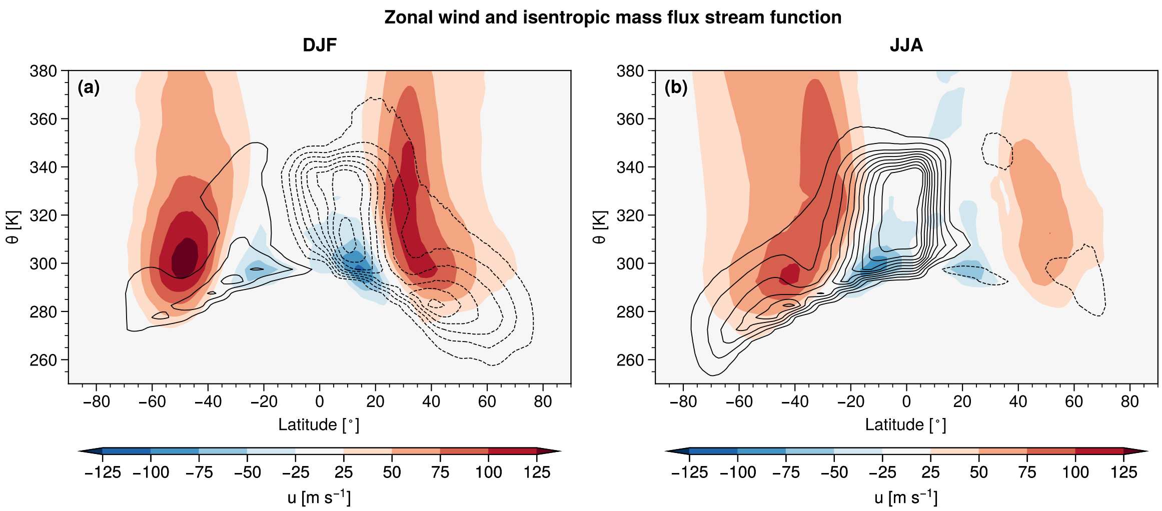

Figure 2.2: The meridional circulation on dry isentropes. The shading shows the density weighted zonal wind on isentropic surfaces and the contours show the meridional isentropic mass flux stream function averaged over December, January, February (a) and over June, July, and August (b). The calculations are as in Pauluis et al. (2010), computed on 50 years of simulation with an atmospheric general circulation model with prescribed present-day climate sea surface temperatures. The model is described in Chapter 4. The circulation inferred from the stream function is clockwise in the Northern Hemisphere and anti-clockwise in the Southern Hemisphere.

The tropics experience a net radiative heating absorbing short wave radiation while emitting less long wave radiation. The shortwave-to-longwave distribution is opposite in the polar areas; the polar regions experience a net radiative cooling. The tropical air is consequently more energetic (it is warmer and moister, and therefore also at higher altitudes) than the polar air. To equilibrate the meridional energy gradient, air that ascended to the upper troposphere at the latitude of maximum insolation travels poleward.

Conserving angular momentum, the poleward flow in the tropical upper troposphere gains westerly momentum relative to the Earths surface as it moves closer to Earths rotational axis (Held and Hou 1980). At approximately 30° north and south, the circulation features strong westerlies which form a strong, and baroclinically unstable, *subtropical jet* in the upper troposphere. The mean meridional flow converges, the air cools radiatively and subsides there; some of it then travels equatorward over the surface forming the trade winds. This meridional circulation is know as the Hadley cell.

Figure 2.2 shows the mean isentropic mass flux streamfunction for December, January, and February and June, July, and, August in an atmospheric general circulation model. The thermally direct Hadley cell is clearly visible in the respective winter hemispheres. The subtropical jet is also clearly visible in the zonal wind at the subtropical edges of the Hadley cell.

The subtropical jet is characterised by vertical wind shear and thus by a horizontal temperature gradient. Continued poleward advection of heat and angular momentum accelerates the jet and can make it baroclinically unstable, whereas Rossby waves breaking within the subtropical jet act to decelerate it and transport westerly momentum into the extratropics (Lee and Kim 2003; Schneider 2006). In fact, most baroclinic wave generation occurs poleward of the edge of the Hadley cell, as discussed next.

2.5.2 The existence of storm tracks

In the midlatitudes, sharp gradients in surface temperature primarily cause the strongest baroclinicity. These gradients typically arise from pronounced land–sea temperature contrasts or from sharp gradients in sea surface temperature itself, which imprint on the overlying atmosphere via sensible heat fluxes. The western boundary currents transport warm water north and east of North America and east of Japan, making these regions hot spots of baroclinicity and baroclinic instability (Hoskins and Valdes 1990; Swanson and Pierrehumbert 1997; Hotta and Nakamura 2011).

In the wake of the Rocky Mountains and the Tibetan Plateau, Rossby-wave troughs form in the upper-tropospheric westerly jets (Held et al. 2002). These troughs induce slantwise ascent and lower-level disturbances that enter the baroclinic regions over the western boundary current extensions, where they develop into baroclinic waves spanning the full depth of the troposphere (Hoskins et al. 1978; Chang et al. 2002; Hoskins and Hodges 2002). The lower-level disturbances manifest as cyclonically rotating systems known as *extratropical cyclones*.

Similarly, in the Southern Hemisphere, the wake of the Andes and Australia are hot spots for cyclogenesis in winter (Hoskins and Hodges 2005). Sea surface temperature gradients in the Southern Ocean are more annular than in the Northern Hemisphere because of the absence of continents; in austral summer, the storm track also appears annular.

The upper-level trough and the lower level cyclones travel eastward with the westerly winds across the ocean basins (Chang et al. 2002). The cyclones transport warm and moist air poleward and cold and dry air equatorward during the baroclinic growth stage. Towards the end of the cyclone life cycle, the trough aligns vertically with the lower level cyclone; the baroclinic wave no longer leans into the vertical wind shear. At this stage the cyclone is considered barotropic and dissipates (Orlanski and Katzfey 1991). The cyclone life cycle is discussed in more detail in Section 2.5.3.

If the cyclone makes landfall, surface friction accelerates its dissipation. In the North Atlantic, cyclones that spawn over the Gulf Stream extension tend to reach the European continent before they dissipate. The North Pacific is roughly twice as wide, and cyclones generated over the Kuroshio current commonly dissipate before they make landfall. The upper-tropospheric wave that comprises the trough linked to the lower-level cyclone is dispersive and regenerates downstream of the cyclone. This effect is known as downstream development (Orlanski and Katzfey 1991; Chang and Orlanski 1993): the regenerated trough forces a new cyclone downstream of the original one, and the storm track 'restarts' and continues westward.

Although primary cyclogenesis most commonly occurs over the Gulf Stream and Kuroshio current extensions and in the wakes of the Andes and Australia, it is not confined to these regions but also takes place in other areas characterised by lower-tropospheric baroclinicity or upper-level forcing (Hoskins and Hodges 2002; Hoskins and Hodges 2005). New cyclones may also develop along the fronts of existing systems, a process referred to as secondary cyclogenesis (Ford and Moore 1990).

2.5.3 The cyclone life cycle and the eddy-driven jet streams

In general, the cyclone life cycle is characterised by baroclinic growth and barotropic decay (Simmons and Hoskins 1978). During the baroclinic growth stage, poleward eddy heat fluxes act not only to reduce the meridional temperature gradient but also to transport westerly momentum from the upper to the lower troposphere (Andrews and McIntyre 1976; Edmon et al. 1980). This process can be viewed as temperature advection exerting a form drag on the sloping isentropic surfaces, thereby accelerating westerly geostrophic winds in the isentropic layer below (Vallis 2017).

The downward eddy momentum flux reduces the vertical wind shear in the baroclinic jets, which results in a more barotropic wind profile known as the *eddy-driven jet* (Lee and Kim 2003; Woollings et al. 2010). The eddy momentum fluxes are directed opposite to the Rossby wave propagation (Edmon et al. 1980). Climatologically, Rossby waves propagate from the surface and upwards, thus, transporting westerly momentum downwards and driving the lower-tropospheric westerlies.

During the growth stage, the cyclones convert baroclinic potential energy into barotropic eddy kinetic energy (Rhines 1975; Simmons and Hoskins 1978). During the barotropic decay stage, two-dimensional turbulence theory on a rotating sphere predicts an upscale cascade of barotropic kinetic energy, from the eddies to the zonal mean flow.

The eddies, comprising both cyclones and anticyclones, not only maintain the zonal-mean eddy-driven jet but also redistribute momentum zonally, thereby sustaining jets that can be zonally asymmetric in strength and position (Hoskins et al. 1983; Cai and Mak 1990). Also in the horizontal direction, the westerly eddy momentum flux is directed opposite to the Rossby wave propagation: the westerlies are accelerated at the wave source, from which the waves tend to diverge, and decelerated where wave activity converges and and the waves break. There is a climatological tendency for Rossby waves to propagate equatorward and break in the subtropics, which transports westerly momentum from the edge of the Hadley cell into the extratropics, as discussed earlier.

The irreversible momentum mixing associated with Rossby wave breaking is a key mechanism by which eddies influence the circulation. Anticyclonic wave breaking shifts the jet poleward, whereas cyclonic wave breaking shifts it equatorward; the type of breaking is closely linked to baroclinic wave development (Thorncroft et al. 1993; Balasubramanian and Garner 1997). Baroclinic wave development and wave breaking are, in turn, preconditioned by the jet's location, structure, and baroclinicity (Orlanski 2003; Rivière 2009; Barnes et al. 2010; Novak et al. 2015). This nonlinear interaction between the mean flow and the eddies influences the mean state and drives variability of the eddy-driven jet stream (Robinson 2006; Woollings et al. 2008; Woollings et al. 2010).

Subtropical and eddy-driven jet streams coexist on Earth. They tend to be merged where the Hadley cell drives a strong subtropical jet that generates baroclinic waves.

When the subtropical jet is weak, baroclinic wave generation occurs at higher latitudes, and the eddy-driven and subtropical jets appear as two separate wind maxima. The split and merged configurations on Earth vary with longitude and season, but appear merged in the zonal mean (Lee and Kim 2003; Woollings et al. 2023).

The eddy driven jet stream is featured in Fig. 2.2 as the zonal wind extending into the thermally direct mid-latitude cell. This cell represents the temperature transport done by mid-latitude storm track, discussed in the next section.

2.5.4 The role of storm tracks in the global circulation

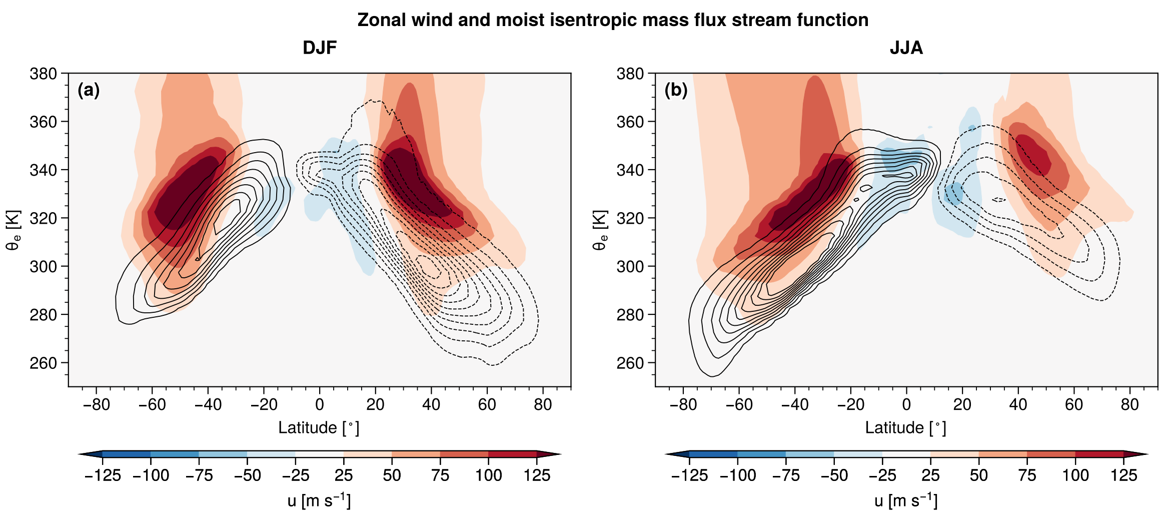

Figure 2.3: The meridional circulation on moist isentropes. Like Fig. 2.2, but for moist isentropes. The circulation inferred from the stream function is clockwise in the Northern Hemisphere and anti-clockwise in the Southern Hemisphere.

Extratropical storms are responsible for most of the poleward energy transport and redistribution of momentum in the midlatitudes (Trenberth and Stepaniak 2003; Schneider 2006; Yamada and Pauluis 2015). In Fig. 2.2, the wintertime storm tracks appear as thermally direct cells centred at approximately $\pm 40°$. The isentropic mass flux transports entropy poleward and upward from the subtropics and towards the poles. The ascent in isentropic coordinates around $\pm 40°$ implies diabatic heating caused by condensation within the storm tracks. The poleward flow is otherwise cooled by radiative heat loss, while the cold return flow (in the lower branch) is diabatically heated at the surface; thus, both flows cross isentropic surfaces (Pauluis et al. 2010).

(In pressure or height coordinates, the time-zonal-mean mid-latitude circulation is thermally indirect. The time-zonal-mean circulation balances the eddy heat fluxes by adiabatically cooling the warm air advected poleward through ascent and adiabatically heating the cold return flow through descent. This residual circulation is called the *Ferrel cell*.)

Aggregating the zonal wind and meridional mass flux on moist isentropic surfaces (accounting for latent heat of the water vapour in the air parcel; θ_e) instead reveals a single thermally direct cell in both summer and winter hemispheres (Fig. 2.3). Comparing Figs. 2.2 and 2.3 yields two main insights. First, in the warm season, moisture transport dominates the meridional energy circulation. Second, the poleward transport of warm, moist air on dry isentropes around $\pm 30°$ is compensated by an equatorward transport of warm, dry air on the same dry isentropes. These mass fluxes occur on separate moist isentropic surfaces, such that the moist-isentropic mass flux exhibits only one thermally direct cell per hemisphere, whereas the dry-isentropic mass flux exhibits two (most clearly visible in the winter hemispheres; Laliberté et al. 2012).

The seasonal cycle is the largest climate signal on record. As indicated by (1), atmospheric water vapour increases as the climate warms. As a result, the hydrological cycle intensifies, more energy is transported in the form of water vapour, and the effects of latent heating are expected to become increasingly important for the mean state and variability of the mid-latitude storm tracks and jet streams.

2.6 Moist jets and storm tracks

How, and to what extent, moisture shapes the mid-latitude mean state and variability is an area of active research. In this thesis, I focus on the effects of latent heating from the condensation of water on the mid-latitude circulation.

2.6.1 Potential effects of latent heating on storminess

There are multiple ways in which latent heating could affect storminess, but the description of these mechanisms depends on how storminess is defined.

From an eddy–mean flow perspective, storminess typically refers to synoptic scale eddy kinetic energy. Latent heating may affect eddy kinetic energy through its influence on the available potential energy associated with the eddies themselves (a direct effect) and on the available potential energy of the mean state (an indirect effect; Lorenz 1955).

Latent heating tends to amplify eddy available potential energy, as condensation occurs in the anomalously warm and moist air advected poleward, further heating that air (Novak and Tailleux 2018). Simultaneously, the metrics of e.g. Novak and Tailleux (2018) and Lutsko et al. (2024) indicate that latent heating decreases mean available potential energy; I examine why in Chapter 3. Mean available potential energy again scales with eddy kinetic energy and hemispheric aggregates of both are projected to decrease with global warming (O'Gorman 2010). The extent to which latent heating increases or decreases storminess, represented by eddy kinetic energy, thus depends on two potentially competing effects: the direct eddy invigoration versus the effect on the mean state potential energy (Lutsko et al. 2024).

By considering tracked extratropical cyclones as storms, the question of whether latent heating increases or decreases storminess implies slightly different mechanisms.

The eddies comprise both cyclones and anticyclones, and indeed, analogous to latent heating amplifying eddy available potential energy: latent heating tends to enhance cyclone growth rates and strengthen individual cyclones (e.g. Wernli and Gray 2024). At upper levels, latent heating strengthens the anti-cyclones (Methven 2015).

The effect of latent heating on the potential for cyclones to grow through baroclinic instability is more difficult to reconcile with the eddy–mean flow perspective. The central question is whether cyclone-driven latent heating produces or consumes baroclinicity for subsequent cyclones to develop.

In other words, and as originally posed by Hoskins and Valdes (1990), does latent heating act against or towards the self-maintenance of storm tracks via its effect on baroclinicity? This question is not directly comparable to the eddy-mean flow perspective: for example, diabatically enhanced secondary cyclogenesis occurs on synoptic timescales (Weijenborg and Spengler 2020) and would therefore be represented as a diabatic increase in eddy available potential energy, rather than as an increase in mean available potential energy.

2.6.2 Latent heating and climate change

The Northern Hemisphere winter storm tracks are projected to intensify regionally, while the summer storm tracks generally weaken (Harvey et al. 2020a). As water vapour accounts for an increasing fraction of the atmospheric composition with warming, it seems likely that latent heating plays an important role in the projected storm track changes (Catto et al. 2019). That cloud microphysics and parts of the ascent that produce latent heating in storms are approximated by parametrisations in conventional climate models thus contributes to the uncertainty in climate projections. To confidently evaluate projections of future mid-latitude climate, we therefore require a robust physical understanding of the effects of increased latent heating on the mid-latitude storm tracks.

From an atmospheric energy budget perspective, warming allows each storm to transport more energy in the form of water vapour, and fewer, weaker, and/or smaller storms are therefore needed to balance the meridional energy gradients (Held 1993; Hall et al. 1994). Indeed, recent climate models project fewer storms overall, yet an increase in the number of extreme storms with warming (Priestley and Catto 2022).

Warming may also affect the location of storm tracks and the closely interlinked jets (Ossó et al. 2024). There are, however, large uncertainties associated with the jet and storm track shifts projected by current climate models, and the wide range of driving mechanisms behind such shifts further reduces our confidence in these projections (Breul et al. 2025).

Latent heating, for example, affects jets over a range of scales and mechanisms. Without mentioning organised mesoscale convection: latent heating influences synoptic jets (Harvey et al. 2020b; Bukenberger et al. 2023), zonally averaged jets (Xia and Chang 2014; Yamada and Pauluis 2017; Baker et al. 2019; Lachmy and Kaspi 2020; Lachmy 2022; White et al. 2024), temporally averaged jets (Hermoso et al. 2024), and the amplitude and breaking of the waves facilitated by these jets (Madonna et al. 2014a; Madonna et al. 2014b; Methven 2015; Pfahl et al. 2015a; Zhang and Wang 2018; Teubler and Riemer 2021), and there is no single, simple explanation for how the integrated impact changes with warming.

2.6.3 A latent heating-dynamics feedback

In general terms, latent heating affects atmospheric dynamics by altering temperature gradients; the exact location at which the heating occurs is key. Latent heating within storm tracks, in turn, is driven by the dynamics, occurring in warm, moist, ascending air associated with the storms themselves (Pauluis et al. 2010).

In the following chapters, we demonstrate that latent heating is non-linearly coupled to the dynamics, with the implication that small-scale, transient latent heating has large-scale, time mean consequences. We design a modelling experiment that tests the effect of the nonlinear coupling between the heating and the dynamics, treating the coupling between latent heating and the dynamics as a feedback mechanism on the storm track as a whole. Finally, we examine the importance of the latent heating feedback for storm track changes under global warming.

Chapter 3

The dependence of latent heating on synoptic dynamics

This chapter is based on Auestad et al. (2024) and discusses the effect of latent heating on baroclinicity within jet streams. There is no consensus on the effect of latent heating on the cross-jet temperature contrast, which is our proxy for baroclinicity. Here, we show that the lack of consensus is attributable to the choice of spatio–temporal averaging of the jet streams in question. Jet representations relying on averaged wind tend to have the strongest latent heating on the cold flank of the jet, thus weakening the cross-jet temperature contrast. In contrast, jet representations reflecting the two-dimensional instantaneous wind field have the strongest latent heating on the warm flank of the jet. Furthermore, we show that latent heating primarily occurs on the warm flank of poleward directed instantaneous jets, which is the case for all storm tracks and seasons.

3.1 Introduction

Jet streams are an integral part of the planetary scale flow. They guide synoptic weather systems and are key for the existence of storm tracks (Chang et al. 2002; Martius et al. 2010; Wirth et al. 2018). In return, the synoptic weather systems shape the planetary scale flow by redistributing heat, momentum, and vorticity (Edmon et al. 1980; Hoskins et al. 1983) and by modulating baroclinicity within the storm tracks through diabatic heating (Hoskins and Valdes 1990; Papritz and Spengler 2015). While diabatic heating related to moist processes climatologically maintains baroclinicity (Papritz and Spengler 2015; Marcheggiani and Spengler 2023), there is conflicting evidence to which extent it dampens or amplifies low frequency variability (Xia and Chang 2014; Woollings et al. 2016; Lutsko and Hell 2021). We disentangle these conflicting findings by contrasting jet-relative diabatic heating for different jet representations.

Latent heating influences baroclinic wave activity on timescales beyond the lifetime of a single cyclone through its effect on baroclinicity (Hoskins and Valdes 1990; Papritz and Spengler 2015; Weijenborg and Spengler 2020). As hypothesised by Robinson (2000), anomalous cyclone activity and eddy momentum fluxes following from anomalous baroclinicity may modify the persistence of the planetary scale flow (e.g. Lorenz and Hartmann 2001; Blanco-Fuentes and Zurita-Gotor 2011; Zurita-Gotor et al. 2014; Lorenz 2022). Thus, if latent heating dampens the anomalous baroclinicity, it should also dampen the planetary scale flow variability, and vice-versa. While this mechanism concerns the amplitude of momentum fluxes, the resulting baroclinicity may also affect the preferred type of wave breaking and therefore the direction of the momentum fluxes (Orlanski 2003; Rivière 2009).

Xia and Chang (2014) conditioned zonal mean latent heating (precipitation) on the first principal component of the 300 hPa daily zonally averaged zonal wind in the

Southern Hemisphere and found it to weaken the cross-jet temperature contrast in both phases of the first principal component. Following a similar argument, Bembenek et al. (2020) and Lutsko and Hell (2021) showed that latent heating mainly occurs on the poleward flank of a zonal mean jet, abating the mean baroclinicity and therefore weakening the mean westerlies. The experiment of Yamada and Pauluis (2017) adds further nuance, showing that latent heating occurs in the core of a zonal mean jet for a cyclonic wave breaking event. On the other hand, Woollings et al. (2016) analysed the instantaneous two-dimensional tendency of the isentropic slope (Papritz and Spengler 2015), showing a positive feedback to baroclinicity in the anomalous position of the storm track. The isentropic slope framework also shows that latent heating maintains the seasonal mean baroclinicity in the North Atlantic storm track (Papritz and Spengler 2015; Marcheggiani and Spengler 2023).

The disagreement between Xia and Chang (2014) and Woollings et al. (2016) could stem from the choice of storm track region and season. Xia and Chang (2014) studied the Southern Hemisphere during summer, while Woollings et al. (2016) studied the North Atlantic during winter. However, the studies also differ in their methods. Xia and Chang (2014) used zonally averaged daily mean wind and precipitation and assumed that latent heating is linearly dependent on the first principal component of the zonal mean wind. Thus, their results could be sensitive to their choice of jet definition and spatio–temporal averaging. Woollings et al. (2016), on the other hand, used the isentropic slope framework which requires neither temporal nor spatial averaging and does thereby not rely on zonal means.

To address these conflicting results, we compile jet conditional climatologies of latent heating and other pertinent variables to explore their sensitivity to spatio–temporal averaging and different jet definitions, either based on zonal means or the two-dimensional wind field. We specifically explore the extent to which latent heating occurs on the warm or cold flank of each jet definition, reflecting on the fact that *jet* is a widely used term in the literature. Climatologists often refer to 'mean flow' features as jets, while synopticians tend to reserve the term for instantaneous jet–like wind profiles.

3.2 Data

We use three-hourly data from ERA5 (Hersbach et al. 2020) for December, January, and February for the period 1979 to 2020. We focus on the North Atlantic but also show some analysis for the North Pacific, South Pacific and Indian Ocean. We use the three-dimensional wind, specific humidity and temperature on a 0.5° horizontal grid and 22 pressure levels [10, 30, 50, 100, 150, 200, 250, 300, 350, 400, 450, 500, 550, 600, 650, 700, 750, 800, 850, 900, 950, 1000] hPa, as well as large-scale and convective precipitation aggregated at the surface. Forecasted diabatic temperature tendencies due to all physical parameterizations as well as only due to radiation are available on model levels and interpolated to the same pressure levels. We use horizontal wind on the 2 potential vorticity units (2 PVU; 2×10^{-6} K kg^{-1} m^{2} s^{-1}) surface for the jet detections.

We subtract the radiative diabatic tendencies from the total diabatic temperature tendency due to physical parametrization and assume that the remaining diabatic heating tendencies are dominated by latent heating above the boundary layer (Papritz and Spengler 2015). Following the example of Papritz and Spengler (2015), we average the "diabatic minus radiative" heating over 700–200 hPa and refer to this as latent heating. Correspondingly, the vertical wind and the specific humidity are also averaged over 700–200 hPa.

Table 3.1: The five different jet definitions.

Label	Full name
3h-Z	three-hourly sector-mean jet
1d-Z	Daily sector-mean jet
10d-Z	10-day low-pass sector-mean jet
3h-2D	three-hourly two-dimensional jet
10d-2D	10-day low-pass two-dimensional jet

3.3 Jet detection

We consider two types of jet representations (Table 3.1): one based on zonally averaging the wind field, referred to as *sector-mean* jets, and the other based on jet axes defined by the two-dimensional wind field, which we refer to as *two-dimensional* jets. Zonally averaged wind is frequently used to identify and diagnose the mid-latitude jet stream (e.g. Robinson 2000; Lorenz and Hartmann 2001; Woollings et al. 2010; Blanco-Fuentes and Zurita-Gotor 2011; Zurita-Gotor et al. 2014; Bembenek et al. 2020; Lutsko and Hell 2021). This has the advantages of efficiency and a clear connection to the zonal momentum budget, but with the disadvantage that zonally averaging neglects the meandering characteristic of the mid-latitude jet (Spensberger et al. 2023). The two-dimensional jet representation, on the other hand, captures such waviness.

The sector-mean jet position is computed by picking the latitude of the strongest zonally averaged zonal wind between 60°W and 0°E on the 2 PVU surface. We perform this analysis for every time step to represent the jet over the central to eastern North Atlantic Ocean, only allowing for one jet latitude for each time step. The method is similar to Woollings et al. (2010), but using upper- instead of lower-tropospheric zonal wind.

The two-dimensional jet representation follows Spensberger et al. (2017). In short, jets are detected where the wind shear perpendicular to the wind direction is zero on the 2 PVU surface.

$$\frac{\partial U}{\partial n} = 0\,, \tag{3.1}$$

where $U = \sqrt{u^2 + v^2}$ and n is perpendicular to the wind direction. Like Spensberger et al. (2017), we apply a T84 truncation to the data before detecting the jets to smooth out smaller scale features and provides for more spatially coherent jets. We use the freely available Python library Dynlib (Spensberger 2024) for the computations.

The two-dimensional jets detected within [20° N–70° N, 80° W–10° E] are used to represent the North Atlantic. An undesirable effect of Eq. 3.1 is that it is also satisfied for wind speed minima. Additionally, high wind speed areas do not always have a well defined jet structure. We mitigate these challenges by only considering locations where $K \leq (\partial U/\partial n)^2 + U\partial^2 U/\partial n^2$ (Spensberger et al. 2017). This approach only identifies wind speed maxima as jets. It also allows for weaker winds with a clear jet like profile to be classified as jets and filters out points of high wind speed without a well defined jet structure. K is set to the 12.5th percentile of $(\partial U/\partial n)^2 + U\partial^2 U/\partial n^2$. For the three-hourly data, $K = -0.732 \cdot 10^{-8}$ s^{-2}, consistent with Spensberger et al. (2023). Note that, generally, several two-dimensional jets are detected at each time step. See Spensberger et al. (2017) for more details on the jet axis detection.

To assess the sensitivity of our findings to temporal averaging, we compute jet latitudes using instantaneous three-hourly, daily mean, and 10-day low-pass filtered data. For the 10-day low-pass filtered data, daily mean values are first computed from the three-hourly data before applying a Lanczos filter (Duchon 1979) with a 61-day window. The two-dimensional jets are computed on the three-hourly and the 10-day low-pass filtered wind field. For the two-dimensional jet detection using the 10-day low pass data, we apply $K = -1.044 \cdot 10^{-10}$ s^{-2}.

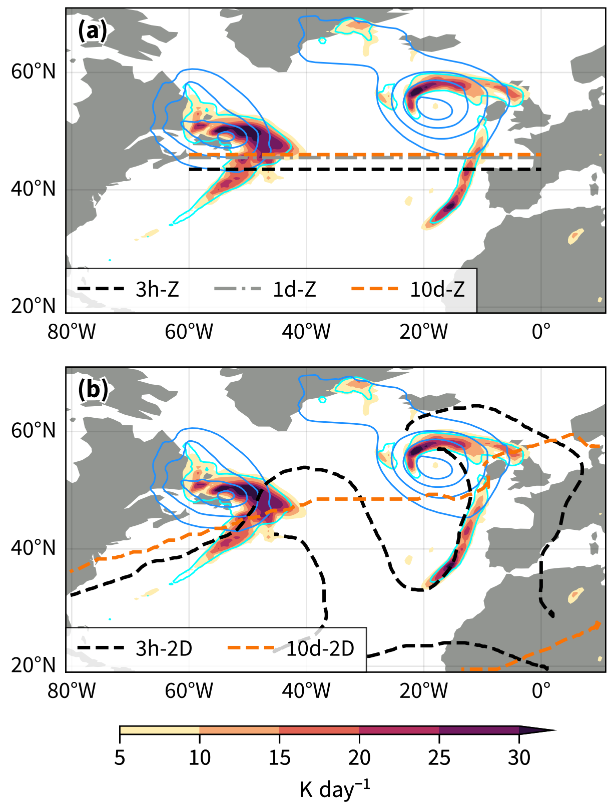

Figure 3.1: Latent heating (shading), large-scale precipitation (cyan; 0.33 mm h^{-1}) and sea level pressure (blue; 960, 970, 980, 990, 1000 hPa) for 14 January 2009 at 21:00 UTC. The dashed lines in (a) show the sector-mean jets computed on three-hourly zonal wind (black; 3h-Z), daily mean zonal wind (grey; 1d-Z), and 10-day low-pass zonal wind (orange; 10d-Z). The dashed lines in (b) show the two-dimensional jets computed on three-hourly winds (black; 3h-2D), and 10-day low-pass winds (orange; 10d-2D).

We refer to the sector mean jets as 3h-Z, 1d-Z, and 10d-Z for the three-hourly, daily, and 10-day low-pass wind, respectively (Table 3.1). The two-dimensional jets are analogously referred to as 3h-2D and 10d-2D. Illustrating the differences between the jet definitions, Fig. 3.1 a shows the sector mean jets simply intersecting the latent heating associated with the two cyclones on 14 January 2009 at 2100 UTC. The 3h-Z jet is located further south compared to both 1d-Z and 10d-Z. In contrast, the 3h-2D jets exhibit synoptic scale variations, outlining troughs and ridges (Fig. 3.1 b). The 10d-2D version does not pick up any synoptic variability but rather follows a straight line from the Gulf Stream region to Northern Europe.

3.4 Construction of jet conditional climatologies

We compile climatologies for vertical wind, specific humidity, latent heating, and precipitation for the different jet definitions. All variables are of three-hourly time resolution, irrespective of the time filtering used for the jet definition.

For climatologies conditional on the sector-mean jet latitude, we first average the variables over the same longitudinal sector (60° W–0° E) as used to define the sector-mean jet latitude (Fig. 3.2 a). The resulting sector mean values are then capped at 20° latitude ($\sim$ 2200 km) on each side of the concurrent three-hourly, daily, and 10-day low-pass sector-mean jet. The data are organised by the latitude of the concurrent sector-mean jet, given on the horizontal axis in the right panel of Fig. 3.2 a, so that the lowest jet latitude states are on the left and the highest jet latitude states on the right. The vertical axis in the right panel of Fig. 3.2 a shows the cross-jet distance spanning $\pm 20°$ latitude. Finally, the data around jets found at similar latitudes are then averaged over by binning the data using 30 bins in the horizontal and 20 bins in the vertical direction, before averaging over each bin.

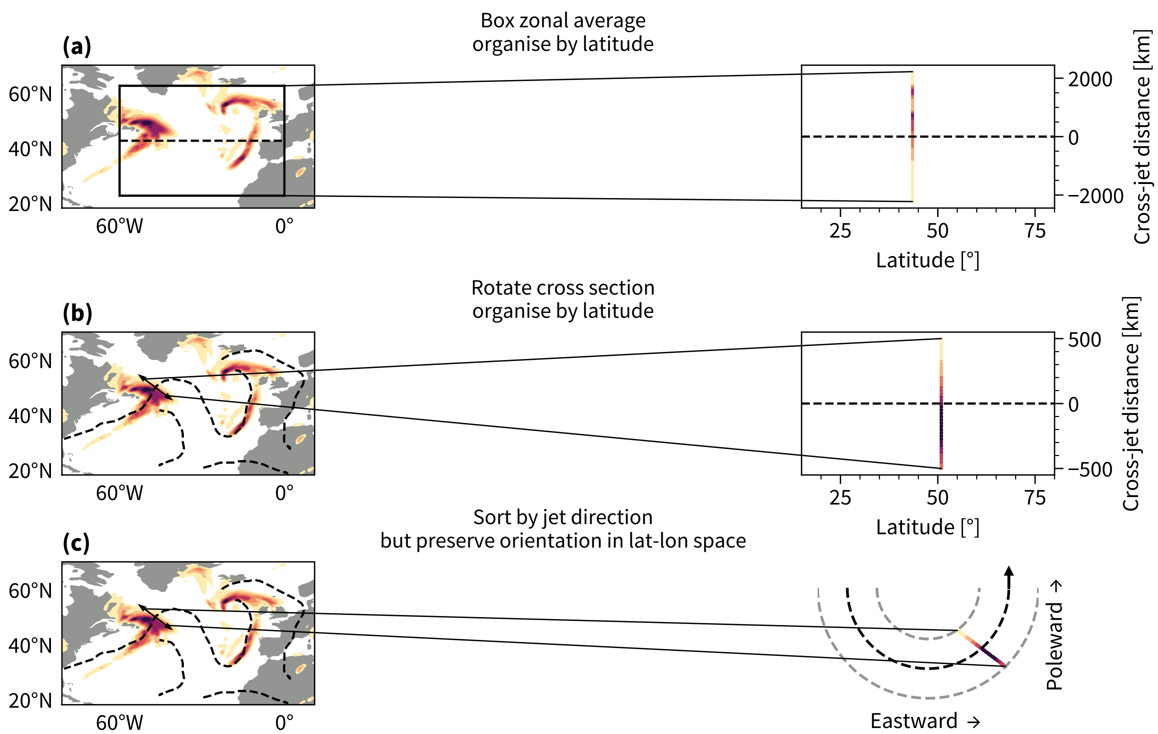

Figure 3.2: Illustration of how we compile the climatologies conditional on jet latitude based on (a) sector-mean jet latitudes, (b) the latitude of the two-dimensional jets, and (c) the jet direction. The dashed lines illustrate the jets. The box illustrates the area for the sector zonal averaging and the arrows illustrate the jet cross section.

The computation of climatologies conditional on the latitude of the two-dimensional jets is illustrated in Fig. 3.2 b. A random set of 100,000 cross sections are sampled from all two-dimensional jets (also used by Spensberger et al. 2023), as exemplified by the black arrows. The variables are interpolated to the cross sections, spanning 500 km on each flank of the jets normal to the jet direction. The cross sections are then organised by the latitude of the jet core in each respective cross section. Given that the two-dimensional jets can take any direction in the longitude-latitude space, we rotate the two-dimensional jets so that they appear as pure westerlies. With this rotation, the left flanks of the jets are on the positive- and the right flanks on the negative side of the vertical axis. By the thermal wind relation, the left flank corresponds to the cold flank of the jet, while the right flank correspond to the warm flank of the jet. The data are coarse grained by binning the data using 20 bins in the horizontal and 10 bins in the vertical direction before averaging over each bin.

Lastly, we compute climatologies conditional on the direction of the two-dimensional jets (see Fig. 3.2 c). As for the other conditional climatologies, we make use of jet cross sections but this time organise them by the direction of the jet rather than their latitude. Their original orientation in the longitude-latitude space is preserved and the cross sections are thus organised in semicircles according to their orientation. The climatologies conditional on jet direction have been coarse grained by binning and averaging the data, here using 30 bins in both the horizontal and vertical direction. The number of bins scales with how the sampled data are distributed in the spaces of latitude and jet direction.

The binning and averaging gives a smoothing effect and the climatologies thus show the estimated expected value of each variable around the jets, conditional on the latitude and direction of the jets. The spread in the data is discussed at the end of Sect. 3.6. The results are qualitatively the same when increasing the number of bins.

We focus on eddy-driven jets, but the lowest latitude jets appearing in our analyses are likely of subtropical nature (Lee and Kim 2003). This is the case for both the low-pass and the instantaneous jets (Spensberger et al. 2023). We do not exclude subtropical jets, as we do not have a consistent criterion to do so for both the sector-mean jet detection and the two-dimensional jet detection.

3.5 Latent heating across sector-mean jets

The strongest sector mean winds are found around the respective jet latitudes (Fig. 3.3 a–c) with the pattern in the wind being somewhat smoother and more confined around the 3h-Z compared to the time filtered 1d-Z and 10d-Z jet latitudes. The sector mean winds do, however, show quite large values in a broad latitudinal band around the detected sector-mean jet. This is not unexpected as we compute sector averages over wavy and often tilted jets. The sector mean wind field might also feature several local maxima, which would contribute to the breadth of the wind profile around the identified jet latitude.

As expected from the thermal wind relation, the poleward flanks of the sector-mean jets are colder than the equatorward flanks (Fig. 3.3 a–c). Additionally, few 10d-Z jets are detected poleward of 65° N (see Appendix A.1), causing the volatility in the temperature contours there. Due to the small sample size of 10d-Z jets poleward of 65° N, the patterns there might not be robust and should be interpreted with care.

Two distinct patterns in vertical wind are visible around the sector-mean jets, with one of them being sensitive to the time filtering. The main pattern of vertical wind, which is independent of the time filtering, resembles the Ferrel cell, with descent observed around 30° N and ascent further poleward (Fig. 3.3 d–f). Around the 3h-Z jets poleward of 40° N, we also notice a secondary pattern in the vertical wind featuring

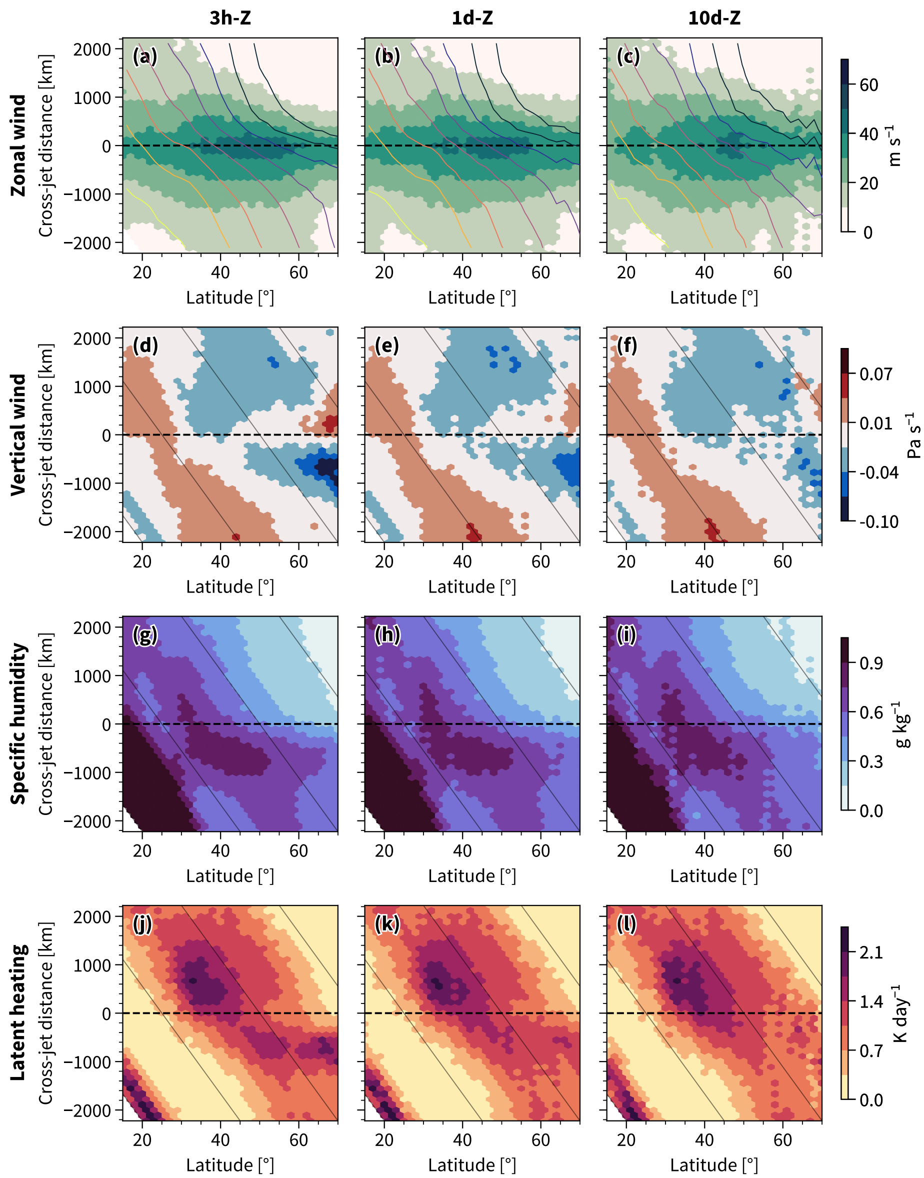

Figure 3.3: The three-hourly zonal wind (2 PVU; a–c), vertical wind (700–200 hPa; d–f), specific humidity (700–200 hPa; g–i), and latent heating (700–200 hPa; j–l) averaged from 60° W to 0° E and shown against the latitude of the concurrent 3h-Z jet (a, d, g, j), 1d-Z jet (b, e, h, k), and 10d-Z jet (c, f, i, l). The jet core is shown by the black dashed line. The grey diagonal lines show constant latitudes for 0, 25, 50, 75° N. The contours in (a–c) show potential temperature at 500 hPa, with intervals 290 (yellow), 295, 300, 305, 310, 315, 320, 325 (black) K.

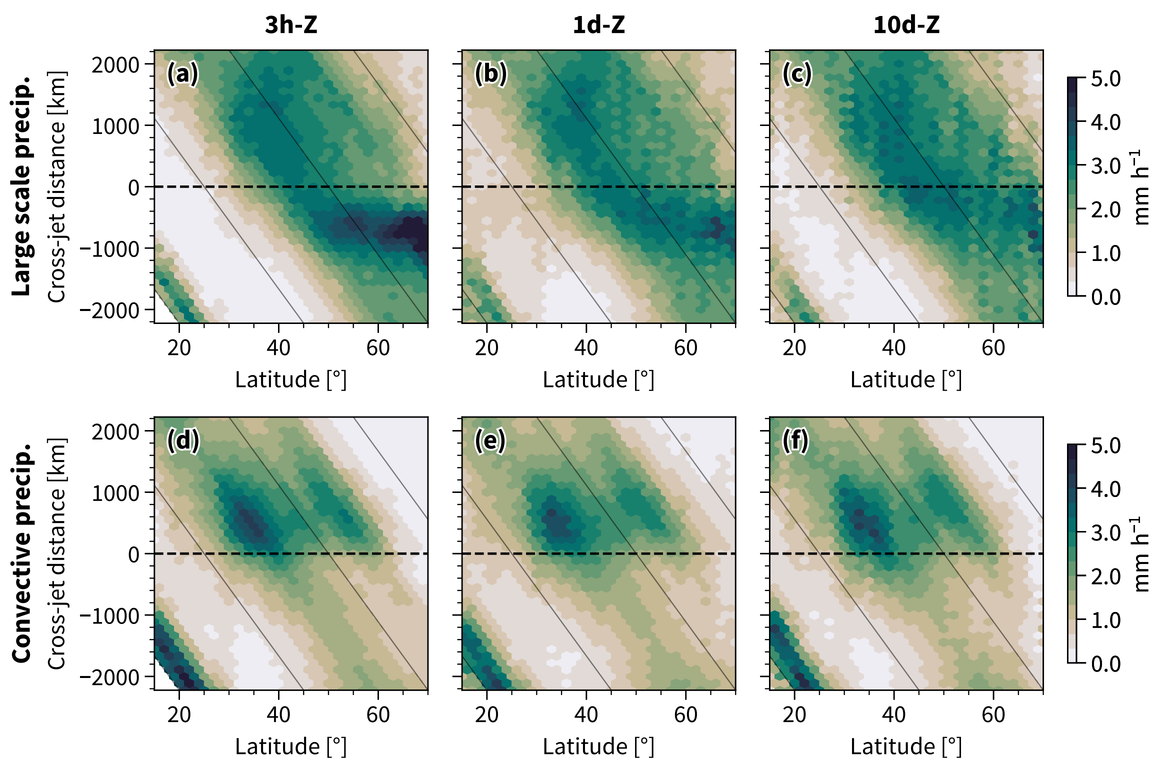

Figure 3.4: This figure is similar to Fig. 3.3 but showing large-scale precipitation (a–c) and precipitation from the ERA5 convection scheme (d–f).

ascent on the warm flank of the jet. The same pattern is visible, but somewhat diluted, for the 1d-Z and only barely visible for the most poleward 10d-Z jets. Hence, the secondary pattern is sensitive to the time filtering.

The distribution of specific humidity, in comparison to vertical wind, is less affected by the time filtering with higher values on the warm flank compared to the cold flank for all the sector-mean jets (Fig. 3.3 g–i).

As mentioned, sector averaging imposes a smoothing effect similar to time filtering, as it averages over several Rossby-wave phases and cyclones. Given the longitudinal confinement of the sector, the zonal distance of averaging decreases with latitude. Hence, the effect of filtering is larger at lower latitudes, which may explain why the zonal wind profile and cross-jet contrast in the vertical wind sharpens at higher latitudes (Fig. 3.3 a–f).

Condensation and thus latent heating typically occur in regions of ascent where moisture is available. Irrespective of time filtering, the sector-mean jets equatorward of $\sim 45^\circ$ N exhibit more latent heating on the poleward flank compared to the equatorward flank (Fig. 3.3 j–k). For jets poleward of $\sim 40^\circ$ N, latent heating follows the aforementioned secondary pattern in vertical wind, which is sensitive to time filtering. As a result, a clear cross-jet contrast in latent heating is seen without time filtering, such that the heating maximum occurs on the equatorward flank of jets poleward of $\sim 40^\circ$ N. At the same latitudes, there is no clear cross-jet contrast in neither vertical wind nor latent heating around the 10d-Z jets.

The sensitivity of the latent heating pattern is congruent with the large-scale precipitation (Fig. 3.4), which spreads out over all latitudes characterised by ascent (Fig. 3.3), while also forming a trail of stronger precipitation on the equatorward flank of the jets poleward of $\sim 40^\circ$ N. Convective precipitation, on the other hand, is first and foremost located on the poleward flank of the sector-mean jets, where the time filtering only slightly affects the pattern (Fig. 3.4). The convective precipitation features a banded latitudinal structure which indicates that it has a strong geographical preference. The larger values around 35–40° N match the climatologically large values of convective precipitation over the Gulf Stream and the cutoff at 60° N coincides with little convective precipitation north of Iceland within the domain of sector zonal averaging (60° W–0° E; not shown).

The relationship we find between the sector-mean jets and latent heating is similar to Xia and Chang (2014). They regressed observed precipitation onto the zonal index in the Southern Hemisphere and found it to follow the poleward flank of the zonal mean jet anomalies. They hence inferred that latent heating weakens the baroclinicity in the anomalous jet. Xia and Chang (2014) use daily data and their finding is consistent with the sector-mean jets equatorward of 40° N (Fig. 3.3 k), given that our results hold for the Southern Hemisphere during summer. Similarly, Bembenek et al. (2020) and Lutsko and Hell (2021) revealed the same negative effect on baroclinicity as deduced from the jets between 30° N–45° N (Fig. 3.3) when analysing the location of precipitation relative to a zonal mean jet. The 10d-Z analysis also resemble Lachmy and Kaspi (2020), who used monthly and zonally averaged values to show that the *eddy driven jet* is shifted equatorward of the largest eddy heat fluxes in winters of strong latent heating. During winters of weak latent heating, they show that the eddy driven jet and the largest eddy heat fluxes are closer in latitude.

3.6 Latent heating around two-dimensional jets

As expected, the wind in the direction of the jet concentrates around the 3h-2D jets, with the wind profile being somewhat sharper on the poleward flank compared to the equatorward flank, exhibiting a clear cross-jet contrast in temperature (Fig. 3.5 a).

The wind is far less concentrated around the 10d-2D jets and has relatively low values for the most poleward located jets, exhibiting a weak cross-jet temperature contrast (Fig. 3.5 b). In other words, the position of the 10d-2D jet is a poor diagnostic for the position of the instantaneous wind.

The distribution of vertical wind around the two-dimensional jets is clearly affected by time filtering. Updrafts are located on the warm flank and downdrafts on the cold flank of the 3h-2D jet axes (Fig. 3.5 c). This is in striking contrast to the sector-mean approach (Fig. 3.3), where the Ferrel cell structure comprises the opposite pattern. It also contrasts the vertical wind distribution around the 10d-2D jets, which appears insensitive to the presence of the jets (Fig. 3.5 d) and similar to the time filtered sector-mean jets, ascent appears to be mainly a function of the jet latitude.

Time filtering has a similar effect on specific humidity. Specific humidity is higher on the warm side for the 3h-2D jets (Fig. 3.5 e), while the specific humidity distribution is insensitive to the presence of 10d-2D jets and, again, is mostly a function of the jet latitude (Fig. 3.5 f).

Latent heating is largest in the region of ascent and higher values of specific humidity (Fig. 3.5 g). In general, more latent heating occurs on the warm flank compared to the cold flank of the 3h-2D jets poleward of 30° N. Some more substantial latent heating on the cold side is seen for jets around 35° N, although still weak in comparison to the warm flank. Similar to vertical motion and specific humidity, latent heating appears independent of the presence of the 10d-2D jets with no clear cross-jet contrast in latent heating visible (Fig. 3.5 h). The insensitivity in vertical wind, specific humidity and latent heating likely follows from the 10d-2D jets poorly representing instantaneous winds and therefore also poorly representing a barrier between cold and warm air. Thus, the 10d-2D jets will be out of phase with the dynamics that drives latent heating.

Similar to the sector-mean jets, it is primarily the large-scale precipitation that

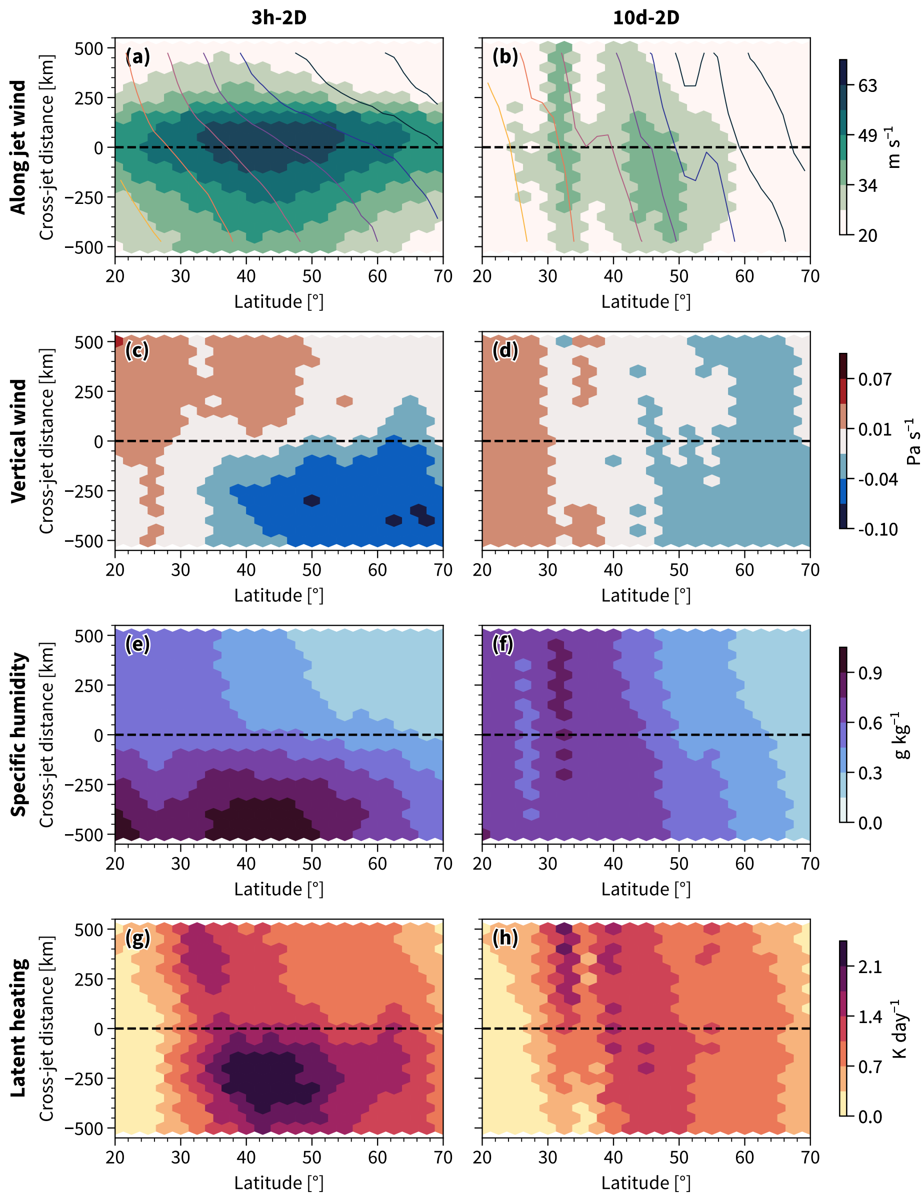

Figure 3.5: The three-hourly winds in the direction of the jet (2 PVU; a–b); vertical wind (700–200 hPa; c–d), specific humidity (700–200 hPa; e–f), and latent heating (700–200 hPa; g–h) interpolated to the cross sections sampled from the two-dimensional jets: 3h-2D (a, c, e, g) and 10d-2D (b, d, f, h). Data are plotted against the latitude of the jet core of each cross section. The warm flanks of the jets lie below the black dashed line and the cold flanks lie above the black dashed line, with this line denoting the jet core.

changes with time filtering around the two-dimensional jets (Fig. 3.6). Large-scale precipitation concentrates on the warm flank of the 3h-2D jets (Fig. 3.6 a), though, similar to latent heating, has no preference for either flank of the 10d-2D jets (Fig. 3.6 b). The large-scale precipitation is generally stronger than the convective precipitation in the two-dimensional jet conditional climatologies. Interestingly, the convective precipitation is co-located with the somewhat more substantial latent heating on the cold flank of the 3h-2D jets around 35° N. Although more convective precipitation is expected around the 3h-2D jets, the convective precipitation pattern is qualitatively similar in 3h-2D and 10d-2D (Fig. 3.6 c, d). This suggests that the time-filtering has less influence on the qualitative relationship between the jet and convective precipitation, compared to large-scale precipitation. For both the 3h-2D and the 10d-2D jets, the convective precipitation is stronger on the cold flank compared to the warm flank, although the cross-jet contrast is subtle for the 10d-2D. The latitudinal stationarity of this signal implies that it is linked to a geographical feature, like the Gulf Stream.

Overall, the distribution of latent heating conditional on the two-dimensional jets is strikingly different to that found by Xia and Chang (2014), Bembenek et al. (2020), and Lutsko and Hell (2021). This has profound repercussions for the interpretation of the effect of latent heating on baroclinicity and jet positioning. Whereas previous studies highlighted detrimental effects of latent heating on the jet, in both the climatological and anomalous positions of the jet, our results based on instantaneous and two-dimensional jets indicate an enhancement of baroclinicity at all latitudes in the extratropics.

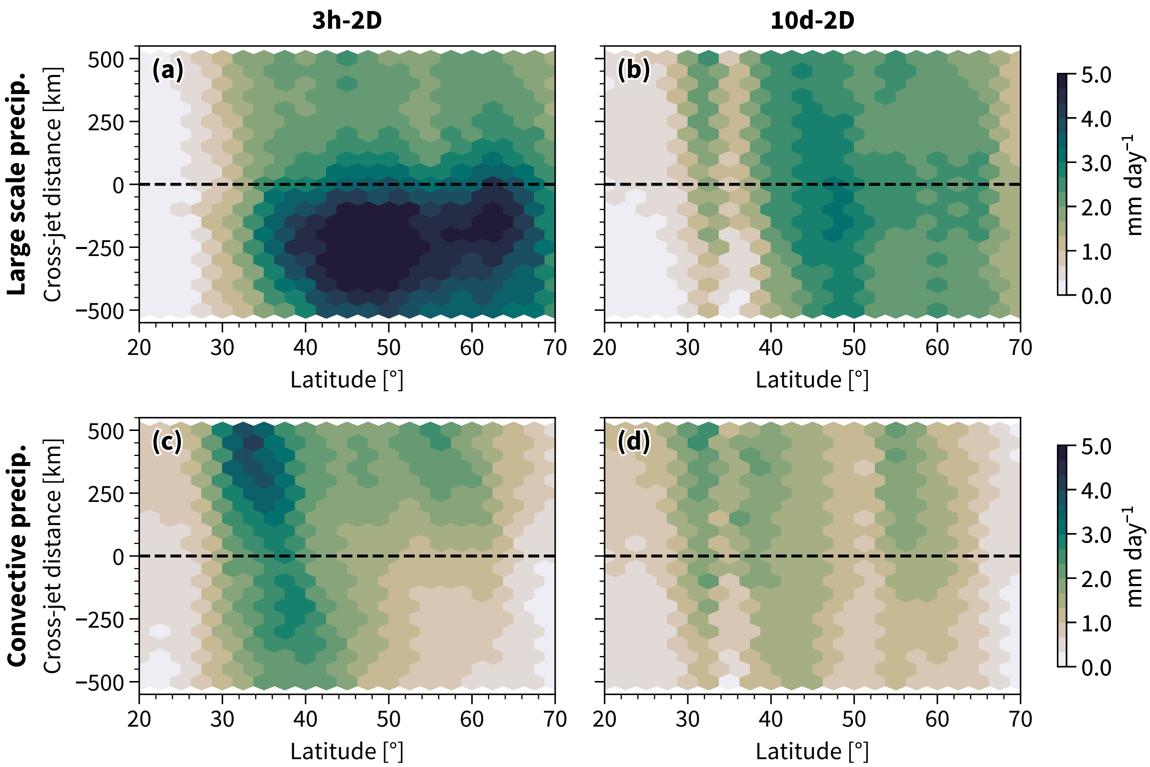

Figure 3.6: This figure is similar to Fig. 3.5 but for large-scale precipitation (a–b) and precipitation from the ERA5 convection scheme (c–d) conditional on the 3h-2D jet axes (a, c) and the 10d-2D jet axes (b, d).

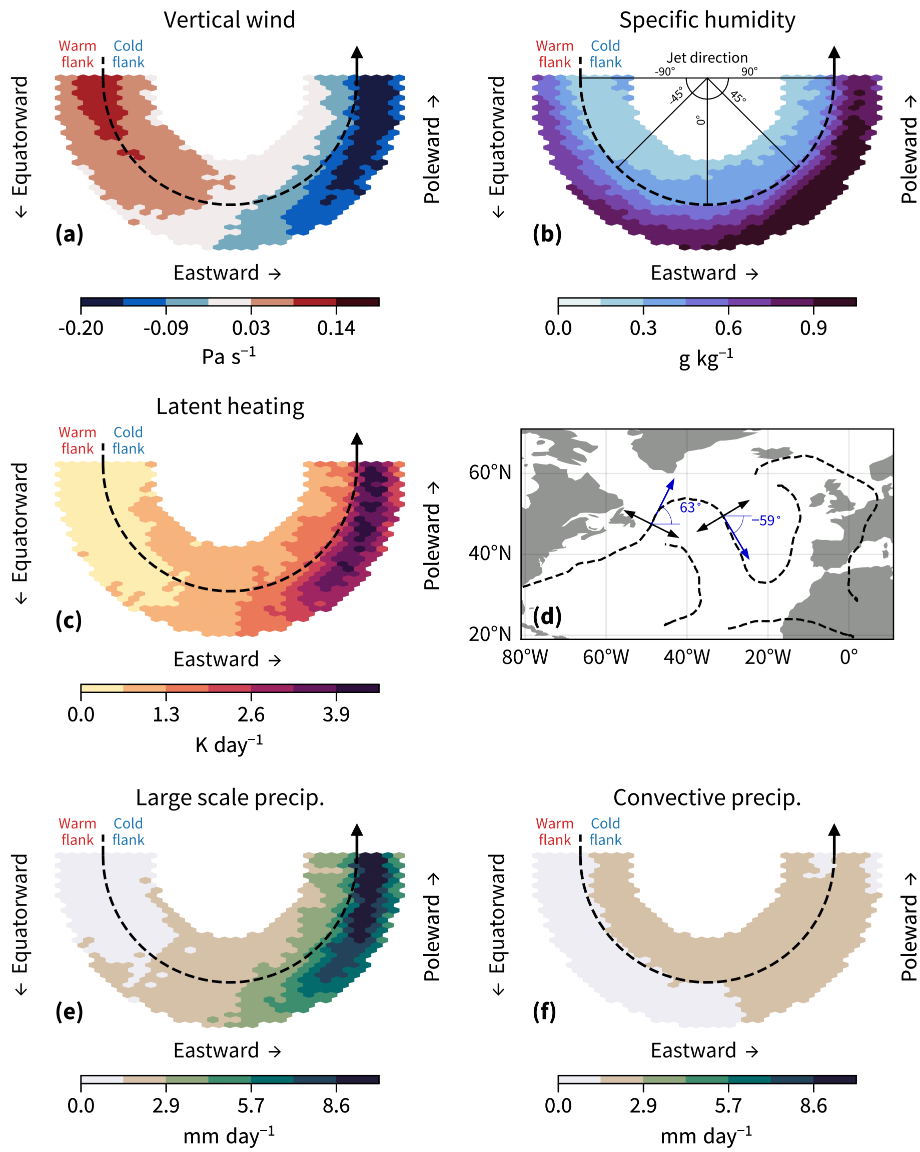

Figure 3.7: Cross sections for vertical wind (a; 700–200hPa), specific humidity (b; 700–200hPa), latent heating (c; 700–200hPa), large-scale precipitation (e), and precipitation from the convection scheme in ERA5 (f) for the 3h-2D jets. The cross sections are sorted by the jet direction and shown with their original orientation in the longitude-latitude plane. The jet directions are parallel to the orientation of the jet core (black dashed line). The angles given in (b) refer to the jet direction. Jet directions with $> 0°$ have a poleward component, with $= 0°$ are perfectly zonal, and with $< 0°$ have an equatorward component. Jet directions of two illustrative cross sections are shown in blue in panel (d). Only jet directions between $-90°$ and $90°$ are shown.

3.7 Latent heating conditional on jet direction

The relationship between jet and latent heating is sensitive to the instantaneous jet direction (Fig. 3.7), suggesting that the two are linked on synoptic time- and spatial scales. As expected from the Clausius–Clapeyron relation, specific humidity is generally higher on the warm flank compared to the cold flank (Fig. 3.7 b). In contrast, ascent and latent heating are strongest along the warm flank of poleward oriented 3h-2D jets (Fig. 3.7 a, c). Equatorward oriented jets are associated with descending motion and very low heating rates. Altogether, this is consistent with the synoptic picture of latent heating occurring in the warm, moist air flowing poleward and upward in warm conveyor belts, producing negative PV on the equatorward flank of jet (Madonna et al. 2014a; Harvey et al. 2020b). Figure 3.7 only shows westerly jets, which make up 90 percent of the 3h-2D jets detected in the NA. Easterly 3h-2D jets are discussed in Appendix A.2.

The location of latent heating relative to the jet core yields a strengthening of the baroclinicity for poleward oriented jets. The increase of baroclinicity (slope of isentropic surfaces) normal to the jet as a consequence of latent heating is confirmed when analysing the diabatic tendency of the isentropic slope (not shown).

The sensitivity of a given variable to the 3h-2D jet direction most likely explains the sensitivity to the spatio–temporal averaging shown above. Given that specific humidity and convective precipitation show similar distributions for all jet directions (Fig. 3.7 b, f), they appear less sensitive to the averaging. Vertical motion (Fig. 3.7 a), latent heating (Fig. 3.7 c), and large-scale precipitation (Fig. 3.7 e), in contrast, are highly sensitive to the orientation of the jet. Thus, when averaging in time and space, the heating appears at a relatively higher latitude compared to the average jet position, even though the heating occurs on the warm flank of the instantaneous jet.

The Lorenz framework is often used to understand baroclinic energetics, by sepa-

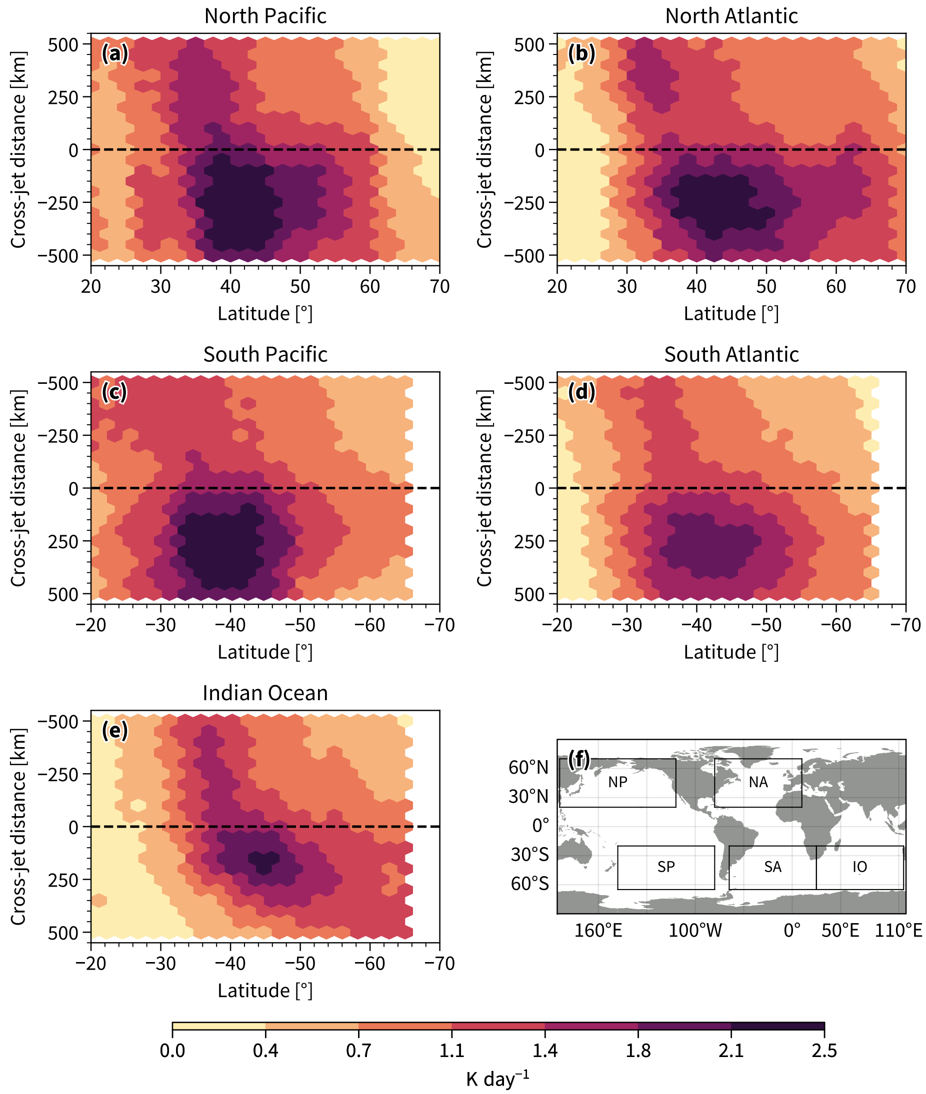

Figure 3.8: This figure is similar to Fig. 3.5 c for 3h-2D jets, showing latent heating for the five major storm track regions indicated in (f) in their respective winter season. The regions are the same used in Spensberger et al. (2023), namely the North Atlantic Ocean (20° N–70° N, 80° W–10° E), the North Pacific Ocean (20° N–70° N, 120° E–120° W), the South Atlantic Ocean (20° S–65° S, 65° W–25° E), the South Pacific Ocean (20° S–65° S, 180° W–80° W), and the Indian Ocean (20° S–65° S,25° E–115° E).

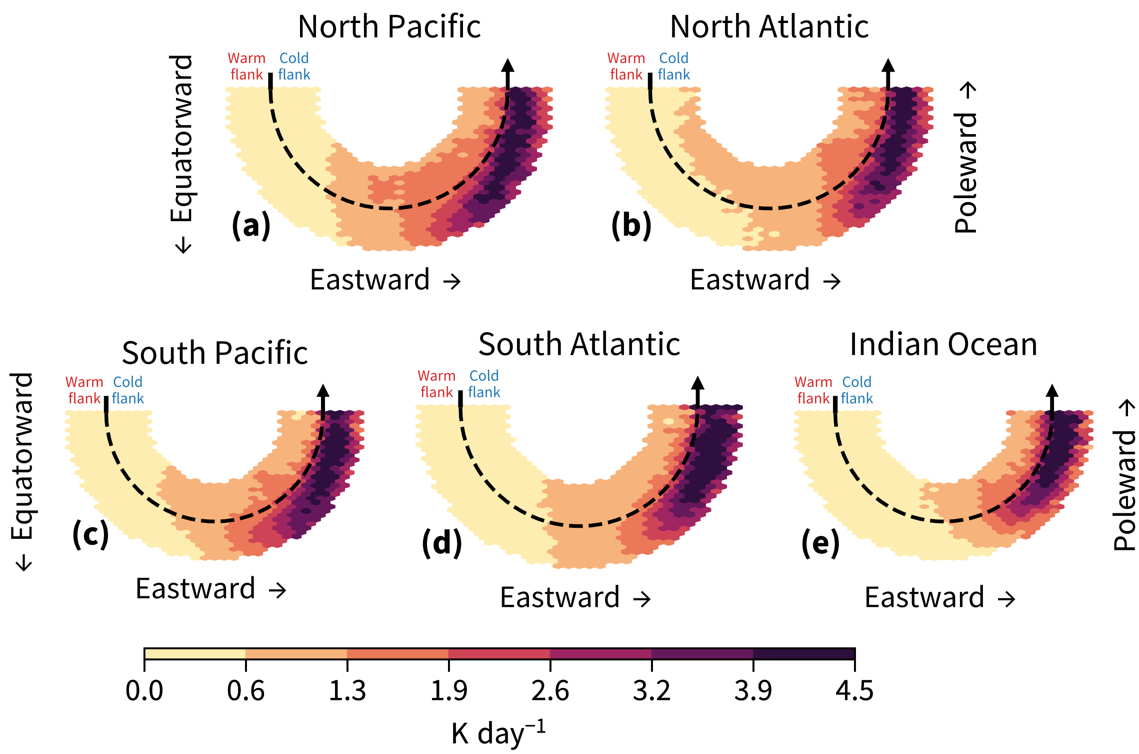

Figure 3.9: This figure is similar to Fig. 3.7 c for 3h-2D jets, showing latent heating for the five major storm track regions (Fig. 3.8 f) in their respective winter season. The axis direction "poleward" is northward in the Northern Hemisphere and southward in the Southern Hemisphere.

rating the flow into mean and eddy components. While diabatic effects weaken the midlatitude mean available potential energy relative to a global reference state (Novak and Tailleux 2018), latent heating is expected to increase mean available potential energy relative to a local reference state (Danard 1966). For latent heating, we showed that a split into mean and eddy components might be misleading, likely due to the asymmetric nature of latent heating with regard to the flow. This is in line with Danard (1966) who argues that the heating occurs in anomalously warm air and strengthens the large scale horizontal temperature gradients in the lower and middle troposphere. Also the isentropic slope budget of Papritz and Spengler (2015) shows that latent heating contributes positively to the overall slope/baroclinicity, and the resulting slope may outlive the original cyclone (Weijenborg and Spengler 2020).

The relationship between latent heating and the 3h-2D jets holds for all the major storm track regions in their respective winters (Figs. 3.8, 3.9) as well as for the other seasons (not shown). Figures 3.8, 3.9 show the mean latent heating across the 3h-2D jets. It is important to note that although the strongest latent heating most often lies on the warm flank of the two-dimensional instantaneous jets, there are still many cases where the reverse is true, which is discussed in Appendix A.1.

3.8 Vertical structure of across-jet latent heating

We have shown that vertically integrated (200–700 hPa) latent heating preferably occurs on the warm flank of the upper-tropospheric 3h-2D jet and argued that this should strengthen baroclinicity in the jet. Figure 3.10 shows the vertical distribution of the latent heating composited according to the jet direction. This shows that updraft and latent heating occurs on the warm side of the jet (left in Fig. 3.10 a, e) from 700 hPa and upwards, leading to an enhanced isentropic slope across the jet (consistent with

Papritz and Spengler 2015; Woollings et al. 2016; Marcheggiani and Spengler 2023).

There is also a clear signature of diabatic heating on the cold side of the jet at lower levels (below 700 hPa; Fig. 3.10 a, c, e). This is likely caused by surface sensible heat fluxes and subsequent turbulent mixing in the boundary layer. The effect of surface fluxes on baroclinicity is discussed in other works (e.g. Swanson and Pierrehumbert 1997; Papritz and Spengler 2015; Marcheggiani and Spengler 2023).

The differences in equivalent potential temperature (following Bolton 1980) to the potential temperature on the warm side of the poleward jets is due to water vapour (see right panels of Fig. 3.10). Consistent with Pauluis et al. (2010), ascent occurs where the difference in lower level equivalent potential temperature to the upper level potential temperature is small, and the the air therefore being close to convectively unstable.

3.9 Concluding remarks

We analysed the across-jet distribution of latent heating, wind speed, humidity, and precipitation for two different types of jet definitions, one based on sector zonal mean zonal wind and one considering the two-dimensional structure of the wind field (Spensberger et al. 2017). We applied these definitions to both low-pass filtered and instantaneous data.

We find that latent heating occurs preferentially on the warm flank of the two-dimensional instantaneous jet (Fig. 3.7), consistent with Papritz and Spengler (2015) and Woollings et al. (2016), who argued that latent heating mainly acts to increase baroclinicity. Conversely, for spatio-temporally averaged jets, the latent heating largely shifts to the cold side of the jet (Fig. 3.3). This dichotomy is due to latent heating primarily occurring on the warm flank of poleward oriented instantaneous jets, whereas latent heating appears distributed across the jet in a spatial and time mean view. Given that Xia and Chang (2014) base their arguments on spatio-temporally averaged data, the conflicting results with Woollings et al. (2016) are most likely attributable to the sensitivity of the latent heating jet relationship to spatio-temporal averaging.

Consistent with the Clausius–Clapeyron relation, we find that specific humidity is higher on the warm flank of the jet, irrespective of jet orientation and jet definition (Figs. 3.3, 3.5, 3.7). Vertical wind, on the other hand, is sensitive to the spatio-temporal averaging, which is likely related to upward motion being associated with poleward oriented instantaneous jets and downward motion with the equatorward oriented jets (Fig. 3.7).

As latent heating is contingent on moist air being lifted, the across-jet sensitivity of latent heating to spatio–temporal averaging thus stems from the asymmetric response in vertical wind to jet direction. This is also reflected in the large-scale precipitation, which exhibits the same sensitivity to spatio-temporal averaging as latent heating and vertical wind (Fig. 3.6). Hence, variables that are independent of jet direction (e.g., specific humidity) are more robust to averaging techniques than variables that depend on the jet direction (e.g., vertical wind).

Given that the jet-relative position of latent heating is sensitive to both spatio-temporal averaging and the jet definition, the physical interpretation of the effect of latent heating is similarly sensitive. While latent heating primarily enhances baroclinicity in a two-dimensional instantaneous jet framework, a zonalisation of the jet due to its definition or spatio-temporal averaging yields a reduction in baroclinicity due to latent heating. However, given that most of the latent heating (precipitation) in the mid-latitudes is driven by synoptic features (Konstali et al. 2024), any definition or spatio-temporal averaging of the jet that masks the synoptic nature of the latent heating-jet relation yields a potentially physically misleading interpretation.

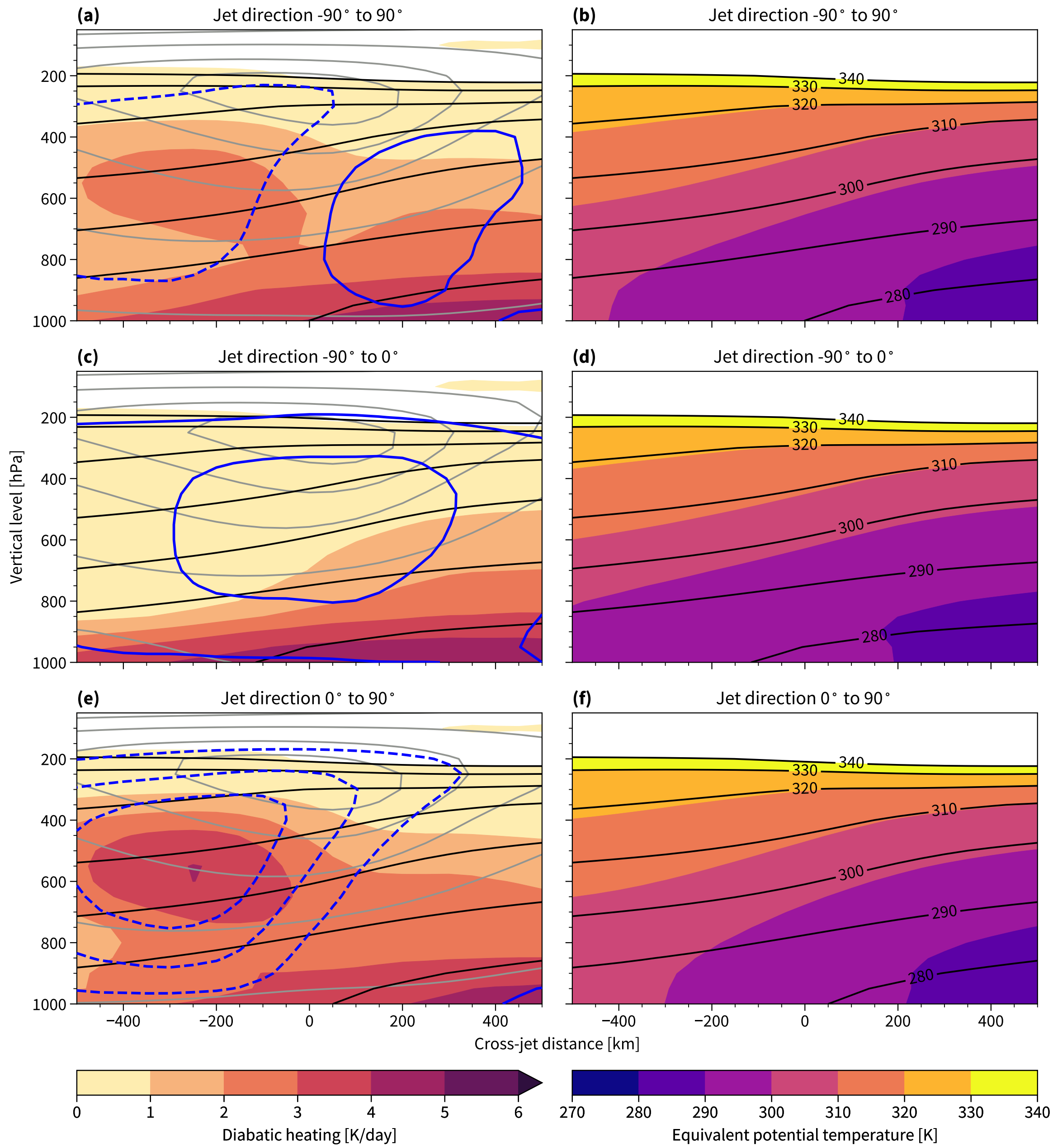

Figure 3.10: Diabatic heating (except radiation; a, c, e; shading), wind in jet direction (grey contours), isentropes (black contours), and vertical wind (blue contours) averaged over composites of the 3h-2D cross sections conditioned on the jet direction. Also shown is the equivalent potential temperature (b, d, f; shading). See Fig. 3.7 and the text for further explanation of the jet direction. The dashed blue contours show updraft while solid blue contours show downdraft. The contour intervals for vertical wind are -0.1, -0.06, -0.02, 0.02, 0.06, 0.1 Pa s^{-1} and for the wind in the jet direction 5, 15, 25, 35, 45, 55 m s^{-1}. Isentropes are identical on each row.

Chapter 4

The latent heating feedback on the midlatitude circulation

This chapter is based on Auestad et al. (2025). We demonstrated that latent heating is organised by the synoptic circulation (Chapter 3). Because latent heating, in turn, modifies temperature gradients and winds, the relationship between dynamics and latent heating should constitute a nonlinear feedback loop. In this chapter, we define the *latent heating feedback* as the coupling between latent heating and the circulation.

Because of the nonlinearity, the climatic effects of this feedback are difficult to isolate and remain poorly understood. By decoupling latent heating from the circulation in an atmospheric general circulation model, we show that the latent heating feedback enhances storm track eddy diffusivity, modifying eddy heat fluxes beyond changes in mean baroclinicity. Simultaneously, tracked storms occur at lower latitudes, intensify more, and propagate further poleward, while the subtropical jet strengthens as coupled latent heating preserves lower latitude baroclinicity. The feedback response supports the idea that diabatic effects cause the "too zonal, too equatorward" storm track biases in climate models (Schemm 2023).

4.1 Introduction

The time mean latent heating in the midlatitude storm tracks forces a zonally varying mean state both forcing and interacting with the stationary wave pattern (Held et al. 2002; Kaspi and Schneider 2013). However, storm-track latent heating is not static but occurs in poleward moving and ascending warm and moist air masses (Chapter 3; Pauluis et al. 2010). Thus, condensation is organized by the dynamics and the consequential latent heat release feeds back on the dynamics by enhancing ascent and modifying temperature gradients. We here define the specific impact of latent heating being coupled with the dynamics, as distinct from a static time-mean forcing mimicking latent heating, the *latent heating feedback*.

On synoptic and shorter timescales, in the lower troposphere, latent heating enhances the ascent in which it occurs and modifies static stability leading to stronger and smaller cyclones (Emanuel et al. 1987; O'Gorman 2011; Booth et al. 2013; Tierney et al. 2018). In the upper troposphere, latent heating sharpens potential vorticity gradients and jets (Harvey et al. 2020b; Bukenberger et al. 2023) and enhances the vertical advection of low potential vorticity air, amplifying negative upper-tropospheric potential vorticity anomalies (Madonna et al. 2014a; Methven 2015) that may promote anticyclonic Rossby wave breaking (Madonna et al. 2014b; Zhang and Wang 2018) and maintain blocks (Pfahl et al. 2015a).

Of relevance for timescales beyond synoptic, Hoskins and Valdes (1990) suggested that latent heating maintains baroclinicity, energizing the storm track. The effect of latent heating on baroclinicity has since been debated (Laîné et al. 2011; Xia and Chang 2014; Papritz and Spengler 2015; Woollings et al. 2016; White et al. 2024; Chapter 3): instantaneous data indicate that latent heating strengthens baroclinicity, while spatio-temporally averaged data suggest a weakening.

This chapter aims to demonstrate the existence of the latent heating feedback and understand how it influences jets and storm tracks on climatic timescales. Due to its nonlinearities, it is difficult to examine the latent heating feedback in isolation in integrated climate simulations. Schemm (2023) suggested that a realistic representation of latent heating is important for capturing the climatological storm track tilt downstream of a sea surface temperature front, consistent with how latent heating is expected to enhance the poleward propagation of cyclones (Tamarin and Kaspi 2016). Hermoso et al. (2024) showed that increasing latent heating shifted the jet poleward over the Gulf Stream extension in reanalysis from 1979-2022, while simultaneously leading to an equatorward shift downstream via its effect on eddy momentum fluxes, suggesting that the effects are regional.

To examine the regional climatic effects of the latent heating feedback in isolation, we introduce an experimental design where latent heating is decoupled from the dynamics only in the extratropics. We show that the latent heating feedback strengthens the subtropical jet in a zonally symmetric fashion. At the same time, cyclones grow faster and stronger and propagate more poleward in regions of a weak subtropical jet. In these regions, the polar jet is strengthened, causing a more tilted storm track and jet.

4.2 Methods

4.2.1 Model

We run the Community Atmosphere Model 4.0 (CAM4), an atmospheric model component of the Community Earth System Model (Neale et al. 2013), with topography and seasonally varying prescribed climatological sea surface temperatures from the period 1995-2005 (Hurrell et al. 2008). The model uses the finite volume method and has a 0.9-degree meridional grid spacing, a 1.25-degree zonal grid spacing and 26 vertical levels. Using ARCHER2 (Beckett et al. 2024), we run the experiments for 50 years, following one year of spin-up that is discarded.

Experimental setup

To examine the latent heating feedback, we run a model experiment where the latent heating is decoupled from the dynamics. The temperature tendencies produced by the CAM4 shallow convection scheme (Hack 1994), deep convection scheme (Zhang and McFarlane 1995), and the micro-physics scheme (Rasch and Kristjánsson 1998) constitute the temperature tendencies due to condensation and evaporation. This temperature tendency, referred to as *latent heating*, includes condensation due to resolved and parametrised convection and can be negative due to evaporation (Fig. 4.1). While decoupling latent heating, the other diabatic tendencies (e.g. radiation) are left to evolve freely. Decoupling latent heating causes some changes in the other diabatic terms, which contribute to the zonal mean temperature budget (following Lachmy and Kaspi 2020, see Figs. B.5–B.6 in Appendix B.2).

We decouple latent heating by replacing the real-time latent heating with the monthly mean latent heating in the control run, analogous to prescribing sea surface temperature (SST). The mean latent heating is calculated and prescribed at every individual grid point on model levels (sigma-hybrid). The prescribed latent heating follows the seasonal cycle, so the climatological January latent heating in the control run is prescribed to January in the decoupled run (Fig. 4.1 b, c).

To minimize the effect of decoupling on the Hadley circulation, latent heating is only prescribed outside of the tropics. We define the tropics as where the 200 hPa control run eddy kinetic energy is smaller than the respective hemispheric median eddy kinetic energy. Eddy kinetic energy is given by $(1/2)(u'^2 + v'^2)$, where the primes denote

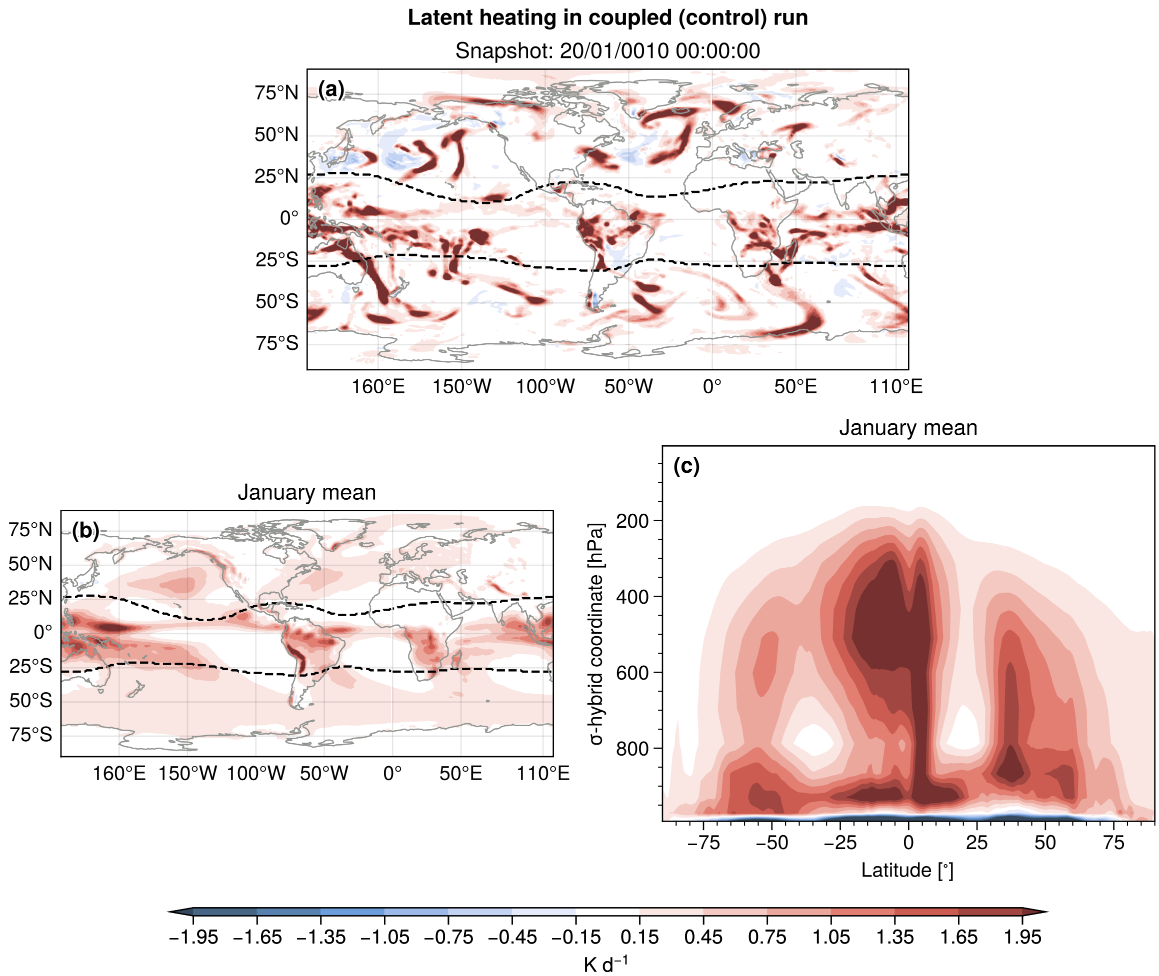

Figure 4.1: Latent heating in the coupled (control) run for a snapshot in time (a) and the January average (b, c). Using all model levels, the unweighted vertical average latent heating is shown in panels a and b and the zonally average is shown in panel c. The black dashed lines (a, b) show the tropical-extratropical boundaries defined in the text. The colourbar refers to all panels.

high pass filtered six-hourly values with a 10-day cut-off period, using a 243 point Lanczos filter (Duchon 1979). Before calculating the tropical-extratropical boundaries, we smooth the eddy kinetic energy by applying a three-month running mean and a 21-grid point running mean, the latter on both the meridional and zonal dimensions. The calculations are done for each month, such that the boundaries follow a seasonal cycle. This is a pragmatic definition of the tropics that allows for only decoupling latent heating where extratropical cyclones exist climatologically. The dashed lines in Fig. 4.1 a, b show these boundaries for January.

Additionally, the decoupling is only applied above the boundary layer, reading the boundary layer height at every time step. Boundary layer processes involve a mixture of sensible and latent heating, as well as cooling by evaporation (Fig. 4.1 c). Fixing the latent heat exchange disturbs the energy balance in the boundary layer mixing processes, which we thus avoid. However, we also performed decoupled simulations where extratropical boundary layer latent heating is set to zero and where extratropical latent heating is decoupled throughout the vertical extent of the model. The results are qualitatively similar, which builds confidence in the robustness of the experimental set-up and suggesting that latent heating in the free troposphere is more relevant than boundary layer latent heating for shaping the climatological circulation (not shown).

4.2.2 Data

Model outputs are stored on the native spatial model grid before being interpolated to 14 vertical pressure levels using logarithmic interpolation. We store the three-dimensional wind field, specific humidity, geopotential height, total diabatic temperature tendency (referred to as *diabatic heating*) and latent heating at six-hourly time steps.

Feature tracking

We track cyclones using the TRACK algorithm (Hodges 1994; Hodges 1995; Hodges 1999) on 850 hPa vorticity after applying a T42 truncation and removing spatial wave numbers smaller than or equal to 5. We only analyze features that persist longer than 2 days and travel further than 1000 km. We require relative vorticity to be greater than 10^{-5} s^{-1} in the Northern Hemisphere and smaller than -10^{-5} s^{-1} in the Southern Hemisphere to identify a cyclone. On the set of tracked cyclones, we compute the cyclone track density, genesis and lysis densities, cyclone propagation velocity, cyclone area and intensity for December, January, and February for each model year using spherical nonparametric estimators (Hodges 1996). Similar to Priestley et al. (2020), the track, genesis, and lysis densities are computed as the number of cyclones per month over an area equivalent to a 5° spherical cap, with genesis and lysis densities only considering the first and last time step of the cyclone track, respectively. The growth rate is in the units of day^{-1}, similar to the Eady growth rate and the intensity is taken as the maximum T42 relative vorticity on 850 hPa during the cyclone lifetime. The cyclone area comprises the connected set of grid points defined by starting at the maximum 850 hPa vorticity in the cyclone and recursively searching for and connecting grid points of lower vorticity. In cases where the cyclones exist within two or more months, they are counted in the month they spend most of their lifetime.

Statistical testing

To assess the statistical significance of the changes between the two experiments, we apply a two-sided Welch t-test on the monthly mean values of the data and the seasonal storm track statistics. We control the false discovery rate at a 0.05 level of significance to account for testing at multiple grid points (Wilks 2016). The data points that reject the null hypothesis; that the expected value is the same, are referred to as 'significant'. For the tracked cyclones, grid points with less than two features per month per 5° spherical cap in either experiment are automatically labelled 'insignificant'.

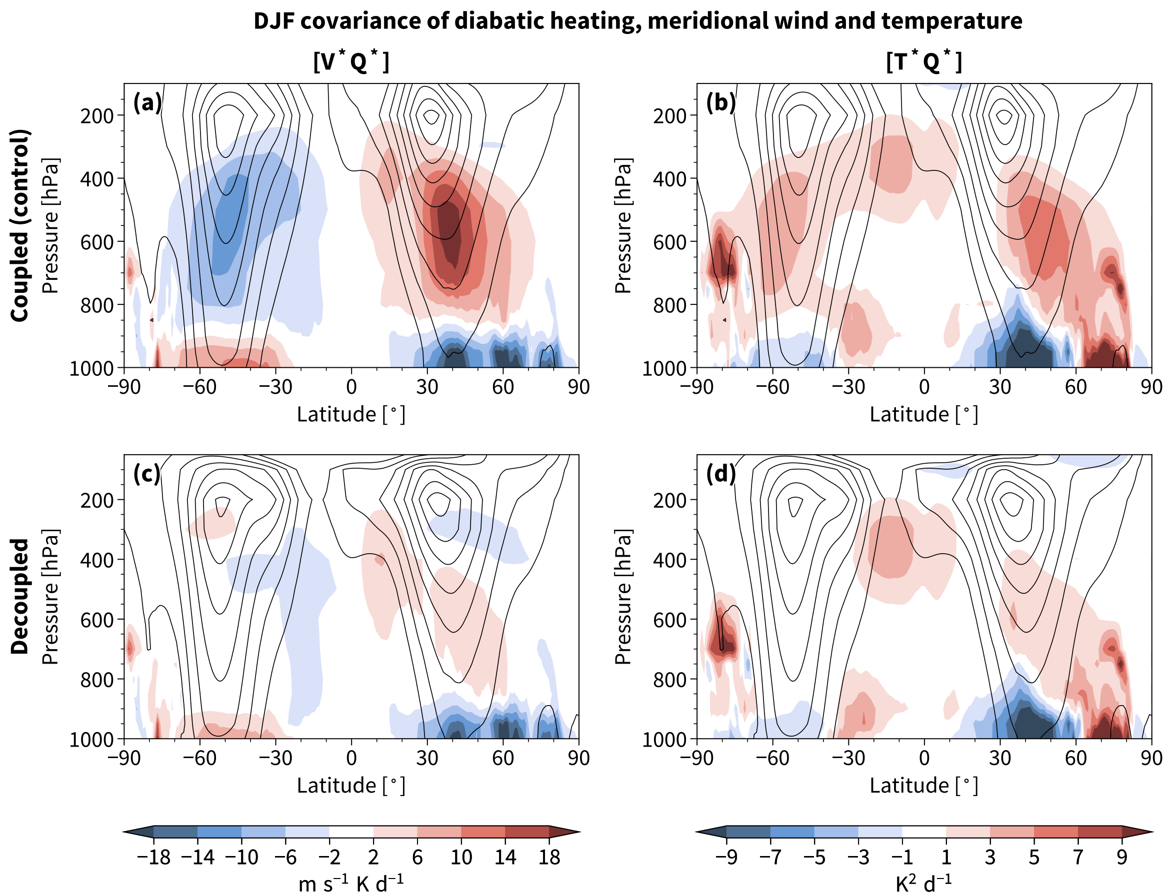

Figure 4.2: The covariance between the full diabatic heating (Q) and meridional wind (V; a, c, shading). The covariance between full diabatic heating and temperature (T; b and d, shading). The zonal mean zonal wind is shown for reference in black contours with intervals $5, 10, ..., 50$ m s^{-1}. Values are averaged over December, January, and February.

4.3 Results

4.3.1 Decoupling latent heating from wind and temperature

The time mean latent heating on model levels is by construction identical in the control and the decoupled runs (not shown). For snapshots in time, however, the latent heating will be dramatically different (Fig. 4.1). In the control run, which we will be referring to as the 'coupled' run, latent heating is patchy, like the spatio-temporal distribution of clouds and precipitation. In the decoupled run, extratropical latent heating is fixed to a smooth and seasonally varying profile.

As a consequence of decoupling, the covariances between the full diabatic heating, meridional wind, and temperature dampen in the midlatitude free troposphere (Fig. 4.2). The anomalies (asterisks) used to compute the covariances are deviations from the zonal mean (brackets). In the coupled run, diabatic heating is positively correlated with poleward wind and temperature in the free troposphere and negatively correlated close to the surface (Fig. 4.2 a, b). This is consistent with free troposphere latent heating in poleward warm air advection and sensible heating of colder air over warmer ocean at the surface. Prescribing free tropospheric latent heating reduces the amplitude of the full diabatic heating anomaly and thus largely reduces the covariances in the free troposphere (Fig. 4.2 c, d).

4.3.2 Coupling enhances eddy heat flux efficiency

We have shown how decoupling latent heating changes the covariance of latent heating against wind and temperature. However, decoupling also changes the covariance of temperature and meridional wind (Fig. 4.3 d). In the following sections, to assess the effects of latent heating being coupled with the dynamics, we examine the differences

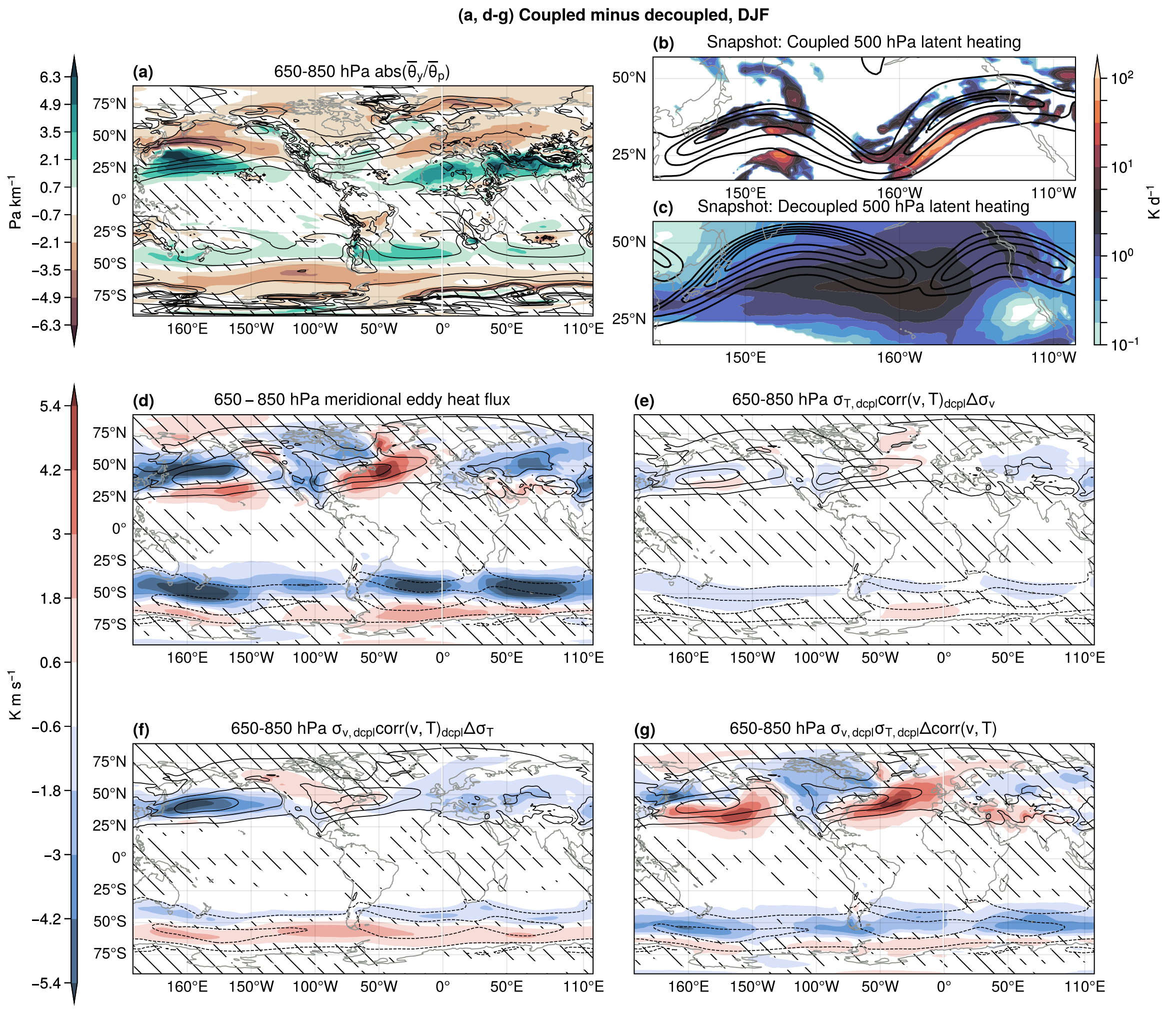

Figure 4.3: The coupled minus decoupled difference in 650-850 hPa baroclinicity (a), meridional eddy heat flux (d), and the linear contributions to the meridional eddy heat flux changes from changes in the meridional wind (e), the temperature (f), and the correlation between meridional wind and temperature (g). The black contours show the climatological values in the decoupled run, with intervals 5, 10, 15, 20 Pa km^{-1} (a) and ± 3.5, 10.5, 17.5 K m s^{-1} (d–g). Values are averaged over December, January, and February and changes in the un-hatched grid points are significant (a, d–g). Panels (b, c) show 500 hPa latent heating (shading) and 300 hPa wind speed (contours; $40, 55, ..., 100$ m s^{-1}) for illustrative snapshots taken from February over the North Pacific.

between coupled and decoupled runs, where the latter is the baseline.

In the coupled run, the poleward lower-tropospheric eddy heat flux ($\overline{v'T'}$) increases in the North Atlantic and on the equatorward flanks of the North Pacific and Southern Hemisphere storm tracks compared to the decoupled run (Fig. 4.3 d). Simultaneously, the poleward eddy heat flux decreases over the continents and on the poleward flank of the North Pacific storm track. In this section, primes denote anomalies from a 10-day running mean (overbar).

The equatorward shift in eddy heat flux in the Southern Hemisphere and North Pacific can be explained by an equatorward shift in background baroclinicity ($|\overline{\theta}_y/\overline{\theta}_p|$). We compute baroclinicity from potential temperature with a 10-day running mean applied to it ($\overline{\theta}$) to represent the mean temperature gradient that the eddy heat fluxes interact with (Drouard et al. 2015).

We hypothesize that baroclinicity shifts equatorward in the coupled simulation due to realistic storm track latent heating typically occurring in the warm poleward moving air, east of troughs, on the warm side of the synoptic jets (Fig. 4.3 b and Fig. 3.7 c). While the heating occurs at relatively high latitudes it does so within air masses that, except when the synoptic wave breaks, are only temporally displaced poleward. Thus, baroclinicity is maintained in relatively low-latitude air masses compared to the decoupled run, where baroclinicity is artificially increased at higher latitudes due to the unrealistic heating of cold, dry, high-latitude air masses by the prescribed latent heating (Fig. 4.3 c).

In the North Atlantic, however, the eddy heat flux increase is disproportionate to the changes in baroclinicity (Fig. 4.3 a, d). If the eddy heat flux were to be driven by a flux-gradient relationship, this would take the form

$$\overline{v'T'} = -\kappa \partial \overline{T} / \partial y, \tag{4.1}$$

where κ is an eddy diffusivity. The mean temperature gradient $(-\partial\overline{T}/\partial y)$ behaves similarly to our baroclinicity measure and thus, baroclinicity changes qualitatively explain the meridional dipole changes in eddy heat flux in the North Pacific and Southern Hemisphere storm tracks. In the North Atlantic, however, the increase in eddy heat flux does not follow the changes in baroclinicity.

To examine the changes in eddy character and diffusivity, we decompose the eddy heat flux into the product between the standard deviation of the meridional wind and temperature, and the correlation between the two,

$$\overline{v'T'} = \sigma_v \sigma_T corr(v, T). \tag{4.2}$$

The changes in eddy heat flux are further decomposed into linear contributions from changes in meridional wind, temperature, the correlation and a non-linear residual (R),

$$\Delta\overline{v'T'} = \sigma_v \sigma_T \Delta corr(v, T) + corr(v, T)\sigma_T \Delta\sigma_v + corr(v, T)\sigma_v \Delta\sigma_T + R. \tag{4.3}$$

Of these terms, the change in correlation explains most of the changes in the eddy heat flux from the decoupled to the coupled simulation (Fig. 4.3 g). In the North Pacific, North Atlantic, and Southern Hemisphere storm tracks the coupling between meridional wind and temperature is improved by realistic latent heating and eddies transport heat poleward more efficiently. Over the Northern Hemisphere continents, in contrast, the correlation weakens and the poleward energy transport becomes less efficient.

The temperature anomalies mostly weaken in the coupled experiment, reducing the storm track eddy heat fluxes, which is largely consistent with the differences in baroclinicity (Fig. 4.3 a, f). Changes in the meridional wind (Fig. 4.3 e) are small and the residual is negligible (not shown), not contributing much to the eddy heat flux changes between the two experiments.

4.3.3 Coupling causes stronger and more poleward propagating storms

In the storm tracks, the eddy heat flux is largely accomplished by cyclone growth and heat transport. Consistent with the changes in eddy heat flux, cyclones grow more intense when latent heating is coupled (Fig. 4.4 a).

Cyclone size also decreases in the main storm track regions in both hemispheres (Fig. 4.4 b). This is consistent with coupled latent heating leading to stronger but horizontally smaller regions of ascent (Emanuel et al. 1987; O'Gorman 2011; Booth et al. 2013; Tierney et al. 2018). Simultaneously, cyclone size increases in the subtropics (significantly in the Southern Hemisphere), which could reflect an equatorward shift of larger systems within the storm tracks.

Constituting an equatorward shift of the storm tracks, coupling increases the number of cyclones on the equatorward flank of the decoupled storm tracks, where also cyclogenesis increases (Fig. 4.4 c, d). In the North Atlantic and eastern North Pacific, where the climatological storm track is northeastward tilted, cyclolysis weakly increases around 60-70° N (Fig. 4.4 e).

Bridging the Northern Hemisphere increase in cyclogenesis (30-40° N) and lysis (60-70° N), the cyclones propagate more poleward in the climatologically tilted storm track regions when latent heating is coupled (Fig. 4.4 f). Cyclones also propagate more poleward in the Southern Hemisphere when latent heating is coupled, but less regionally confined and in a more zonally symmetric fashion compared to the Northern Hemisphere.

The enhanced poleward propagation is consistent with the effect of latent heating on lower-tropospheric potential vorticity relative to the cyclone core and the general increase in cyclone growth rate with coupled latent heating (Tamarin and Kaspi 2016).

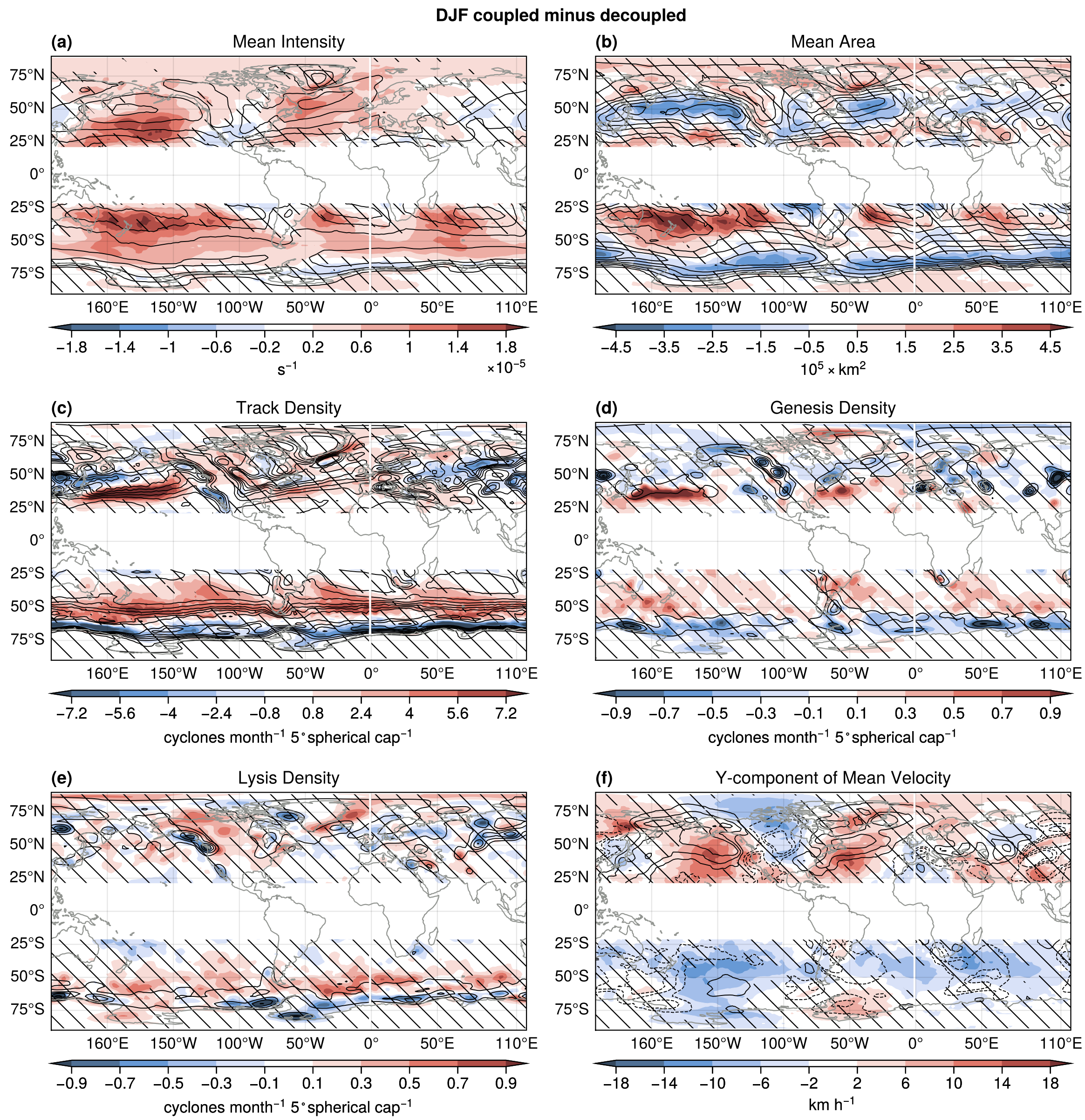

Figure 4.4: The coupled minus decoupled difference in cyclone intensity (a), cyclone area (b), track density (c), genesis density (d), lysis density (e), and mean meridional propagation velocity (f). The black contours show the climatological values in the decoupled run, with intervals 1, 2, 3, 4, 5, 6 $\times$ 10^{-5} s^{-1} (a), 2.5, 5, 7.5, 10, 12.5, 15, 17.5 $\times$ 10^5 km^2 (b), 1, 4, 7, 10, 13, 16, 19 cyclones month^{-1} 5° spherical cap^{-1} (c), 1, 2, 3, 4, 5 cyclones month^{-1} 5° spherical cap^{-1} (d, e), and -15, -10, -5, 5, 10, 15 km h^{-1} (f). Values are from December, January, and February and changes in the un-hatched grid points are significant.

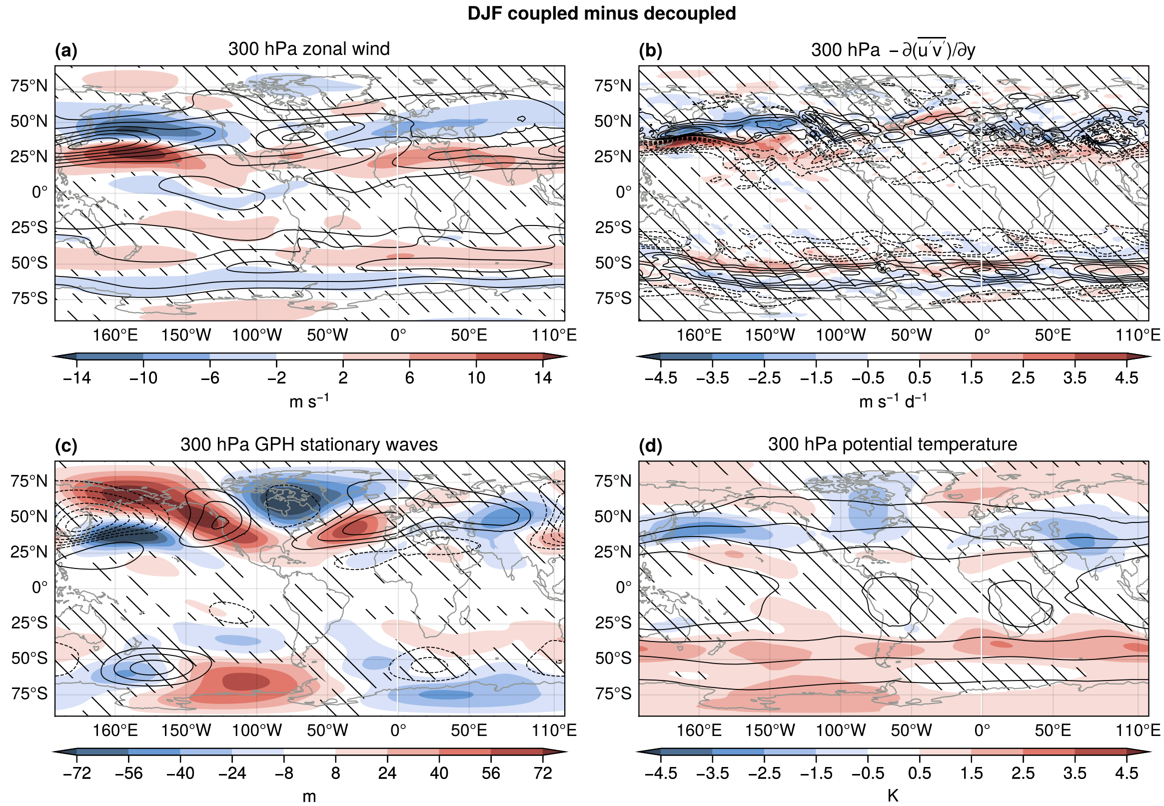

Figure 4.5: The coupled minus decoupled difference in 300 hPa zonal wind (a), 300 hPa meridional eddy momentum flux convergence (b), 300 hPa geopotential height stationary waves (c), and 300 hPa potential temperature (d). Climatological values in the decoupled run are shown in black in contours with intervals 10, 20, ..., 60 m s^{-1} (a), $\pm$1, 2, ..., 5 m s^{-1} d^{-1} (b), $\pm$50, 100, ..., 300 m (c), and 310, 320, 330, 340 K (d). Values are averaged over December, January, and February and changes in the un-hatched grid points are significant.

The equatorward shift of the storm tracks, primarily the North Pacific and the Southern Hemisphere shift equatorward, is less intuitive and discussed next.

4.3.4 Coupling shifts the mean jet equatorward and 'splits' it

Like the storm tracks, the time mean jet shifts equatorward in the North Pacific and Southern Hemisphere when latent heating is coupled (Fig. 4.5 a). The signal is not limited to the storm tracks but is largely zonally symmetric and visible in the lower troposphere (not shown).

The equatorward jet shift likely follows the coupling-induced equatorward shift in baroclinicity, discussed in Section 3.2: latent heating in the subtropical air maintains baroclinicity, and thus a jet, at lower latitudes (Fig. 4.3 a). Consistently, cyclogenesis increases at lower latitudes in the coupled run (Fig. 4.4 d) and the transient meridional eddy momentum flux convergence shifts equatorward with the jet, indicating more poleward eddy propagation from the lower genesis latitudes, leaving a stronger time mean subtropical jet (Fig. 4.5 b).

With coupled latent heating, a tendency for 'split jets' emerges over the North Atlantic and the eastern North Pacific. In these regions, the storm track tilt is enhanced by coupled latent heating (Fig. 4.4 f). The split jet tendency features reduced westerlies around 45° N and enhanced westerlies further poleward, further tilting the time mean jet. The reduced westerlies could also indicate more or stronger blocking events, consistent with the latent heating effect on blocks (Pfahl et al. 2015a).

Via its non-linear relationship with the dynamics, the transient latent heating shapes the time mean zonally asymmetric circulation as expressed by stationary waves. The stationary waves are computed as anomalies in monthly mean geopotential height from the zonal average ($\overline{z}^* = \overline{z} - [\overline{z}]$). The equatorward jet shift in the western North Pacific manifests as a meridional shift in the stationary wave pattern (Fig. 4.5 c). The enhanced poleward propagation of storms and 'split-jet' tendency in the eastern North Pacific and North Atlantic projects onto the stationary wave pattern by amplifying the ridges there and the trough over North America.

We finally note that our results are robust to the method of decoupling. Solomon (2006) decoupled latent heating by redistributing the heating over zonal bands. The experiment of Solomon (2006) shows that coupling latent heating enhances eddy heat fluxes, causing an upper-tropospheric polar amplification in the Northern Hemisphere and generally warmer upper-tropospheric temperatures in the Southern Hemisphere in December-February, similar to our results (Figs. 4.3 d and 4.5 d). The upper-tropospheric warming results from ascending air parcels following the moist adiabatic lapse rate in the coupled run, which increases mean static stability (not shown; Juckes 2000). Appendix B.1 contains June, July, and August versions of Figs. 4.2–4.5.

4.4 Summary and discussion

Latent heating within the storm tracks feeds back on the circulation over a range of spatio-temporal scales. Here, we demonstrate the climatological latent heating feedback effect in an atmosphere-only model (CAM4) by comparing a run with realistic latent heating (coupled experiment) against a run with latent heating prescribed in the extratropics (decoupled experiment).

To decouple, real-time latent heating is replaced by the climatological monthly mean latent heating in the coupled experiment, such that the time-mean extratropical latent heating in the two runs is identical, while allowing for transient differences (Fig. 4.1 and 4.3 b, c). The non-linear relationship between latent heating and circulation causes significant differences in the extratropical mean jet and storm track characteristics between the two runs.

Coupling latent heating leads to an equatorward shift in the midlatitude baroclinicity, thus also shifting the eddy heat flux in the North Pacific and the Southern Hemisphere equatorward (Fig. 4.3 a, d). In the North Atlantic, however, eddy heat fluxes increase disproportionately to baroclinicity as a result of eddies transporting heat poleward more efficiently in the coupled- compared to the decoupled simulation (Fig. 4.3 g).

Cyclones grow more intense in the coupled run compared to the decoupled run (Fig. 4.4 a), consistent with how latent heating increases potential vorticity below the

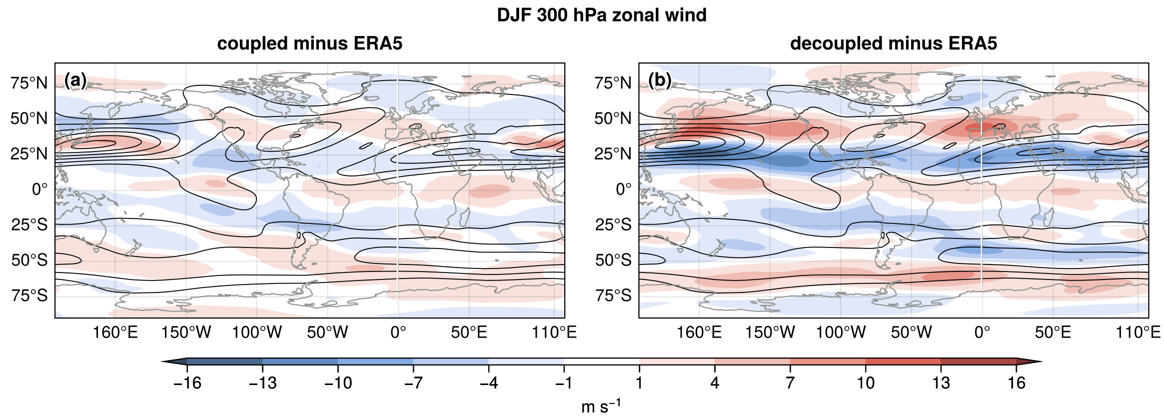

Figure 4.6: The coupled minus reanalysis (a) and decoupled minus reanalysis (b) difference in 300 hPa zonal wind, using the ERA5 reanalysis dataset (introduced in Chapter 3). Climatological zonal wind from reanalysis are shown in black in contours with intervals 10, 20, ..., 60 m s^{-1}. Values are averaged over December, January, and February.

heating maximum and enhances ascent within the cyclone (e.g. Wernli and Gray 2024). Where the subtropical jet is weak, cyclones also propagate more poleward in the coupled run (Fig. 4.4 f), contributing to the zonally asymmetric state (Fig. 4.5 c; Tamarin and Kaspi 2016; Schemm 2023). Coupling latent heating thus reduces model biases concerning storm track and jet tilts, compared to reanalysis (compare panels a and b in Fig. 4.6), which supports the idea that diabatic effects cause the too zonal and too equatorward storm tracks biases in climate models (Schemm 2023).

The subtropical jets strengthen in the coupled run compared to the decoupled run, a signal which is largely zonally symmetric (Fig. 4.5 a). To explain this, we suggest that since realistic latent heating occurs in poleward moving warm airmasses (Fig. 4.2 and Fig. 3.7) that often will return to lower latitudes, baroclinicity is maintained at lower latitudes in the coupled run, compared to the decoupled run, where latent heating also occurs in the cold and equatorward moving air, artificially forcing baroclinicity and therefore the jet at higher latitudes (Section 3.2).

As the hydrological cycle amplifies in a warming world, so will latent heating. There are large uncertainties as to how jets and storm tracks respond to increasing greenhouse gas concentrations and the physical drivers are hard to isolate due to the nonlinearities (Ossó et al. 2024). In the next chapter, I examine the latent heating feedback in a climate change experiment quantifying its contribution to storm track changes with warming.

Chapter 5

The latent heating feedback effect on storm tracks in current and future climates

This chapter is based on Auestad et al. (2026). As the climate warms, latent heating within storm tracks increases, but it remains unclear to what extent the latent heating feedback (Chapter 4) contributes to storm track changes with warming. Using atmospheric general-circulation model experiments that separate the coupled heating–dynamics feedback from climatological changes in latent heating, we show that this feedback plays a leading order role in intensifying storm tracks under +4 K warming. The feedback increases lower-tropospheric storm intensity, compensating for reduced baroclinicity, while its upper-tropospheric effect is seasonal: amplifying summer eddies but damping winter ones. The feedback is critical for storms that grow in moist environments, typical for summer and warmer climates, underscoring the need for accurate representation of moist processes in climate models.

5.1 Introduction

Atmospheric warming increases the atmospheric evaporative potential and thus the amount of water vapour in the atmospheric circulation. This is expected to lead to more intense precipitation and latent heat release, and thus potentially to stronger storms (Booth et al. 2013). The extent to which the latent heating induced intensification of storms scales with atmospheric temperature is, however, non-trivial, because latent heating also modifies the environmental conditions that govern storm growth (Held 1993; Papritz and Spengler 2015; Catto et al. 2019). This chapter presents novel simulations designed to examine the role of latent heating within storm tracks in a warmer climate.

The intensity and location of storm tracks are often diagnosed in an Eulerian framework by applying spatial or temporal filters to the horizontal winds to obtain the synoptic-scale eddy kinetic energy (Hall et al. 1994; Chang et al. 2002). Synoptic-scale eddy kinetic energy is converted from atmospheric eddy and mean available potential energy as warm, moist, and light air rises and cold, dense air sinks (Lorenz 1955). Condensation heats the ascending warm and moist air, increasing synoptic available potential energy (Danard 1966; Chapter 3) and enhancing ascent. Nevertheless, mean available potential energy, and consequently eddy kinetic energy, is projected to decrease with increasing atmospheric moisture content because climatological latent heating weakens the mean meridional temperature gradients and increases the mean static stability (Juckes 2000; O'Gorman and Schneider 2008; O'Gorman 2010; Raible et al. 2010; Lutsko et al. 2024).

As an alternative to Eulerian statistics, Lagrangian tracking of storms as individual features reveals that latent heating not only intensifies cyclones by strengthening lower-level potential vorticity within the cyclone, but also imposes a positive potential vorticity tendency poleward of the cyclone, thereby enhancing the poleward propagation of deep systems (Tamarin and Kaspi 2016; Yao et al. 2023). A key factor in how latent heating intensifies and steers cyclones is its precise location relative to the cyclone's potential vorticity structure. Consequently, accurately capturing the intensity and position of storm tracks in climate models likely depends sensitively on how well latent heating is represented (Willison et al. 2013; Willison et al. 2015; Hawcroft et al. 2017; Schemm 2023).

To examine the potential importance of how well structures of latent heating are represented in models, we focus on the coupling between latent heating and the circulation, as opposed to the climatological changes in latent heating. By artificially decoupling the latent heating in an atmospheric general circulation model while preserving its climatology, we specifically quantify how the nonlinear coupling between dynamics and latent heating feeds back on the flow itself, an effect we refer to as the *latent heating feedback* (Chapter 4).

Similar to Chapter 4, we decouple latent heating from the dynamics in order to quantify the latent heating feedback on eddy kinetic energy and cyclone intensity in both a present-day climate and under 4 K of warming. This reveals the relative contribution of the changes in the nonlinear relation between latent heating and dynamics to the full equilibrated storm track response. Furthermore, there is no a priori guarantee that eddy kinetic energy aggregated over large spatial domains primarily reflects the same dynamics as Lagrangian-tracked cyclones. To address this, we combine both Eulerian and Lagrangian metrics and attribute changes in eddy kinetic energy to changes in the intensity and location of tracked extratropical cyclones.

5.2 Methods

5.2.1 Model and data

The model and decoupling technique are the same as those used in Chapter 4. I repeat the most important aspects of the experimental design here; otherwise, see Chapter 4 for details. Here, as opposed to Chapter 4, the experiments are named in *italic* and capitalised.

The experimental design comprises four atmospheric general circulation model simulations using the Community Atmosphere Model 4.0 (CAM4; Table 5.1). The control experiment, representing the coupled latent heating climate (*Coupled*; with no perturbations applied to the physics schemes), includes topography and prescribed sea surface temperatures based on a 1995–2005 climatology (Hurrell et al. 2008). The grid spacing is 0.9° in the meridional direction and 1.25° in the zonal direction. We repeat the simulation adding 4 K uniformly to the sea surface temperature for the $Coupled + 4K$ simulation. The model is run on ARCHER2 (Beckett et al. 2024) for 50 years, with the first year discarded as spin-up.

To decouple latent heating from the dynamics, we repeat the two aforementioned experiments but replace the real time latent heating with the climatological monthly mean latent heating from the corresponding coupled experiment. When decoupling, the model latent heating is only removed and replaced above the boundary layer and in the extratropics to avoid a direct perturbation to the Hadley circulation. We define the extratropics to be where the 200 hPa eddy kinetic energy in the coupled run is on average larger than the hemisphere median eddy kinetic energy.

Each coupled–decoupled pair have by construction the same time mean free-troposphere extratropical latent heating and sea surface temperatures. The two-pairs form the four

Table 5.1: Overview of simulations and experimental design. The $\Delta(\cdot,\cdot)$ naming denotes a subtraction of the second argument from the first argument, i.e. $\Delta(x, y) = x - y$.

(a) Experiments

Name	**Latent heating**	**Sea surface temperature prescribed to**
Coupled	Normal	1995–2005 climatology
Decoupled	Prescribed climatological extra-tropical latent heating from *Coupled*	1995–2005 climatology
$Coupled + 4K$	Normal	1995–2005 climatology with 4 K added uniformly
$Decoupled + 4K$	Prescribed climatological extra-tropical latent heating from Coupled +4K	1995–2005 climatology with 4 K added uniformly

(b) Comparisons and interpretation

Name	**Purpose: quantify the ...**
$\Delta(Coupled + 4K, Coupled)$	effect of 4 K warming
$\Delta(Coupled, Decoupled)$	latent heating feedback effect in present-day climate
$\Delta(Coupled + 4K, Decoupled + 4K)$	latent heating feedback effect in a 4 K warmer climate
$\Delta(Coupled + 4K, Decoupled + 4K)$ $- \Delta(Coupled, Decoupled)$	change in the latent heating feedback effect under +4 K warming

experiments shown in Table 5.1.

The model output is stored as six-hour averages interpolated to 14 pressure levels using logarithmic interpolation. From this we compute eddy kinetic energy, $(1/2)(u'^2 + v'^2)$, where the primes denote 10-day high-pass filtered horizontal wind using a 243 point Lanczos filter (Duchon 1979). We perform a density weighted vertical integral of both eddy kinetic energy and specific humidity.

5.2.2 Cyclone tracking

As in Chapter 4, we identify cyclones from the six-hourly T42-truncated 850 hPa vorticity field using the TRACK algorithm (Hodges 1994; Hodges 1995; Hodges 1999), only keeping the cyclones that travel further than 1000 km, and persist for more than 2 days. Additionally, we now only consider cyclones that spend at least half their lifetime poleward of 30° north or south and we require the complete cyclone lifetime to be within either December-February or June-August. We track cyclones on 48 complete winter and summer seasons as we discard the first modelled year.

Cyclone intensity is defined as the vorticity at the 'feature point' identified on the T42 850 hPa vorticity field (Hodges 1994). We also compute cyclone growth rates as the change in cyclone relative vorticity over each six-hour time step $(\Delta\zeta_{850}/\Delta t)$, using centred finite differences except at genesis and lysis, where we apply a one-sided finite-difference scheme.

5.2.3 Cyclone mean quantities

We compute the cyclone average eddy kinetic energy, specific humidity and baroclinicity by a spatially weighted average over grid points that fall within 1.5 times the Rossby radius of the cyclone centre at 850 hPa. We approximate the Rossby radius by

$$R_d = 1000 \text{ km} \, \frac{sin(45°)}{|sin(\lambda_{cyclone})|}, \tag{5.1}$$

where $\lambda_{cyclone}$ is the latitude of the cyclone and the vertical lines indicate taking the absolute value. The denominator is proportional to $|f|$, the coriolis parameter, and accounts for the fact that R_d decreases towards the poles (Eq. 2.13). Thus, the radius used to calculate cyclone averaged quantities is $1.5 \times R_d$. The results are not sensitive to the exact choice of this radius.

Baroclincity is computed in a two-step process, by taking the cyclone averaged euclidean norm of the horizontal potential temperature gradient at 600 hPa divided by the cyclone averaged vertical temperature gradient between 500 hPa and 700 hPa,

$$B = \frac{||\boldsymbol{\nabla}_p \theta_{600 \text{ hPa}}||}{(\theta_{500 \text{ hPa}} - \theta_{700 \text{ hPa}})/200 \text{ hPa}}, \tag{5.2}$$

where $\boldsymbol{\nabla}_p$ is the horizontal gradient evaluated at constant pressure.

5.2.4 Cyclone counts, densities, and kernel averaged quantities

To create climatologies of cyclone associated eddy kinetic energy in longitude-latitude space, we first average the cyclone-averaged vertically integrated eddy kinetic energy over all cyclones that fall within 5° spherical caps, with centres placed on a $1° \times 1°$ longitude–latitude grid. For simplicity, all samples within each spherical cap are equally weighted. We similarly count the number of cyclones within the same spherical caps and scale this count to represent the average number of features observed per day, before multiplying the two quantities.

Because the data have six-hourly temporal resolution, the same cyclone can be counted up to four times per day. The scaling is arbitrary and is chosen here such that the magnitudes are comparable to those in the eddy kinetic energy climatology. Furthermore, the result is insensitive to whether we simply count cyclones or instead estimate the probability density function of the features, for example the feature *density* (not shown; Hodges 1996). The spherical caps overlap, which smooths the field.

We compute the cyclone density in baroclinicity–moisture space as the number of cyclones within an ellipse whose semi-axes correspond to half a standard deviation in each variable, divided by the area of the ellipse and by the total number of cyclones summed over all ellipses. We then average the cyclone growth rate and intensity over the cyclones found within the same ellipses in baroclinicity–moisture space, weighting each value by $1-r/r_{max}$, where r is the standardised distance to the centre of the ellipse and r_{max} is the maximum such distance found within that ellipse. The ellipse sizes are shown in Fig. 5.8 for reference. Also here the ellipses overlap and therefore smooth the fields.

5.2.5 Cyclone centred composites of potential vorticity

We calculate Ertel potential vorticity,

$$q = -g(f\mathbf{k} + \nabla \times \mathbf{u}_3) \cdot \nabla\theta, \tag{5.3}$$

where g is the gravitational acceleration on earth, f is the Coriolis parameter, $\mathbf{k}$ is the vertical unit vector, ∇ is the three dimensional gradient operator with pressure as vertical coordinate, and $\mathbf{u}_3$ is the three dimensional wind field. Potential vorticity is then conservatively interpolated to a 40 km $\times$ 40 km Cartesian grid centred on each cyclone before we average over the composites.

5.3 Results

5.3.1 Eddy kinetic energy response to the latent heating feedback

The +4 K global warming response in eddy kinetic energy is computed by taking the difference between a simulation with prescribed climatological sea surface temperatures from 1995–2005 (Hurrell et al. 2008) and an identical simulation with 4 K uniformly added to the sea surface temperatures. We refer to this difference as $\Delta(Coupled + 4K, Coupled)$ (Table 5.1). We reiterate that *Coupled* refers to the fact that latent heating is coupled to the dynamics (i.e. without modifications to the physics schemes), in contrast to the *Decoupled* runs.

The wintertime eddy kinetic energy response to +4 K is largely consistent with the Coupled Model Intercomparison Project Phase 6 (CMIP6) trends. In the global warming experiment, $\Delta(Coupled + 4K, Coupled)$, vertically integrated eddy kinetic energy generally strengthens in the winter hemispheres (Fig. 5.1 a, d). The Southern Hemisphere and North Pacific winter responses are consistent with the CMIP6 trends and potentially also emerging reanalysis trends, whereas the North Atlantic winter increase in eddy kinetic energy is shifted too far poleward in our experiments compared with reanalysis and the CMIP6 (Harvey et al. 2020a; Chemke et al. 2022; Battalio and Lora 2024).

The summertime eddy kinetic energy trends are largely consistent with the CMIP6 projections. In the respective summers, eddy kinetic energy shifts poleward in the Southern Hemisphere, equatorward in the North Pacific and strengthens in the North Atlantic in the global warming experiment (Fig. 5.1 a, d). This is consistent with the zonal mean poleward shift in austral summer eddy kinetic energy in the CMIP6 mean

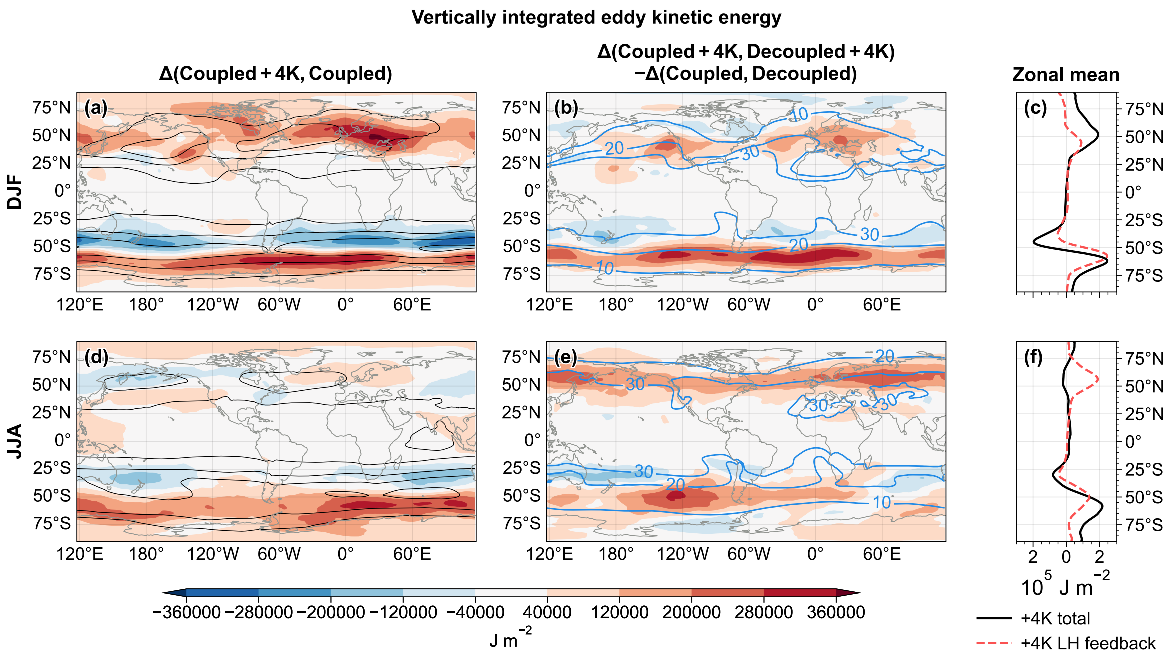

Figure 5.1: The response in vertically integrated eddy kinetic energy to adding 4 K to the sea surface temperatures (shading; a, d) and the contribution from the latent heating feedback (shading; b, e) averaged over December, January, February (a, b) and over June, July, and August (c, d). Vertically integrated eddy kinetic energy in *Coupled* is shown by black contours in a and d for levels: 25, 75, 125, 175, 225, 275 10^5 J m^{-2}. Vertically integrated specific humidity in *Coupled* + 4*K* is shown in blue contours (b, d), with units of kg m^{-2}. Zonally averaged vertically integrated eddy kinetic energy is shown in panels c and f.

under warming (Karbi and Chemke 2025). The regional and zonally asymmetric increase in eddy kinetic energy during boreal summer in the global warming experiment is inconsistent with possible reanalysis trends: boreal summer eddy kinetic energy appears to have generally weakened over the past 40 years (Battalio and Lora 2024). Yet, in the zonal mean, the global warming experiment also exhibits a net decrease in boreal summer eddy kinetic energy (Fig. 5.1 d), consistent with reanalysis and the CMIP6 trends (Chemke and Coumou 2024).

To quantify the contribution from the latent heating feedback to the eddy kinetic energy changes in the global warming experiment, we decouple latent heating from the dynamics. Specifically, we repeat both the *Coupled* and $Coupled + 4K$ simulations, except that we replace the real-time latent heating in the extratropical free troposphere with the climatological latent heating from the respective *Coupled* run. This yields two runs with latent heating decoupled from the dynamics: one with a present-day climate, *Decoupled*, and one with a 4 K warmer climate, *Decoupled+4K*.

The latent heating feedback effect is quantified as the effect of latent heating distinct from the climatological forcing. By construction, the coupled and decoupled paired runs have identical time mean latent heating in the extratropical free troposphere (the region of decoupling). Prescribing latent heating in the decoupled runs removes the temporal variance in latent heating and thus eliminates the covariance between the dynamics and latent heating (Chapter 4). Consequentially, only the coupled experiments allow for nonlinear interactions, or a feedback, between latent heating and the synoptic dynamics.

Taking the difference between the *Coupled* and *Decoupled* experiments, we quantify the effect of the latent heating feedback in the present-day climate and in the +4 K climate, which we denote by $\Delta(Coupled, Decoupled)$ and $\Delta(Coupled{+}4K, Decoupled{+}4K)$, respectively (Table 5.1). The difference $\Delta(Coupled + 4K, Decoupled + 4K) - \Delta(Coupled, Decoupled)$ then gives the change in climate specifically due to the change in the latent heating feedback in the global warming experiment.

The results show the changing latent heating feedback to play a leading order role in the global storm track changes. In austral summer, the latent heating feedback accounts for approximately all of the increase, but not the subtropical decrease in Southern Hemisphere eddy kinetic energy in the global warming experiment (Fig. 5.1 a–c). In winter in both hemispheres, the latent heating feedback explains roughly half of the increase in eddy kinetic energy (Fig. 5.1 a–f).

The Northern Hemisphere during boreal summer stands out: there, the latent heating feedback increases eddy kinetic energy, yet the total eddy kinetic energy response to global warming is a net zonal mean weakening (Fig. 5.1 d–f). This implies that in the decoupled runs, there is a compensating decrease in eddy kinetic energy in the Northern Hemisphere in boreal summer under +4 K forcing ($\Delta(Decoupled{+}4K, Decoupled)$; not shown). This could be linked to baroclinicity reducing with warming, which is discussed later on.

The latent heating feedback effect is strongest where moisture is available in the extratropics. The eddy kinetic energy response to the latent heating feedback under global warming is somewhat equatorward-shifted compared with the total response (Fig. 5.1), particularly in the winter hemispheres. The latent heating feedback response is generally strongest where vertically integrated specific humidity is larger than 10 kg m^{-2} (blue lines in Fig. 5.1 b, e). It is physically consistent that the feedback effect is focused on regions where more moisture is available, which are located further poleward and are more zonally symmetric in summer than in winter. While moisture availability likely explains the seasonal differences in the location of the feedback response, the difference in amplitude arises from the upper-tropospheric response, which we show next.

5.3.2 The vertical structure of the eddy kinetic energy response

In the global warming experiment, zonal mean eddy kinetic energy shifts upward and poleward in both summer and winter in the Southern Hemisphere (Fig. 5.2 a, c). In the Northern Hemisphere, the zonal mean eddy kinetic energy also shifts upward in both seasons, yet, eddy kinetic energy shifts poleward in response to +4 K forcing only in boreal winter (Fig. 5.2 a, c).

The change in the latent heating feedback under +4 K forcing produces a larger increase in upper-tropospheric eddy kinetic energy in the summer hemispheres than in the winter hemispheres (Fig. 5.2 b, d). Consequently, the differing upper-tropospheric response explains why the *vertically integrated* eddy kinetic energy response to the latent heating feedback under +4 K forcing accounts for only about half of the wintertime increase, but nearly all of the summertime increase, in the total eddy kinetic energy response to +4 K forcing (Fig. 5.1 c, f).

To understand the changes in zonal mean eddy kinetic energy, we examine the changes in zonal mean potential temperature which to first order drive atmospheric density variations (Fig. 5.3). Classical eddy–mean flow theory of baroclinic instability links long-term changes in eddy kinetic energy to changes in vertical and meridional density gradients, although transient eddies also feed back on the mean state (Lorenz 1967; Lindzen and Farrell 1980; Hall et al. 1994). As the climate warms, the upper-tropospheric tropical air and lower-tropospheric polar air warm most strongly, as the tropical water cycle amplifies and polar feedbacks emerge. This produces stronger density gradients in the upper troposphere and weaker gradients in the lower troposphere; the former strengthens and shifts eddy kinetic energy poleward, whereas the latter weakens it (Shaw et al. 2016).

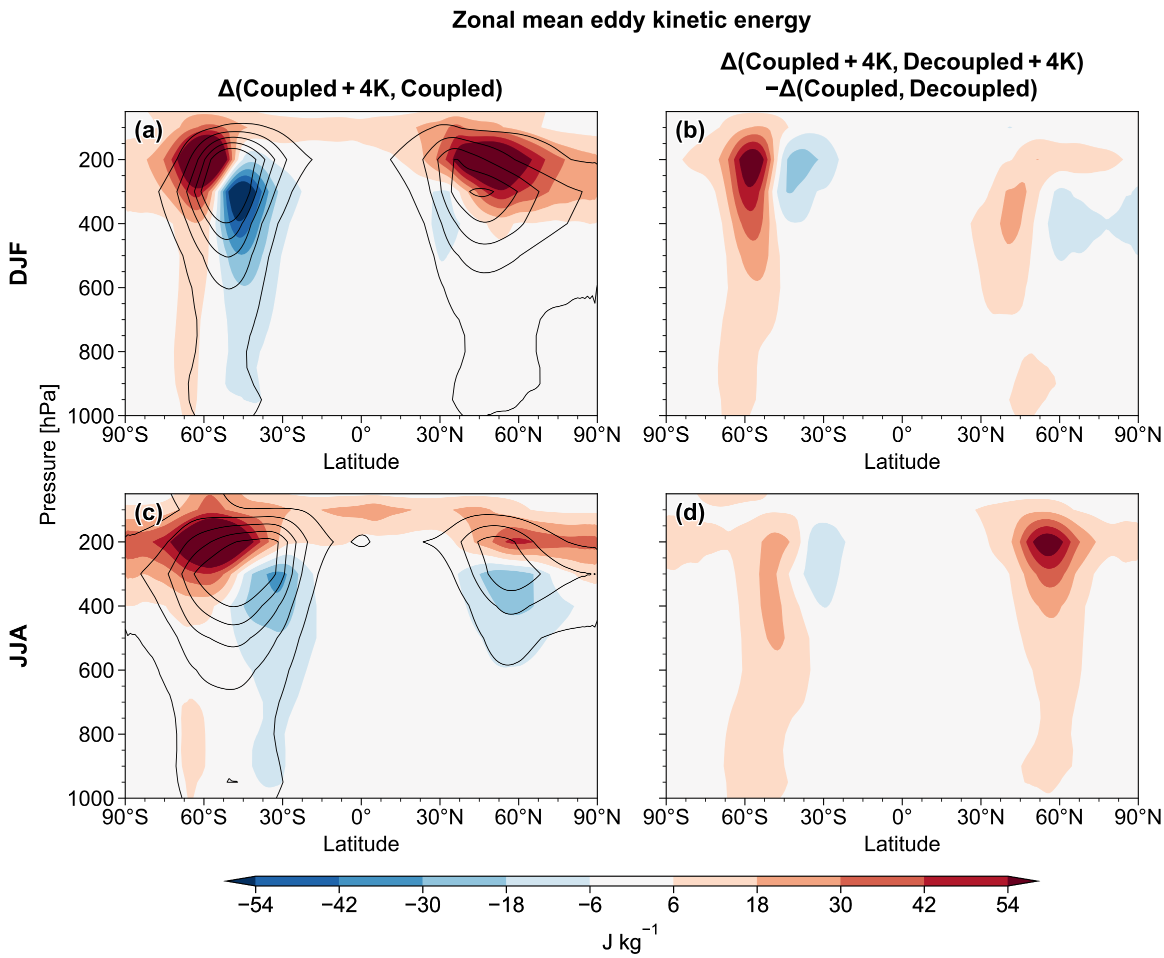

Figure 5.2: The shading shows the response in zonal mean eddy kinetic energy to adding 4 K to the sea surface temperatures (a, c) and to the latent heating feedback when adding 4 K to the sea surface temperatures (b, d) averaged over December, January, February (a, b) and over June, July, and August (c, d). The contours show the zonal mean eddy kinetic energy in the *Coupled* run (a, c) for levels: 50, 100, 150, 200, 250 J kg^{-1}.

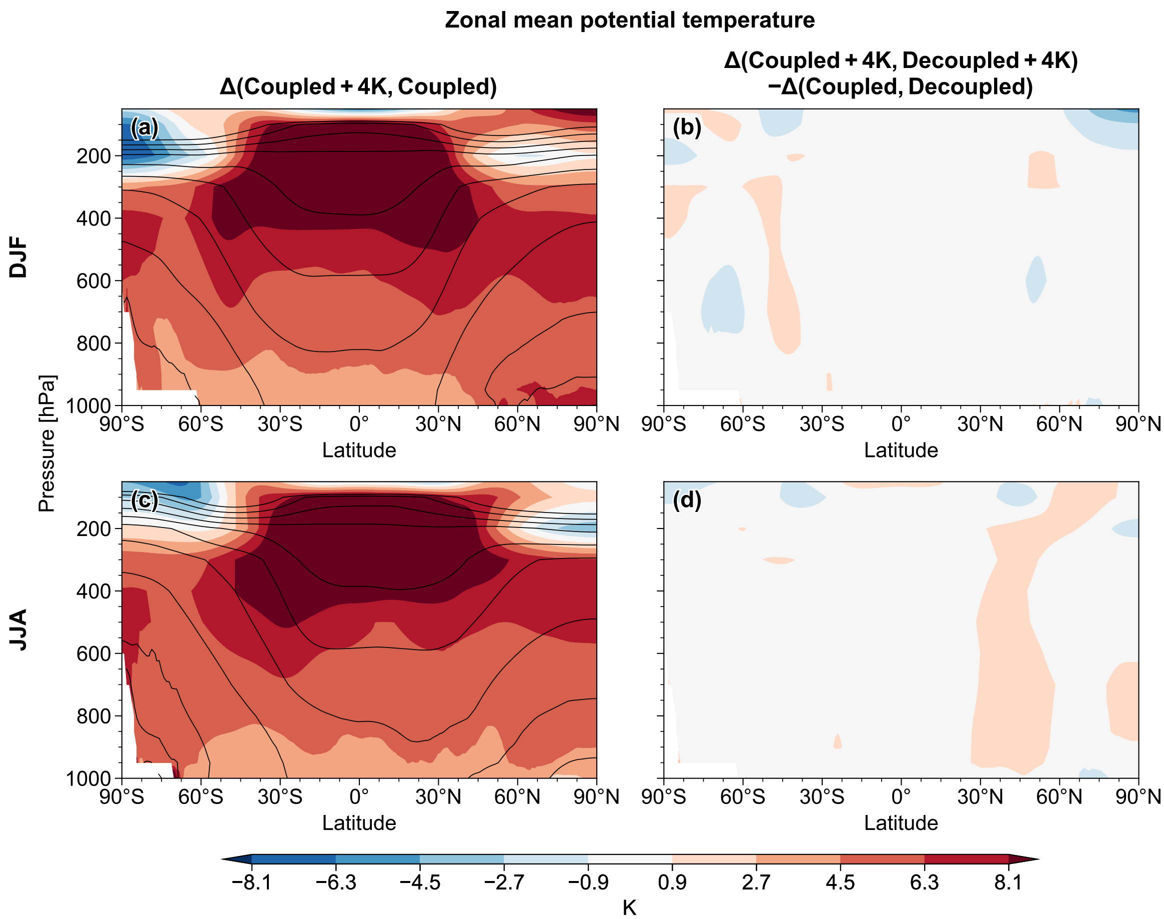

Figure 5.3: The shading shows the response in zonal mean potential temperature to adding 4 K to the sea surface temperatures (a, c) and to the latent heating feedback when adding 4 K to the sea surface temperatures (b, d) averaged over December, January, February (a, b) and over June, July, and August (c, d). The contours show the zonal mean potential temperature in the *Coupled* run (a, c) for levels: 230, 245, 260, 275, 290, 305, 320, 335, 350, 365, 380, 395 K. Subsurface grid points are masked.

The upper-tropospheric potential temperature gradients strengthen in the global warming experiment (Fig. 5.3 a, c), which is consistent with the general upward and poleward shift in Southern Hemisphere zonal mean eddy kinetic energy (Fig. 5.2 a, c). In contrast, the large seasonal difference in the Northern Hemisphere eddy kinetic energy response cannot be easily reconciled with the zonal mean potential temperature response, which vary little between the seasons (Fig. 5.3 a, c).

Polar amplification should be weak in these experiments because we hold sea ice fixed in the global warming set-up. Potential temperatures do increase over the poles, although not as strongly as in the tropical upper troposphere (Fig. 5.3 a, c). Additionally, static stability increases below 400 hPa, which should mitigate eddy kinetic energy as it reduces the reservoir of available potential energy.

The eddy kinetic energy response in $\Delta(Coupled{+}4K, Decoupled{+}4K){-}\Delta(Coupled, Decoupled)$ is unlikely to be driven by changes in mean-state temperature gradients, given the mismatch in amplitude between the eddy kinetic energy and temperature gradient responses. While the latent heating feedback plays a leading order role for the eddy kinetic energy changes under 4 K warming (Fig. 5.2), the zonal mean potential temperature response in $\Delta(Coupled + 4K, Decoupled + 4K) - \Delta(Coupled, Decoupled)$ is much smaller than in $\Delta(Coupled + 4K, Coupled)$ (Fig. 5.3). This confirms that the experimental design isolates changes in the direct effect of latent heating on the eddies from changes in the effect of latent heating on the mean state.

Examining the response to the latent heating feedback for fixed climates reveals that the feedback weakens upper-tropospheric eddy kinetic energy in winter while it increases it in summer. Figure 5.4 shows the vertical zonal mean eddy kinetic energy response to coupling in present-day and +4 K climates, individually. In the lower troposphere, the latent heating feedback strengthens eddy kinetic energy irrespective of season and hemisphere (Fig. 5.4), and this effect continues to increase with warming (Fig. 5.2). In

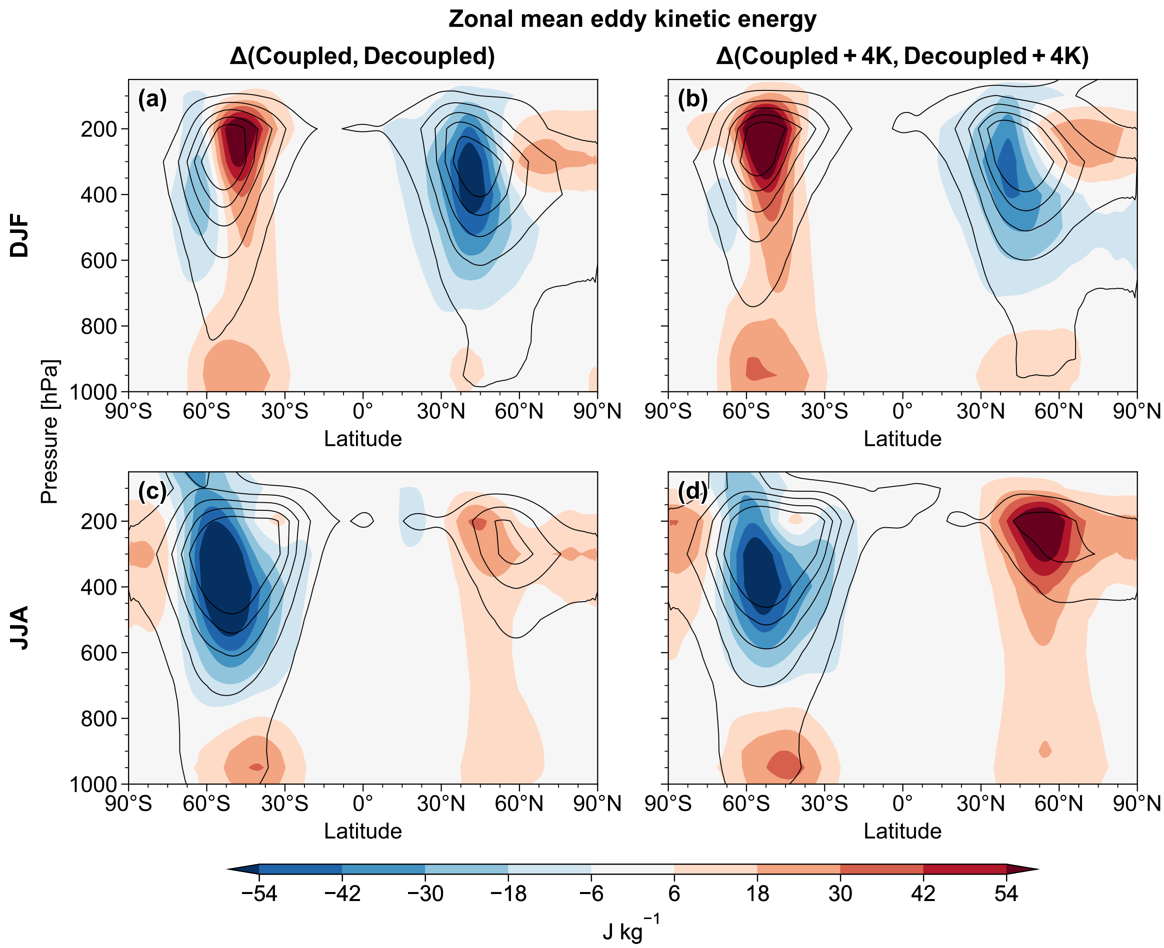

Figure 5.4: The shading shows the response in zonal mean eddy kinetic energy to the latent heating feedback in the present-day climate (a, c) and the +4 K climate (b, d) averaged over December, January, February (a, b) and over June, July, and August (c, d). The contours show the zonal mean eddy kinetic energy in the *Decoupled* (a, c) and $Decoupled + 4K$ runs (b, d) for levels: 50, 100, 150, 200, 250 J kg^{-1}.

the upper troposphere, in contrast, the latent heating feedback strengthens eddy kinetic energy only in summer, while it weakens eddy kinetic energy in winter.

Although the latent heating feedback unambiguously strengthens lower-tropospheric eddy kinetic energy in all seasons, its effect on the upper troposphere — and therefore on vertically integrated eddy kinetic energy — is strongly seasonally dependent. In the respective winter months, the latent heating feedback weakens upper-tropospheric eddy kinetic energy less in the 4 K warmer climate than in the present-day climate (Fig. 5.4), which results in a moderate net increase in upper-tropospheric eddy kinetic energy (Fig. 5.2). In the respective summer months, the latent heating feedback strengthens upper-tropospheric eddy kinetic energy in present-day climate and even more with +4 K forcing (Fig. 5.4), leading to a net increase (Fig. 5.2).

For the rest for the chapter, we mainly focus on the Southern Hemisphere as the zonal mean eddy kinetic energy (Fig. 5.4) and tracked storm responses to the latent heating feedback are very similar in both hemispheres (not shown). The Southern Hemisphere results can therefore be transferred to the Northern Hemisphere. In the next sections, we relate the eddy kinetic energy response to changes in tracked storms and more closely examine the effect of the latent heating feedback on storm structure and growth mechanisms.

5.3.3 The latent heating feedback effect on cyclones

The eddy kinetic energy response reflects changes in cyclone frequency and intensity (Fig. 5.5). To demonstrate this, we average the vertically integrated eddy kinetic energy within 1.5 times the Rossby radius of each tracked cyclone, and multiply the resulting cyclone-averaged eddy kinetic energy by the daily number of observed cyclones the same longitude and latitude. We avoid comparing grid points where there are on average

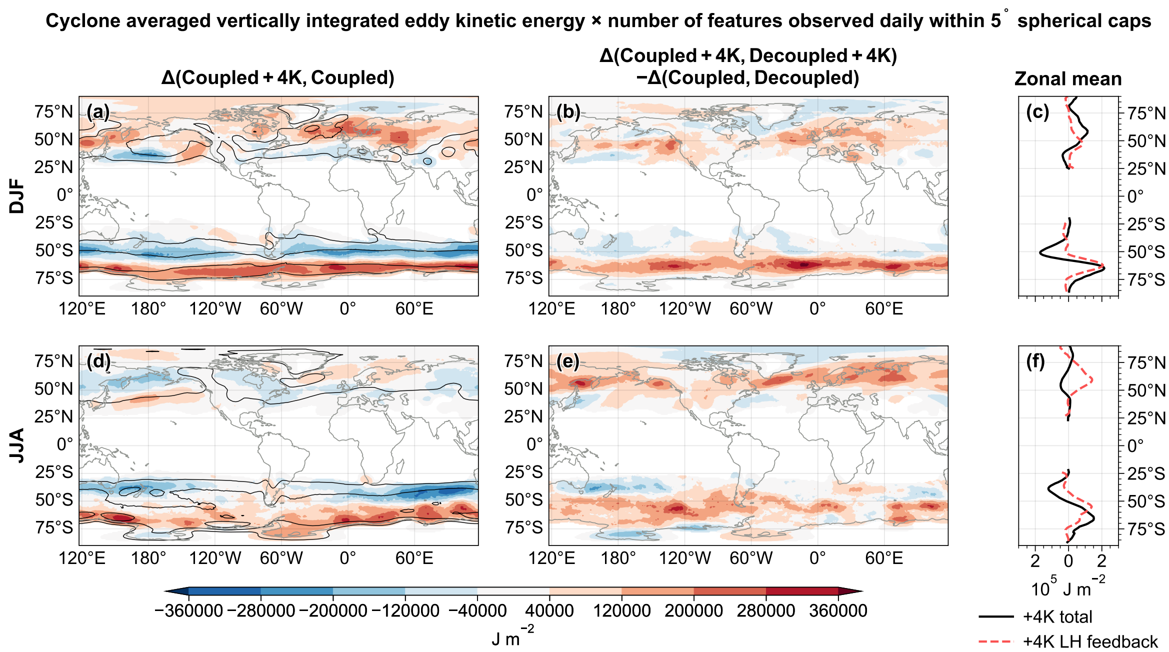

Figure 5.5: The response in cyclone-averaged vertically integrated eddy kinetic energy to adding 4 K to the sea surface temperatures (shading; a, d) and the contribution from the latent heating feedback (shading; b, e) averaged over December, January, February (a, b) and over June, July, and August (c, d). All panels show cyclone-averaged vertically integrated eddy kinetic energy averaged over 5° spherical caps and multiplied by the average number of features observed daily within the same 5° spherical caps. Black contours (a, c) show the *Decoupled* climatology for the same levels as in Fig. 5.1. The corresponding zonally averaged (cyclone-averaged vertically integrated) eddy kinetic energy is shown in panels c and f.

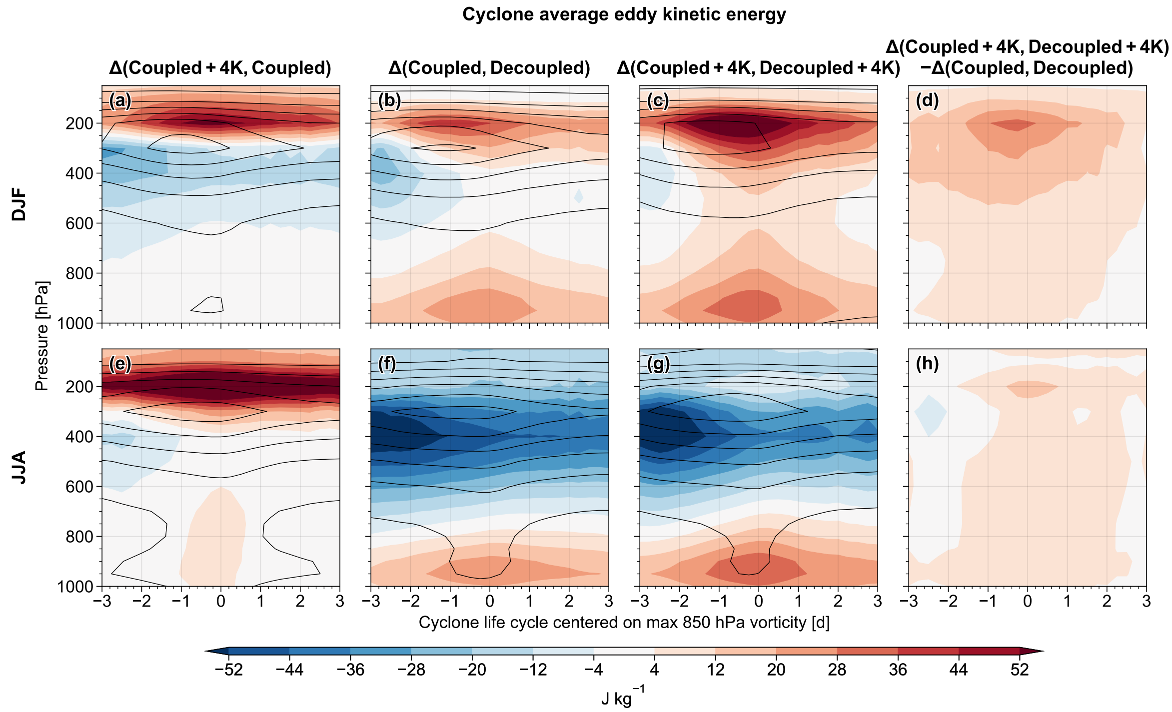

Figure 5.6: The shading shows the response to coupling and +4 K forcing in cyclone-averaged eddy kinetic energy composited over cyclones in the Southern Hemisphere for December, January, February (a–d) and over June, July, and August (e–h). The horizontal axes show cyclone lifetime, centred at the time of peak 850 hPa vorticity of the tracked cyclones. Shown are the responses to 4 K warming (a, e), to coupling latent heating in present-day climate (b, f), to coupling latent heating in the 4 K warmer climate (c, g), and to the change in the latent heating feedback effect under 4 K warming (d, h). The black contours show the cyclone averaged eddy kinetic energy in the *Coupled* (a, e), *Decoupled* (b, f), and $Decoupled + 4K$ (c, g) runs for levels: 50, 100, 150, 200, 250, 300, 350, 400, 450, 500 J kg^{-1}.

less than three cyclones in each month in either simulation. The resulting cyclone-conditional eddy kinetic energy response is qualitatively similar to the full eddy kinetic energy response (compare Figs. 5.1 and 5.5). Neither the spatial cyclone distribution nor the mean cyclone eddy kinetic energy alone explains the changes in eddy kinetic energy (not shown); we therefore infer that the eddy kinetic energy response arises from both spatial storm track shifts and changes in cyclone intensities.

Figure 5.6 shows the vertical structure of cyclone-averaged eddy kinetic energy composited over cyclones in the Southern Hemisphere. The composites span the three days before and after the time of peak cyclone vorticity at 850 hPa. In the lower troposphere, eddy kinetic energy in the *Coupled* (a, e), *Decoupled* (b, f) and $Decoupled + 4K$ (c, g) runs peaks together with the 850 hPa vorticity, whereas in the upper troposphere eddy kinetic energy peaks slightly earlier (black contours in Fig. 5.6).

The cyclone-averaged eddy kinetic energy reveals a vertical structure similar to the Eulerian eddy kinetic energy in response to +4 K forcing and coupling (Fig. 5.2). Due to +4 K forcing in the coupled runs, the cyclone-averaged eddy kinetic energy shifts upwards in both seasons and increases weakly in the lower troposphere in austral winter (Fig. 5.6 a, e). The change in the latent heating feedback under +4 K forcing weakly increases eddy kinetic energy throughout the depth of the troposphere in both seasons, but enhances upper-tropospheric eddy kinetic energy more strongly in austral summer than in austral winter (Fig. 5.6 d, h).

As in the Eulerian response, the latent heating feedback increases lower-tropospheric cyclone-averaged eddy kinetic energy in both seasons in the present-day climate (Fig. 5.6 b, f), and even more so in the +4 K climate (Fig. 5.6 c, g), leading to a net increase in lower-tropospheric eddy kinetic energy due to the change in the latent heating feedback (Fig. 5.6 d, h). The increase in upper-tropospheric cyclone-averaged eddy kinetic energy due to changes in the latent heating feedback arises from a strengthening of eddy kinetic energy in austral summer (Fig. 5.6 b, c) and a reduced weakening in austral winter (Fig. 5.6 f, g), again similar to the Eulerian response (Fig. 5.4).

The increase in lower-tropospheric eddy kinetic energy due to the latent heating feedback likely results from latent heating enhancing ascent within cyclones, thereby stretching and spinning up the cyclonic vortex (e.g. Wernli and Gray 2024). As latent heating within storms increases with atmospheric temperature, it is reasonable that this effect strengthens with warming, as seen in our experiments in both seasons.

The seasonally dependent effect of the latent heating feedback on upper-tropospheric eddy kinetic energy is less intuitive. The seasonal difference may stem from the latent heating feedback generating eddy kinetic energy at higher altitudes in summer than in winter, because convection within cyclones penetrates to higher levels in a warm atmosphere than in a cold atmosphere (Tierney et al. 2018).

Enhanced summertime convection may offset a general weakening of upper-tropospheric eddy kinetic energy by the latent heating feedback. The weakening of upper-tropospheric eddy kinetic energy due to the latent heating feedback is strongest before peak cyclone intensity, an effect which is strongest in austral winter, but can also be seen near 400 hPa in austral summer (Fig. 5.6 b, c, f, g). Thus, the effect seems linked to changes in the typical cyclone life cycle, which we examine next.

As a final remark, the results in panel h of Fig. 5.6 are sensitive to the subset of cyclones considered. In Fig. 5.6, we composite over all cyclones that spend at least half their lifetime poleward of 30°. Instead, compositing the 10 strongest cyclones each winter shows that the upper-tropospheric austral winter weakening intensifies, leading to a net decrease in upper-tropospheric cyclone-averaged eddy kinetic energy due to the latent heating feedback under +4 K forcing (not shown). This sensitivity further motivates identifying the physical mechanism responsible for the weakening.

5.3.4 The latent heating feedback effect on troughs and ridges around cyclones

To better understand the effect of the latent heating feedback on upper-tropospheric eddy kinetic energy in the vicinity of cyclones, we focus on the present-day simulations and examine cyclone centred composites of 300 hPa potential vorticity anomalies relative to the zonal mean (Fig. 5.7). We exclude cyclones poleward of 70° N to avoid in-

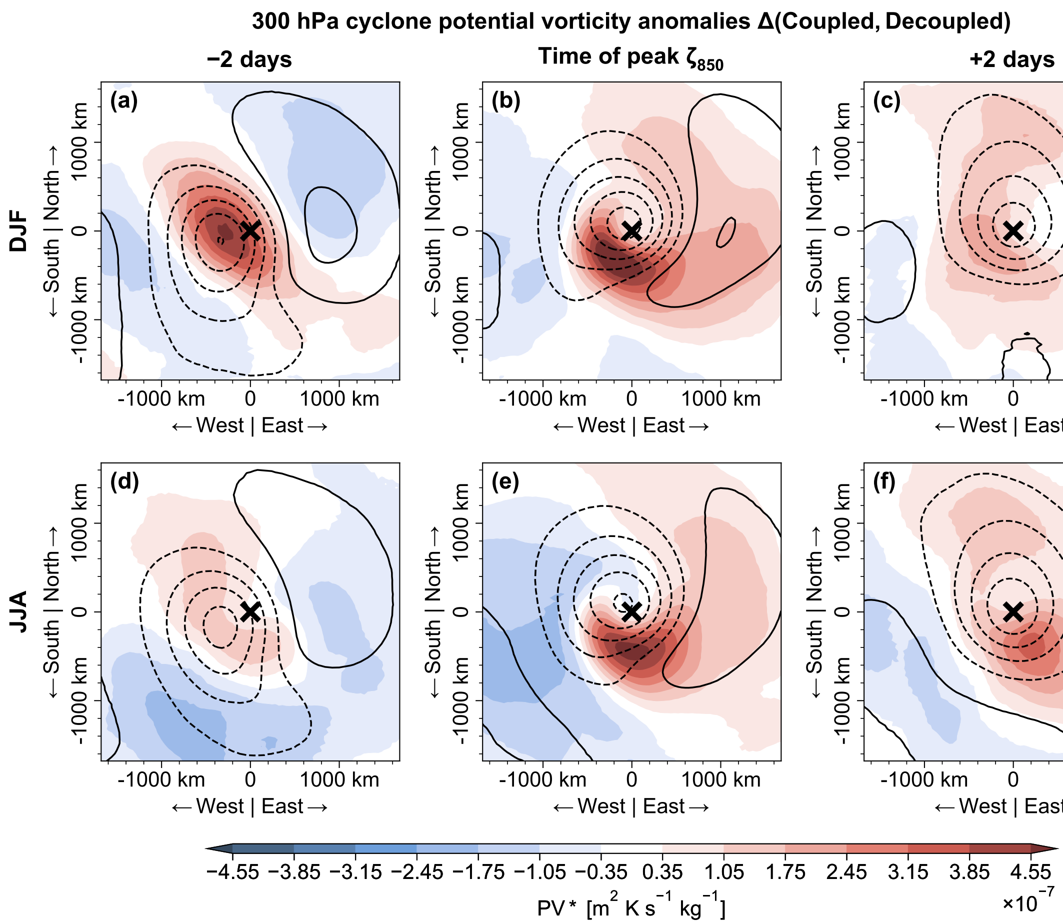

Figure 5.7: Cyclone centred composites of potential vorticity anomalies from the zonal mean at 300 hPa for cyclones in the Southern Hemisphere for December, January, February (a–c) and over June, July, and August (d–f). The shading shows the difference in anomalous potential vorticity between the *Coupled* and *Decoupled* runs 2 days before peak cyclone vorticity (a, d), at the time of peak cyclone vorticity (b, e), and 2 days after peak cyclone vorticity (c, f). The black contours show the mean potential vorticity anomalies on cyclones in the *Decoupled* run at levels: -1.8, -1.4, -1., -0.6, -0.2, 0.2, 0.6, 1., 1.4, 1.8 10^{-6} m^2 K s^{-1} kg^{-1}. Differing from the set of cyclones used for Fig. 5.6, we here leave out cyclones poleward of 70° S, for which the ice cap causes spurious values of potential vorticity. The 850 hPa cyclone centre is marked with a black cross.

teractions with the ice cap; otherwise, the cyclone composite includes the same cyclones as analysed previously. The black contours show the potential vorticity anomalies associated with Southern Hemisphere cyclones in each season in the *Decoupled* run. The black cross marks the 850 hPa cyclone centre. Two days before peak intensity, the composites exhibit a Rossby wave that tilts westward with height relative to the centre of the lower-level cyclone (Fig. 5.7 a, d). At peak intensity, the potential vorticity anomaly centres rotate cyclonically around each other (Fig. 5.7 b, e), suggesting cyclonic Rossby wave breaking associated with high-impact cut-off low systems (Barnes et al. 2025). Two days after peak intensity, a single trough remains approximately vertically aligned with the lower-level cyclone centre (Fig. 5.7 c, f).

In the *Coupled* run, cyclones are associated with weaker upper-tropospheric waves prior to peak intensity than in the Decoupled run (shading in Fig. 5.7 a, d). Latent heating is important for baroclinic waves to develop bottom up (Boettcher and Wernli 2013); thus, the *Coupled* cyclone composite likely contains waves that, on average, depend less on an upper-tropospheric disturbance than the *Decoupled* composite. This interpretation is consistent with coupling reducing upper-tropospheric eddy kinetic energy before peak cyclone intensity (Fig. 5.6 b, c, f, g).

At peak intensity, the ridge east of the cyclone is amplified and the trough 'flattened' in the *Coupled* run compared to the *Decoupled* run (Fig. 5.7 b, e). The amplified ridge intrudes into the trough centred on the cyclone, damping the negative potential vorticity anomaly above the cyclone core, while the remainder of the trough deepens to the west. This flattening is consistent with moist baroclinic instability producing a narrow, intense region of ascent and broader regions of descent, in contrast to dry baroclinic instability, where vertical velocities are more symmetric (Emanuel et al. 1987; O'Gorman 2011).

The *Coupled* cyclones, compared with the *Decoupled* cyclones, are characterised by weaker upper-tropospheric potential vorticity anomalies two days after peak intensity (Fig. 5.7 c, f). Thus, the potential vorticity field in the *Coupled* run is closer to the zonal mean and exhibits less waviness at this stage than in the *Decoupled* run. This pattern may reflect enhanced wave dissipation after cyclones reach peak intensity, as latent heating enhances upper-level divergent outflows, which amplify ridges and weaken troughs (Teubler and Riemer 2021). Alternatively, it is possible that the *Coupled* composite exhibits weaker potential vorticity anomalies because *Coupled* cyclones vary more in structure than *Decoupled* cyclones: *Coupled* cyclones can have either moist or dry structures, whereas *Decoupled* cyclones are effectively all dry. The reduced waviness is consistent with the reduction of upper-tropospheric eddy kinetic energy after peak intensity, an effect we observe in winter (Fig. 5.6 f, g).

To summarise, across the full depth of the troposphere coupling latent heating to the dynamics increases eddy kinetic energy more effectively in the warm season than in the cold season (Figs. 5.4 and 5.6), consistent with the larger influence of latent heating on vertical velocities in summer than in winter (Kohl and O'Gorman 2024). The seasonal difference arises because coupling reduces upper-tropospheric eddy kinetic energy, particularly in the cold season. Our potential vorticity analysis (Fig. 5.7) suggests two contributing mechanisms for this reduction: (1) when latent heating is coupled, less upper-level wave activity is required to form cyclones; and (2) coupling enhances upper-level wave dissipation, leaving the upper troposphere more zonal and less wavy towards the end of the cyclone life cycle. In the warm season, direct eddy amplification may offset these effects and produce a net increase in upper-tropospheric eddy kinetic energy, especially near peak cyclone intensity.

5.3.5 Lower-tropospheric cyclone intensification in moist and baroclinic environments

Lower-tropospheric storm intensity has the greatest societal impact. We have shown that the latent heating feedback strengthens lower-tropospheric eddy kinetic energy and cyclone intensities in both the warm and cold seasons, and in both hemispheres, and that this effect becomes stronger as the atmosphere warms. However, baroclinicity, which represents the reservoir of potential energy from which extratropical cyclones grow, may also change with global warming (O'Gorman 2010). In this section, we show that the latent heating feedback can compensate for weaker baroclinicity and that it is crucial for the development of the strongest lower-tropospheric storms in both the present-day and +4 K climates.

From multivariate idealised baroclinic life cycle experiments, we know that both the availability of moisture and baroclinicity enhance cyclone intensity up to certain thresholds (Booth et al. 2013; Tierney et al. 2018). In our present-day climate simulations, cyclones exist in environments ranging from dry to moist and, simultaneously, from nearly barotropic to baroclinic. However, no cyclones exist in environments that are both very moist and strongly baroclinic at the same time (black contours in Fig. 5.8). We continue to analyse Southern Hemisphere cyclones, but the results are similar also for the Northern Hemisphere (not shown).

The latent heating feedback enhances cyclone intensification (Chapter 4). Cyclones intensify in environments of high baroclinicity and decay where baroclinicity is weaker, or where conditions are very dry, in both the *Coupled* and *Decoupled* simulations (shading in Fig. 5.8). In the *Coupled* run, cyclones also intensify in moist environments with weak baroclinicity (Fig. 5.8 a, c). Intensification rates are generally higher in the *Coupled* run compared to the *Decoupled* run, with the largest differences in austral

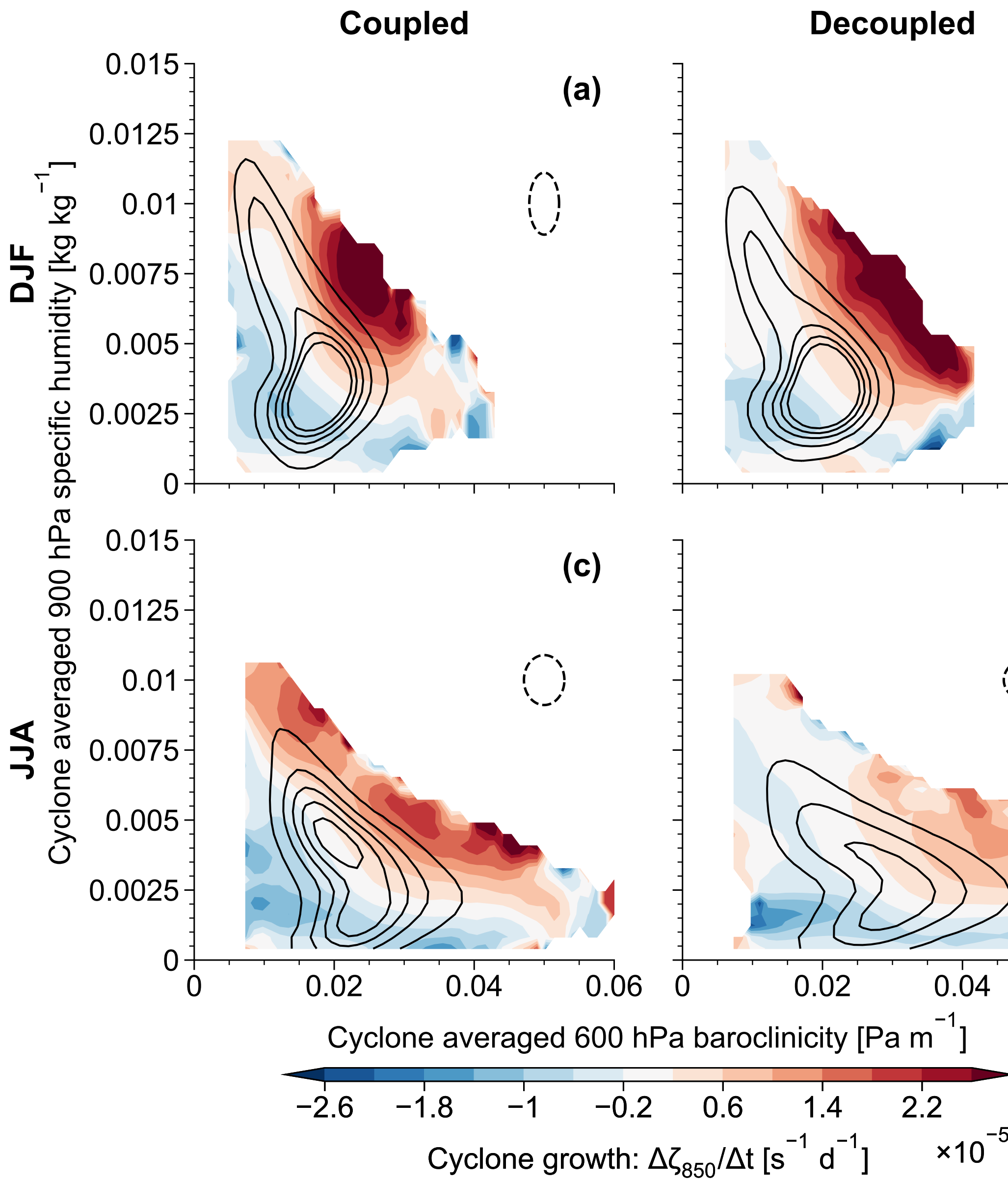

Figure 5.8: The shading shows cyclone intensification and decay in the space of cyclone averaged baroclinicity (horizontal axes) and specific humidity (vertical axes) in *Coupled* (a, c) and *Decoupled* (b, d) for December, January, February (a, b) and over June, July, and August (c, d). The black contours show the cyclone density in baroclinicity-moisture space for levels: 100, 300, 500, 700, 900 m Pa^{-1}. Here, we use all cyclones in the Southern Hemisphere. The black dashed ellipses illustrate the sizes of the elliptic filters used for the smoothing. See the text for the baroclinicity-moisture space density calculations.

winter.

To examine cyclone peak intensity as a function of baroclinicity and moisture, we average the baroclinicity and moisture experienced by the cyclones from the time of cyclogenesis to the time they reach peak vorticity. We only consider cyclones that peak 24 h or longer after genesis for this analysis. The shading in Fig. 5.9 a, b, d, e shows cyclone peak vorticity as a function of the experienced baroclinicity and moisture. Peak vorticity is overall higher in the *Coupled* run than in the *Decoupled* run. Peak vorticity is also enhanced in moist but weakly baroclinic environments when latent heating is coupled to the dynamics, consistent with the enhanced cyclone intensification in those regions (Fig. 5.8).

The cyclones experience more baroclinicity in austral winter than in austral summer and more moisture in austral summer than in austral winter (black contours in Figs. 5.8–5.9). When latent heating is coupled to the dynamics, the distribution of cyclones in baroclinicity-moisture space shifts from more baroclinic towards more moist environments (Fig. 5.9 c, f). This could be partly linked to the equatorward shift of storm tracks under coupling (Chapter 4).

Having shown that the latent heating feedback shifts the balance between moist and baroclinic cyclone growth, we now consider how this changes with +4 K forcing. In the global warming experiment, storms become moister and their environment less baroclinic (Fig. 5.10 a, c). Thus, from a cyclone perspective, the environment appears to moisten at the expense of baroclinicity, consistent with experiments increasing temperature and moisture in general circulation models (Pfahl et al. 2015b; Sinclair et al. 2020; Lutsko et al. 2024).

Despite the reduction in baroclinicity when coupling (Fig. 5.9 c, f), the strongest storms are about 20% more intense in the *Coupled* experiments than in the *Decoupled* experiments (Fig. 5.10 b, d). The global warming forcing yields a far smaller response

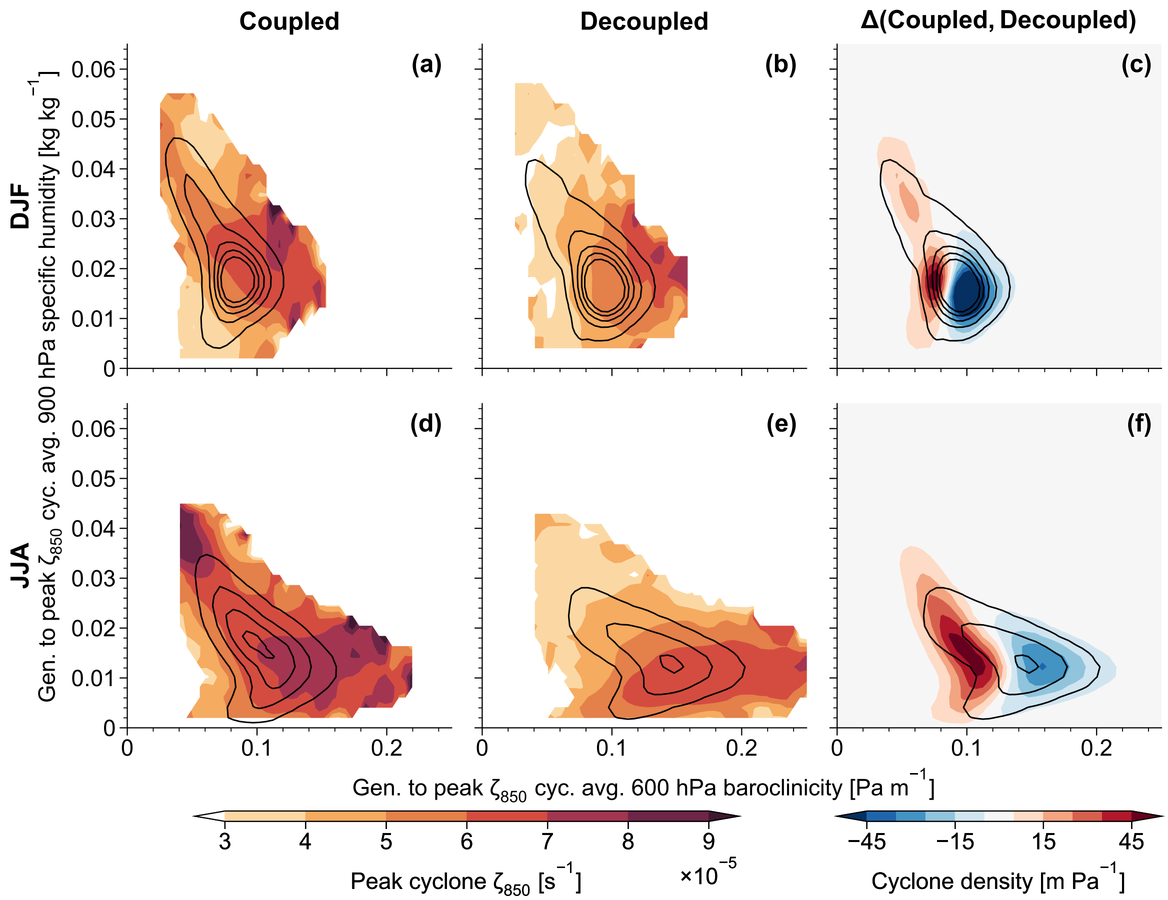

Figure 5.9: The shading in panels a, b, d, and e shows cyclone maximum 850 hPa vorticity in the space of the mean cyclone averaged baroclinicity (horizontal axes) and specific humidity (vertical axes) from genesis to peak vorticity in *Coupled* (a, c) and *Decoupled* (b, d) for December, January, February (a–c) and over June, July, and August (d–f). The contours show the cyclone density in baroclinicity-moisture space in the *Coupled* (a, d) and *Decoupled* (b, c, e, f) runs for levels: 10, 30, 50, 70, 90 m Pa^{-1}. The shading in Panels c and f shows the change in cyclone density due to the latent heating feedback. Here, we use all cyclones in the Southern Hemisphere that exist for at least 24 h before they reach peak vorticity. See text for the baroclinicity-moisture space density calculations.

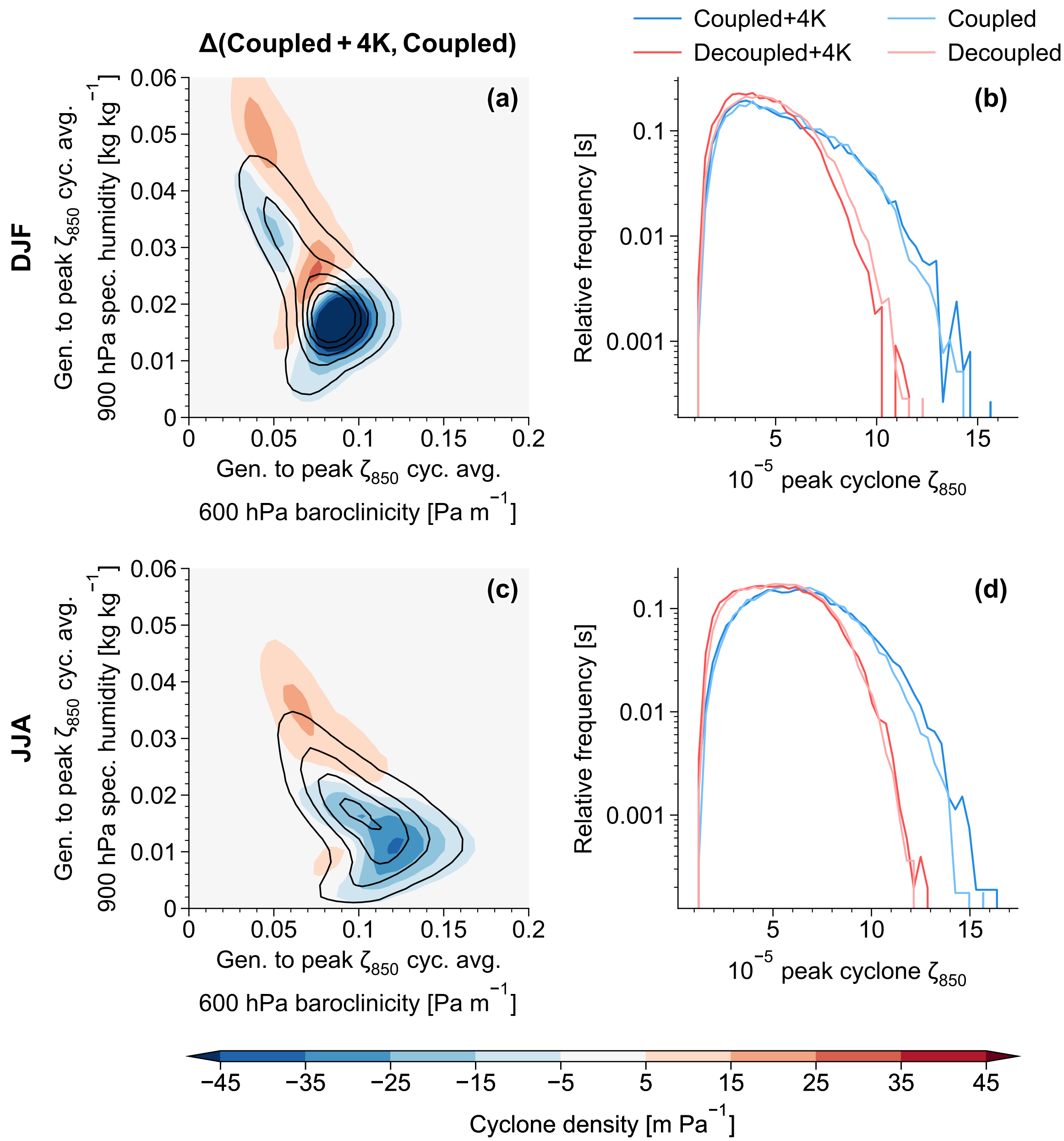

Figure 5.10: The shading in panels a and c are similar to Fig. 5.9 c, f but showing the change in cyclone density in baroclinicity-moisture space to global warming (+4 K) for December, January, February (a, b) and over June, July, and August (c, d). The contours in a and c show the cyclone density in *Coupled* for levels: 10, 30, 50, 70, 90 m Pa^{-1}. Panels b and d show the standardised histogram of peak cyclone 850 hPa vorticity for all four experiments. See text for the baroclinicity-moisture space density calculations.

in storm strength than decoupling latent heating from the dynamics. Yet, there are consistently a few more strong storms in the $Coupled + 4K$ run than in the $Coupled$ run, even though baroclinicity is reduced.

5.4 Conclusions

We quantify the contribution from the direct eddy amplification of latent heating to eddy kinetic energy and cyclone intensity by *decoupling* latent heating from the dynamics. By doing so in a climate resembling the present day and in a 4 K warmer climate, we can also assess the relative contribution from the *latent heating feedback* effect as the world warms. This set-up specifically tests the role of the change in the latent heating–dynamics coupling; the climatological-mean change in latent heating is distinct from this and have been discussed by e.g. Lachmy (2022).

Overall, the change in the latent heating feedback effect plays a leading order role in the storm track response to +4K forcing (Fig. 5.1), supporting the importance of model fidelity in simulating moist processes within cyclones (Willison et al. 2013; Willison et al. 2015; Hawcroft et al. 2017; Schemm 2023). The latent heating feedback unambiguously strengthens the lower-tropospheric eddy kinetic energy and cyclone vorticity, and this effect increases as the climate warms.

The feedback is most important in summer, independent of hemisphere, when moist airmasses extend to higher latitudes (Fig. 5.1 b, e). In summer, the latent heating feedback response is to strengthen eddy kinetic energy throughout the vertical column, and the strengthening of this effect under warming is responsible for most of the increase in eddy kinetic energy in the global warming experiment (Fig. 5.2 and Fig. 5.4). In winter, the contribution from the latent heating feedback to the total climate change signal is smaller, as the feedback reduces eddy kinetic energy in the upper troposphere but still increases eddy kinetic energy in the lower troposphere.

Latent heating coupled with the dynamics makes cyclones less dependent on forcing by upper-tropospheric waves, reducing the upper-tropospheric eddy kinetic energy (Fig. 5.7). Moisture-driven ascent reaches higher altitudes in summer compared to winter (Tierney et al. 2018), which seems to offset this effect. Summer cyclones also grow in less baroclinic but moister environments than winter cyclones (Fig. 5.8). Thus, the latent heating feedback likely has a larger influence on the distribution of summer cyclones as it is a more important growth mechanism in summer than in winter.

Focusing on the lower tropospheric storm intensity, we see that for a fixed climate, the strongest cyclones are $\sim 20\%$ more intense in the coupled simulations compared to the decoupled simulations (Fig. 5.10). For cyclone peak intensities, the effect of coupling within the same climate is far larger than the effect of +4 K forcing.

In the global warming experiment, cyclones grow in less baroclinic but moister environments (Fig. 5.9–5.10). Nevertheless, the cyclones reach similar or stronger peak intensities, which indicates that the increase in moist growth compensates for the reduction in baroclinicity, as has previously been demonstrated in aquaplanet simulations (Pfahl et al. 2015b; Sinclair et al. 2020).

Chapter 6

Synthesis, critique, and outlook

6.1 A short summary

In this thesis, we have shown that latent heating concentrates in regions where the jet stream transports warm, moist air poleward, sharpening the jet and amplifying upper-tropospheric waves (Chapter 3). This points to a coupled relationship between latent heating and the dynamics, which has largely been overlooked in previous efforts to understand the climatic impact of latent heating. Building on this, we presented a new modelling experiment showing that this coupling plays an important role in shaping the climate by strengthening storms and promoting their poleward propagation, suggesting that inadequate representation of latent heating contributes to long-standing biases in climate models (Chapter 4). Finally, we quantify how this coupling influences storminess in a global warming experiment, showing that latent heating increasingly affects storm intensity through direct amplification, which compensates for a reduction in baroclinicity (Chapter 5).

6.2 The original aim and why it failed

The original aim of my doctoral work was to examine the role of diabatic effects in jet and storm track variability; particularly, the role of latent heating for the persistence of meridional shifts in jets and storm tracks. As described in the Introduction in Chapter 3, we hypothesised that whether latent heating strengthens or weakens baroclinicity in the anomalous positions of the storm tracks could act to enhance or oppose the maintenance of the storm track in its anomalous position via a *baroclinic feedback mechanism*. That is, greater baroclinicity leads to larger eddy heat fluxes and enhanced vertical Rossby wave propagation that *could* lead to more Rossby wave divergence at upper levels, thus forcing a baroclinic jet in the anomalous position (Robinson 2000; Lorenz and Hartmann 2001; Xia and Chang 2014). Less baroclinicity, on the other hand, reduces eddy heat fluxes and vertical wave propagation, which, in turn, should reduce the divergence of Rossby waves at upper levels.

This turned out to be somewhat speculative; quantifying the relative contributions of the barotropic and baroclinic feedback mechanisms to annular modes is not trivial, yet to the extent possible, it appears that the baroclinic feedback mechanism plays a secondary role (Lorenz 2022).

It can also be discussed whether the methods of Chapter 3 successfully diagnose the effect of latent heating on baroclinicity. We diagnosed latent heating at a time instant around synoptic jets; we are only able to claim that latent heating typically strengthens the cross jet temperature contrast at that instant. While causing a net strengthening of the local baroclinicity (Papritz and Spengler 2015), latent heating also leads to enhanced updraughts and upper-level divergence. It remains unclear whether the local temperature perturbations from latent heating are sufficiently large to facilitate a subsequent baroclinic waves or whether it mainly perturbs the atmosphere in other ways.

One and a half years after publishing Auestad et al. (2024), my main takeaway from this paper is an intuitive graphical demonstration of the dependence of latent heating on the meridional wind and temperature, with latent heating occurring in the warm, moist poleward moving airmasses. This dependence is consistent with ridge amplification associated with latent heating (Methven 2015) and with the possible importance of latent heating for the persistence of blocking (Pfahl et al. 2015a).

6.3 The decoupling technique

6.3.1 Caveats

When designing the decoupled latent heating experiment (Chapter 4), the aim was still to assess the effect of coupled latent heating on the persistence of anomalous circulation patterns in the midlatitudes. We examined both blocking and annular mode persistence. However, the decoupling introduced such large mean-state changes that it was difficult to isolate any possible effects on variability. Thus, we instead examined the effects on the mean-state changes themselves.

We presented the effect of coupling latent heating to the dynamics as the coupled experiment minus the decoupled experiment (Chapter 4). When decoupling, a fixed climatology (with a seasonal cycle) of latent heating is prescribed in the model. This introduces a weak temperature forcing, likely negligible at a given time instant, yet non-negligible on climatic timescales. We argued that the equatorward jet shift due to coupling (Fig. 4.5) is caused by coupled latent heating effectively strengthening baroclinicity at lower latitudes than prescribed latent heating, which, in comparison, forces baroclinicity at higher latitudes and pushes the jet polewards. Thus, the effect is relative to an artificial baseline state, which must be kept in mind when discussing the real-world implications of this result.

6.3.2 Alternatives

We also experimented with changing the latent heat of vaporisation (L_v) parameter in CAM4 to test its effect on the mid-latitude storm tracks and jets. Bembenek et al. (2020) and Lutsko and Hell (2021) adopt a similar approach using a two-layer quasi-geostrophic channel model. For a spherical model domain, Suhas et al. (2022) demonstrate that increasing L_v in an aquaplanet model with uniform sea surface temperatures sets up a Hadley cell. In other words, the tropical circulation is very sensitive to the value of L_v, and changes to the tropical circulation tend to have extratropical consequences. In our case, we wanted a relatively realistic model domain, while leaving the tropical circulation undisturbed, and therefore did not vary L_v in the tropics. Increasing or decreasing L_v only in the extratropics would, however, create an energy imbalance between regions of evaporation and condensation.

Another option could be to maintain the amplitude and patchiness of the latent heating, but to decouple it from the dynamics by spatially shifting it away from regions of moist updraughts. This could, for example, be done by prescribing the full spatio-temporal latent heating field from the coupled run in the decoupled run in a random temporal order, or simply prescribing randomly generated latent heating. We did not pursue this approach.

As mentioned in Chapter 4, when Solomon (2006) redistribute occurrences of latent heating uniformly across latitudes, they observe mean-state changes similar to those in Auestad et al. (2025). This indicates that the results are likely not overly sensitive to the exact method of decoupling.

6.3.3 Advantages

The chosen decoupling technique may be just as — or even more — adequate than the aforementioned alternatives, depending on the research question. The main advantage of the decoupling technique used in Chapters 4–5 is that the coupled–decoupled pair of simulations have identical time mean latent heating in the extratropical free troposphere. In the time-zonal-mean heat budget, for example, diabatic heating is a linear term; thus, the eddy latent heating term vanishes (Lachmy and Kaspi 2020). Coupling latent heating is nevertheless able to modulate the time- and zonal-mean circulation, as it affects the eddy heat fluxes (see supplementary material in Auestad et al. 2025).

The mean-state changes, measured by zonal wind (not shown) and temperature (Fig. 5.3), between the coupled–decoupled pairs are also quite similar in the present-day and the 4 K warmer climate (Chapter 5). Thus, when estimating the change in the latent heating feedback with warming, $\Delta(Coupled + 4K, Decoupled + 4K) - \Delta(Coupled, Decoupled)$, most of the mean-state changes cancel out, while the eddy statistics and the Lagrangian-tracked cyclones clearly respond to changes in the latent heating feedback effect (Chapter 5).

6.4 Outlook

The diabatic influence on both the mean state and the variability of mid-latitude jets and storm tracks remains an open area of research. First of all, the effects, and the relative importance of, sensible heat fluxes, radiation, and latent heating for mid-latitude dynamics are active areas of research and seem dependent on the specific phenomenon under consideration (Hotta and Nakamura 2011; Li et al. 2014; Li et al. 2015; Ceppi and Hartmann 2015; Novak et al. 2015; Papritz and Spengler 2015; Novak et al. 2017;

Schäfer and Voigt 2018; Papavasileiou et al. 2020; Marcheggiani and Ambaum 2020; Marcheggiani and Spengler 2023).

I focused on latent heating, and note that the observational foundation could be improved. Hawcroft et al. (2017) compared cloud cover in ERA-Interim with satellite measurements, revealing biases in reanalysis latent heating. Although newer reanalysis products exist, they still approximate updraughts and (inevitably) cloud microphysics, and therefore still produce biased representations of latent heating. It would be useful to repeat the analysis of Chapter 3 using, for example, satellite measurements to assess whether the claim that latent heating occurs on the warm side of the jet also holds for more direct observations.

Although models and reanalyses inaccurately represent latent heating, there is compelling evidence that storm tracks become more realistic at higher resolution due to improved representations of latent heating (Willison et al. 2013; Willison et al. 2015; Schemm 2023). High-resolution models, ideally large eddy simulations, may therefore provide good test cases for diagnosing latent heating and its effects.

Another challenge is that climate diagnostics are not always trivially mapped onto weather. Diagnostics such as eddy kinetic energy, mean available potential energy, and the mean zonal wind can be linked through the zonal mean momentum budget, which makes them convenient for climate studies. While latent heating affects spatio-temporally averaged eddy kinetic energy via mean available potential energy and by direct eddy invigoration (Lutsko et al. 2024), we show in Chapter 5 that latent heating also exerts a more subtle influence on eddy kinetic energy as it modulates cyclone structure (consistent with Tierney et al. 2018). This effect seems important to consider to interpret the weather implications of projected changes in hemispheric mean eddy kinetic energy; in other words, while mean storminess is projected to decrease with warming (O'Gorman 2010; Lutsko et al. 2024) that is not necessarily the case for surface weather.

The method of decoupling could also be refined. For example, a more synoptic examination of the diabatic effect on the persistence of weather could include rerunning persistent blocking episodes (from simulation or reanalysis) and, for example, dampen latent heating in the close vicinity of the block to examine the effect on the block duration.

Furthermore, the simulations prescribe sea surface temperatures and sea ice, which influence storm tracks relative to coupled atmosphere–ocean simulations (Raible and Blender 2004). A coupled atmosphere–ocean framework should therefore be considered in future experiments, particularly when examining seasonal-to-subseasonal storm track variability (Marshall et al. 2001).

At last, whether the decoupling technique is robust across different climate models remains an open question. Solomon (2006) decoupled latent heating in CAM2; however, it would be valuable to repeat the experiment using models outside the Community Earth System Model framework.

6.5 Final remarks

This thesis is influenced by, and contributes to, two main trends in atmospheric science. First, as noted in the Introduction, it contributes to the growing body of research on moist dynamics. This line of research is motivated both by the need to explain discrepancies between theories based on dry dynamics and observations, and by the expectation that moist dynamics will become increasingly important as the atmosphere warms. Second, there is an increasing tendency to connect theories of climate with the weather phenomena through which climate is experienced. This thesis contributes to linking these scales, particularly in Chapter 3, by reconciling climate and weather perspectives on the jet stream and its associated latent heating.

In Chapter 4, we examine the implications of the findings from Chapter 3 for climate and find that they contribute to making the climate more zonally asymmetric. There is a long tradition of treating climate as zonally symmetric, with zonally asymmetric perturbations superimposed on this background state. Understanding these zonally asymmetric perturbations remains an active area of research and is crucial for understanding the regional and local weather associated with climate change.

In Chapter 5, we engage with a relatively recent and specific debate concerning whether latent heating acts to increase or decrease storm intensity further as the climate warms. We combine weather and climate based perspectives and diagnostics in order to add nuance to a question that has largely been discussed from either a climate perspective or a weather perspective in isolation.

Bibliography

Andrews, D. G. and M. E. McIntyre (1976). "Planetary Waves in Horizontal and Vertical Shear: The Generalized Eliassen-Palm Relation and the Mean Zonal Acceleration". In: *Journal of the Atmospheric Sciences* 33.11, pp. 2031–2048. DOI: 10.1175/1520-0469(1976)033<2031:PWIHAV>2.0.CO;2.

Auestad, H., A. Shibu, P. Ceppi, and T. Woollings (2025). "The Latent Heating Feedback on the Mid-Latitude Circulation". In: *Geophysical Research Letters* 52.18, e2025GL116437. DOI: 10.1029/2025GL116437.

— (2026). "The Latent Heating Feedback Effect on Storm Tracks in Current and Future Climates". In: *npj Climate and Atmospheric Science*. DOI: 10.1038/s41612-026-01421-9.

Auestad, H. et al. (2024). "Spatio-Temporal Averaging of Jets Obscures the Reinforcement of Baroclinicity by Latent Heating". In: *Weather and Climate Dynamics* 5.4, pp. 1269–1286. DOI: 10.5194/wcd-5-1269-2024.

Baker, H. S., T. Woollings, C. E. Forest, and M. R. Allen (2019). "The Linear Sensitivity of the North Atlantic Oscillation and Eddy-Driven Jet to SSTs". In: *Journal of Climate* 32.19, pp. 6491–6511. DOI: 10.1175/JCLI-D-19-0038.1.

Balasubramanian, G. and S. T. Garner (1997). "The Role of Momentum Fluxes in Shaping the Life Cycle of a Baroclinic Wave". In: *Journal of the Atmospheric Sciences* 54.4, pp. 510–533. DOI: 10.1175/1520-0469(1997)054<0510:TROMFI>2.0.CO;2.

Barnes, E. A., D. L. Hartmann, D. M. W. Frierson, and J. Kidston (2010). "Effect of Latitude on the Persistence of Eddy-Driven Jets". In: *Geophysical Research Letters* 37.11. DOI: 10.1029/2010GL043199.

Barnes, M. A., M. J. Reeder, and T. Ndarana (2025). "Rossby Wave Breaking Morphologies on the Southern Hemisphere Dynamical Tropopause". In: *Journal of Climate* 38.18, pp. 4825–4844. DOI: 10.1175/JCLI-D-24-0461.1.

Battalio, J. M. and J. M. Lora (2024). "Increases in the Local Eddy Energetics of the Extratropical Atmosphere over the Last Four Decades". In: *Journal of Climate* 37.12, pp. 3283–3304. DOI: 10.1175/JCLI-D-22-0930.1.

Beckett, G. et al. (2024). *ARCHER2 Service Description*. Tech. rep. Zenodo. DOI: 10.5281/zenodo.14507040.

Bembenek, E., D. N. Straub, and T. M. Merlis (2020). "Effects of Moisture in a Two-Layer Model of the Midlatitude Jet Stream". In: *Journal of the Atmospheric Sciences* 77.1, pp. 131–147. DOI: 10.1175/JAS-D-19-0021.1.

Blanco-Fuentes, J. and P. Zurita-Gotor (2011). "The Driving of Baroclinic Anomalies at Different Timescales". In: *Geophysical Research Letters* 38.23. DOI: 10.1029/2011GL049785.

Boettcher, M. and H. Wernli (2013). “A 10-Yr Climatology of Diabatic Rossby Waves in the Northern Hemisphere”. In: *Monthly Weather Review* 141.3, pp. 1139–1154. DOI: 10.1175/MWR-D-12-00012.1.

Bolton, D. (1980). “The Computation of Equivalent Potential Temperature”. In: *Monthly Weather Review* 108.7, pp. 1046–1053. DOI: 10.1175/1520-0493(1980)108<1046:TCOEPT>2.0.CO;2.

Booth, J. F., S. Wang, and L. Polvani (2013). “Midlatitude Storms in a Moister World: Lessons from Idealized Baroclinic Life Cycle Experiments”. In: *Climate Dynamics* 41.3, pp. 787–802. DOI: 10.1007/s00382-012-1472-3.

Breul, P., P. Ceppi, I. R. Simpson, and T. Woollings (2025). “Seasonal and Regional Jet Stream Changes and Drivers”. In: *Nature Reviews Earth & Environment* 6.12, pp. 824–842. DOI: 10.1038/s43017-025-00749-9.

Bukenberger, M., S. Rüdisühli, and S. Schemm (2023). “Jet Stream Dynamics from a Potential Vorticity Gradient Perspective: The Method and Its Application to a Kilometre-Scale Simulation”. In: *Quarterly Journal of the Royal Meteorological Society* 149.755, pp. 2409–2432. DOI: 10.1002/qj.4513.

Cai, M. and M. Mak (1990). “Symbiotic Relation between Planetary and Synoptic-Scale Waves”. In: *Journal of the Atmospheric Sciences* 47.24, pp. 2953–2968. DOI: 10.1175/1520-0469(1990)047<2953:SRBPAS>2.0.CO;2.

Catto, J. L. et al. (2019). “The Future of Midlatitude Cyclones”. In: *Current Climate Change Reports* 5.4, pp. 407–420. DOI: 10.1007/s40641-019-00149-4.

Ceppi, P. and D. L. Hartmann (2015). “Connections Between Clouds, Radiation, and Midlatitude Dynamics: A Review”. In: *Current Climate Change Reports* 1.2, pp. 94–102. DOI: 10.1007/s40641-015-0010-x.

Chang, E. K. M., S. Lee, and K. L. Swanson (2002). “Storm Track Dynamics”. In: *Journal of Climate* 15.16, pp. 2163–2183. DOI: 10.1175/1520-0442(2002)015<02163:STD>2.0.CO;2.

Chang, E. K. M. and I. Orlanski (1993). “On the Dynamics of a Storm Track”. In: *Journal of the Atmospheric Sciences* 50.7, pp. 999–1015. DOI: 10.1175/1520-0469(1993)050<0999:OTDOAS>2.0.CO;2.

Charney, J. G. (1947). “THE DYNAMICS OF LONG WAVES IN A BAROCLINIC WESTERLY CURRENT”. In: *Journal of the Atmospheric Sciences* 4.5, pp. 136–162. DOI: 10.1175/1520-0469(1947)004<0136:TDOLWI>2.0.CO;2.

Charney, J. G. and M. E. Stern (1962). “On the Stability of Internal Baroclinic Jets in a Rotating Atmosphere”. In: *Journal of the Atmospheric Sciences* 19.2, pp. 159–172. DOI: 10.1175/1520-0469(1962)019<0159:OTSOIB>2.0.CO;2.

Chemke, R. and D. Coumou (2024). “Human Influence on the Recent Weakening of Storm Tracks in Boreal Summer”. In: *npj Climate and Atmospheric Science* 7.1, p. 86. DOI: 10.1038/s41612-024-00640-2.

Chemke, R., Y. Ming, and J. Yuval (2022). “The Intensification of Winter Mid-Latitude Storm Tracks in the Southern Hemisphere”. In: *Nature Climate Change* 12.6, pp. 553–557. DOI: 10.1038/s41558-022-01368-8.

Danard, M. B. (1966). “On the Contribution of Released Latent Heat to Changes in Available Potential Energy”. In: *Journal of Applied Meteorology (1962-1982)* 5.1, pp. 81–84.

Drouard, M., G. Rivière, and P. Arbogast (2015). “The Link between the North Pacific Climate Variability and the North Atlantic Oscillation via Downstream Propagation of Synoptic Waves”. In: *Journal of Climate* 28.10, pp. 3957–3976. DOI: 10.1175/JCLI-D-14-00552.1.

Duchon, C. E. (1979). “Lanczos Filtering in One and Two Dimensions”. In: *Journal of Applied Meteorology and Climatology* 18.8, pp. 1016–1022. DOI: 10.1175/1520-0450(1979)018<1016:LFIOAT>2.0.CO;2.

Eady, E. T. (1949). “Long Waves and Cyclone Waves”. In: *Tellus* 1.3, pp. 33–52. DOI: 10.1111/j.2153-3490.1949.tb01265.x.

Edmon, H. J., B. J. Hoskins, and M. E. McIntyre (1980). “Eliassen-Palm Cross Sections for the Troposphere”. In: *Journal of the Atmospheric Sciences* 37.12, pp. 2600–2616. DOI: 10.1175/1520-0469(1980)037<2600:EPCSFT>2.0.CO;2.

Emanuel, K. A., M. Fantini, and A. J. Thorpe (1987). “Baroclinic Instability in an Environment of Small Stability to Slantwise Moist Convection. Part I: Two-Dimensional Models”. In: *Journal of the Atmospheric Sciences* 44.12, pp. 1559–1573. DOI: 10.1175/1520-0469(1987)044<1559:BIIAEO>2.0.CO;2.

Ford, R. P. and G. W. K. Moore (1990). “Secondary Cyclogenesis—Comparison of Observations and Theory”. In: *Monthly Weather Review* 118.2, pp. 427–446. DOI: 10.1175/1520-0493(1990)118<0427:SCOOAT>2.0.CO;2.

Hack, J. J. (1994). “Parameterization of Moist Convection in the National Center for Atmospheric Research Community Climate Model (CCM2)”. In: *Journal of Geophysical Research: Atmospheres* 99.D3, pp. 5551–5568. DOI: 10.1029/93JD03478.

Hall, N. M. J., B. J. Hoskins, P. J. Valdes, and C. A. Senior (1994). “Storm Tracks in a High-Resolution GCM with Doubled Carbon Dioxide”. In: *Quarterly Journal of the Royal Meteorological Society* 120.519, pp. 1209–1230. DOI: 10.1002/qj.49712051905.

Harvey, B. J., P. Cook, L. C. Shaffrey, and R. Schiemann (2020a). “The Response of the Northern Hemisphere Storm Tracks and Jet Streams to Climate Change in the CMIP3, CMIP5, and CMIP6 Climate Models”. In: *Journal of Geophysical Research: Atmospheres* 125.23, e2020JD032701. DOI: 10.1029/2020JD032701.

Harvey, B., J. Methven, C. Sanchez, and A. Schäfler (2020b). “Diabatic Generation of Negative Potential Vorticity and Its Impact on the North Atlantic Jet Stream”. In: *Quarterly Journal of the Royal Meteorological Society* 146.728, pp. 1477–1497. DOI: 10.1002/qj.3747.

Hawcroft, M. et al. (2017). “Using Satellite and Reanalysis Data to Evaluate the Representation of Latent Heating in Extratropical Cyclones in a Climate Model”. In: *Climate Dynamics* 48.7, pp. 2255–2278. DOI: 10.1007/s00382-016-3204-6.

Held, I. M. (1993). “Large-Scale Dynamics and Global Warming”. In: *Bulletin of the American Meteorological Society* 74.2, pp. 228–242. DOI: 10.1175/1520-0477(1993)074<0228:LSDAGW>2.0.CO;2.

Held, I. M. and A. Y. Hou (1980). “Nonlinear Axially Symmetric Circulations in a Nearly Inviscid Atmosphere”. In: *Journal of the Atmospheric Sciences* 37.3, pp. 515–533. DOI: 10.1175/1520-0469(1980)037<0515:NASCIA>2.0.CO;2.

Held, I. M., M. Ting, and H. Wang (2002). “Northern Winter Stationary Waves: Theory and Modeling”. In: *Journal of Climate* 15.16, pp. 2125–2144. DOI: 10.1175/1520-0442(2002)015<2125:NWSWTA>2.0.CO;2.

Hermoso, A. et al. (2024). “A Dynamical Interpretation of the Intensification of the Winter North Atlantic Jet Stream in Reanalysis”. In: *Journal of Climate* 37.22, pp. 5853–5881. DOI: 10.1175/JCLI-D-23-0757.1.

Hersbach, H. et al. (2020). “The ERA5 Global Reanalysis”. In: *Quarterly Journal of the Royal Meteorological Society* 146.730, pp. 1999–2049. DOI: 10.1002/qj.3803.

Hodges, K. I. (1994). “A General Method for Tracking Analysis and Its Application to Meteorological Data”. In: *Monthly Weather Review* 122.11, pp. 2573–2586. DOI: 10.1175/1520-0493(1994)122<2573:AGMFTA>2.0.CO;2.

— (1995). “Feature Tracking on the Unit Sphere”. In: *Monthly Weather Review* 123.12, pp. 3458–3465. DOI: 10.1175/1520-0493(1995)123<3458:FTOTUS>2.0.CO;2.

— (1996). “Spherical Nonparametric Estimators Applied to the UGAMP Model Integration for AMIP”. In: *Monthly Weather Review* 124.12, pp. 2914–2932. DOI: 10.1175/1520-0493(1996)124<2914:SNEATT>2.0.CO;2.

— (1999). “Adaptive Constraints for Feature Tracking”. In: *Monthly Weather Review* 127.6, pp. 1362–1373. DOI: 10.1175/1520-0493(1999)127<1362:ACFFT>2.0.CO;2.

Holton, J. R. and G. J. Hakim (2013). *An Introduction to Dynamic Meteorology*. Fifth edition. Amsterdam: Academic Press.

Hoskins, B. J., I. Draghici, and H. C. Davies (1978). “A New Look at the ω-Equation”. In: *Quarterly Journal of the Royal Meteorological Society* 104.439, pp. 31–38. DOI: 10.1002/qj.49710443903.

Hoskins, B. J. and K. I. Hodges (2005). “A New Perspective on Southern Hemisphere Storm Tracks”. In: *Journal of Climate* 18.20, pp. 4108–4129. DOI: 10.1175/JCLI3570.1.

Hoskins, B. J. and K. I. Hodges (2002). “New Perspectives on the Northern Hemisphere Winter Storm Tracks”. In: *Journal of the Atmospheric Sciences* 59.6, pp. 1041–1061. DOI: 10.1175/1520-0469(2002)059<1041:NPOTNH>2.0.CO;2.

Hoskins, B. J., I. N. James, and G. H. White (1983). “The Shape, Propagation and Mean-Flow Interaction of Large-Scale Weather Systems”. In: *Journal of the Atmospheric Sciences* 40.7, pp. 1595–1612. DOI: 10.1175/1520-0469(1983)040<1595:TSPAMF>2.0.CO;2.

Hoskins, B. J. and P. J. Valdes (1990). “On the Existence of Storm Tracks”. In: *Journal of Atmospheric Sciences* 47.15, pp. 1854–1864.

Hotta, D. and H. Nakamura (2011). “On the Significance of the Sensible Heat Supply from the Ocean in the Maintenance of the Mean Baroclinicity along Storm Tracks”. In: *Journal of Climate* 24.13, pp. 3377–3401. DOI: 10.1175/2010JCLI3910.1.

Hurrell, J. W. et al. (2008). “A New Sea Surface Temperature and Sea Ice Boundary Dataset for the Community Atmosphere Model”. In: *Journal of Climate* 21.19, pp. 5145–5153. DOI: 10.1175/2008JCLI2292.1.

Juckes, M. N. (2000). “The Static Stability of the Midlatitude Troposphere: The Relevance of Moisture”. In: *Journal of the Atmospheric Sciences* 57.18, pp. 3050–3057. DOI: 10.1175/1520-0469(2000)057<3050:TSSOTM>2.0.CO;2.

Karbi, I. and R. Chemke (2025). “Seasonally Asymmetric Projected Changes in Austral Atmospheric Waves”. In: *Geophysical Research Letters* 52.17, e2025GL117333. DOI: 10.1029/2025GL117333.

Kaspi, Y. and T. Schneider (2013). “The Role of Stationary Eddies in Shaping Midlatitude Storm Tracks”. In: *Journal of the Atmospheric Sciences* 70.8, pp. 2596–2613. DOI: 10.1175/JAS-D-12-082.1.

Kohl, M. and P. A. O’Gorman (2024). “Asymmetry of the Distribution of Vertical Velocities of the Extratropical Atmosphere in Theory, Models, and Reanalysis”. In: *Journal of the Atmospheric Sciences* 81.3, pp. 545–559. DOI: 10.1175/JAS-D-23-0128.1.

Konstali, K., C. Spensberger, T. Spengler, and A. Sorteberg (2024). “Global Attribution of Precipitation to Weather Features”. In: *Journal of Climate* 37.4, pp. 1181–1196. DOI: 10.1175/JCLI-D-23-0293.1.

Kundu, P. K. (2008). *Fluid Mechanics*. 4th ed. Amsterdam ; Academic Press.

Lachmy, O. (2022). “The Relation Between the Latitudinal Shifts of Midlatitude Diabatic Heating, Eddy Heat Flux, and the Eddy-Driven Jet in CMIP6 Models”. In: *Journal of Geophysical Research: Atmospheres* 127.16, e2022JD036556. DOI: 10.1029/2022JD036556.

Lachmy, O. and Y. Kaspi (2020). “The Role of Diabatic Heating in Ferrel Cell Dynamics”. In: *Geophysical Research Letters* 47.23, e2020GL090619. DOI: 10.1029/2020GL090619.

Laîné, A., G. Lapeyre, and G. Rivière (2011). “A Quasigeostrophic Model for Moist Storm Tracks”. In: *Journal of the Atmospheric Sciences* 68.6, pp. 1306–1322. DOI: 10.1175/2011JAS3618.1.

Laliberté, F., T. Shaw, and O. Pauluis (2012). “Moist Recirculation and Water Vapor Transport on Dry Isentropes”. In: *Journal of the Atmospheric Sciences* 69.3, pp. 875–890. DOI: 10.1175/JAS-D-11-0124.1.

Lee, S. and H.-k. Kim (2003). “The Dynamical Relationship between Subtropical and Eddy-Driven Jets”. In: *Journal of the Atmospheric Sciences* 60.12, pp. 1490–1503. DOI: 10.1175/1520-0469(2003)060<1490:TDRBSA>2.0.CO;2.

Li, Y., D. W. J. Thompson, and S. Bony (2015). “The Influence of Atmospheric Cloud Radiative Effects on the Large-Scale Atmospheric Circulation”. In: *Journal of Climate* 28.18, pp. 7263–7278. DOI: 10.1175/JCLI-D-14-00825.1.

Li, Y., D. W. J. Thompson, Y. Huang, and M. Zhang (2014). “Observed Linkages between the Northern Annular Mode/North Atlantic Oscillation, Cloud Incidence, and Cloud Radiative Forcing”. In: *Geophysical Research Letters* 41.5, pp. 1681–1688. DOI: 10.1002/2013GL059113.

Lindzen, R. S. and B. Farrell (1980). “A Simple Approximate Result for the Maximum Growth Rate of Baroclinic Instabilities”. In: *Journal of the Atmospheric Sciences* 37.7, pp. 1648–1654. DOI: 10.1175/1520-0469(1980)037<1648:ASARFT>2.0.CO;2.
Lorenz, D. J. (2022). “The Role of Barotropic versus Baroclinic Feedbacks on the Eddy Response to Annular Mode Zonal Wind Anomalies”. In: *Journal of the Atmospheric Sciences* 79.10, pp. 2529–2547. DOI: 10.1175/JAS-D-22-0061.1.
Lorenz, D. J. and D. L. Hartmann (2001). “Eddy–Zonal Flow Feedback in the Southern Hemisphere”. In: *Journal of the Atmospheric Sciences* 58.21, pp. 3312–3327. DOI: 10.1175/1520-0469(2001)058<3312:EZFFIT>2.0.CO;2.
Lorenz, E. N. (1955). “Available Potential Energy and the Maintenance of the General Circulation”. In: *Tellus* 7.2, pp. 157–167. DOI: 10.3402/tellusa.v7i2.8796.
— (1967). *The Nature and Theory of the General Circulation of the Atmosphere*. World Meteorological Organization.
Lutsko, N. J. and M. C. Hell (2021). “Moisture and the Persistence of Annular Modes”. In: *Journal of the Atmospheric Sciences* 78.12, pp. 3951–3964. DOI: 10.1175/JAS-D-21-0055.1.
Lutsko, N. J., J. Martinez-Claros, and D. D. B. Koll (2024). “Atmospheric Moisture Decreases Midlatitude Eddy Kinetic Energy”. In: *Journal of the Atmospheric Sciences* 81.11, pp. 1817–1832. DOI: 10.1175/JAS-D-23-0226.1.
Madonna, E., H. Wernli, H. Joos, and O. Martius (2014a). “Warm Conveyor Belts in the ERA-Interim Dataset (1979–2010). Part I: Climatology and Potential Vorticity Evolution”. In: *Journal of Climate* 27.1, pp. 3–26. DOI: 10.1175/JCLI-D-12-00720.1.
Madonna, E. et al. (2014b). “On the Co-Occurrence of Warm Conveyor Belt Outflows and PV Streamers”. In: *Journal of the Atmospheric Sciences* 71.10, pp. 3668–3673. DOI: 10.1175/JAS-D-14-0119.1.
Marcheggiani, A. and M. H. P. Ambaum (2020). “The Role of Heat-Flux–Temperature Covariance in the Evolution of Weather Systems”. In: *Weather and Climate Dynamics* 1.2, pp. 701–713. DOI: 10.5194/wcd-1-701-2020.
Marcheggiani, A. and T. Spengler (2023). “Diabatic Effects on the Evolution of Storm Tracks”. In: *Weather and Climate Dynamics* 4.4, pp. 927–942. DOI: 10.5194/wcd-4-927-2023.
Marshall, D. P., J. R. Maddison, and P. S. Berloff (2012). “A Framework for Parameterizing Eddy Potential Vorticity Fluxes”. In: *Journal of Physical Oceanography* 42.4, pp. 539–557. DOI: 10.1175/JPO-D-11-048.1.
Marshall, J. et al. (2001). “North Atlantic Climate Variability: Phenomena, Impacts and Mechanisms”. In: *International Journal of Climatology* 21.15, pp. 1863–1898. DOI: 10.1002/joc.693.
Martius, O., C. Schwierz, and H. C. Davies (2010). “Tropopause-Level Waveguides”. In: *Journal of the Atmospheric Sciences* 67.3, pp. 866–879. DOI: 10.1175/2009JAS2995.1.

Methven, J. (2015). "Potential Vorticity in Warm Conveyor Belt Outflow". In: *Quarterly Journal of the Royal Meteorological Society* 141.689, pp. 1065–1071. DOI: 10.1002/qj.2393.

Neale, R. B. et al. (2013). "The Mean Climate of the Community Atmosphere Model (CAM4) in Forced SST and Fully Coupled Experiments". In: *Journal of Climate* 26.14, pp. 5150–5168. DOI: 10.1175/JCLI-D-12-00236.1.

Novak, L., M. H. P. Ambaum, and R. Tailleux (2017). "Marginal Stability and Predator–Prey Behaviour within Storm Tracks". In: *Quarterly Journal of the Royal Meteorological Society* 143.704, pp. 1421–1433. DOI: 10.1002/qj.3014.

Novak, L., M. H. P. Ambaum, and R. Tailleux (2015). "The Life Cycle of the North Atlantic Storm Track". In: *Journal of the Atmospheric Sciences* 72.2, pp. 821–833. DOI: 10.1175/JAS-D-14-0082.1.

Novak, L. and R. Tailleux (2018). "On the Local View of Atmospheric Available Potential Energy". In: *Journal of the Atmospheric Sciences* 75.6, pp. 1891–1907. DOI: 10.1175/JAS-D-17-0330.1.

O'Gorman, P. A. (2010). "Understanding the Varied Response of the Extratropical Storm Tracks to Climate Change". In: *Proceedings of the National Academy of Sciences* 107.45, pp. 19176–19180. DOI: 10.1073/pnas.1011547107.

— (2011). "The Effective Static Stability Experienced by Eddies in a Moist Atmosphere". In: *Journal of the Atmospheric Sciences* 68.1, pp. 75–90. DOI: 10.1175/2010JAS3537.1.

O'Gorman, P. A. and T. Schneider (2008). "Energy of Midlatitude Transient Eddies in Idealized Simulations of Changed Climates". In: *Journal of Climate* 21.22, pp. 5797–5806. DOI: 10.1175/2008JCLI2099.1.

Orlanski, I. and J. Katzfey (1991). "The Life Cycle of a Cyclone Wave in the Southern Hemisphere. Part I: Eddy Energy Budget". In: *Journal of the Atmospheric Sciences* 48.17, pp. 1972–1998. DOI: 10.1175/1520-0469(1991)048<1972:TLCOAC>2.0.CO;2.

Orlanski, I. (2003). "Bifurcation in Eddy Life Cycles: Implications for Storm Track Variability". In: *Journal of the Atmospheric Sciences* 60.8, pp. 993–1023. DOI: 10.1175/1520-0469(2003)60<993:BIELCI>2.0.CO;2.

Ossó, A. et al. (2024). "Advancing Our Understanding of Eddy-driven Jet Stream Responses to Climate Change – A Roadmap". In: *Current Climate Change Reports* 11.1, p. 2. DOI: 10.1007/s40641-024-00199-3.

Papavasileiou, G., A. Voigt, and P. Knippertz (2020). "The Role of Observed Cloud-Radiative Anomalies for the Dynamics of the North Atlantic Oscillation on Synoptic Time-Scales". In: *Quarterly Journal of the Royal Meteorological Society* 146.729, pp. 1822–1841. DOI: 10.1002/qj.3768.

Papritz, L. and T. Spengler (2015). "Analysis of the Slope of Isentropic Surfaces and Its Tendencies over the North Atlantic". In: *Quarterly Journal of the Royal Meteorological Society* 141.693, pp. 3226–3238. DOI: 10.1002/qj.2605.

Parker, D. J. and A. J. Thorpe (1995). "Conditional Convective Heating in a Baroclinic Atmosphere: A Model of Convective Frontogenesis". In: *Journal of the Atmospheric*

Sciences 52.10, pp. 1699–1711. DOI: 10.1175/1520-0469(1995)052<1699:CCHIAB>2.0.CO;2.

Pauluis, O., A. Czaja, and R. Korty (2010). "The Global Atmospheric Circulation in Moist Isentropic Coordinates". In: *Journal of Climate* 23.11, pp. 3077–3093. DOI: 10.1175/2009JCLI2789.1.

Pedlosky, J. (1964). "The Stability of Currents in the Atmosphere and the Ocean: Part I". In: *Journal of the Atmospheric Sciences* 21.2, pp. 201–219. DOI: 10.1175/1520-0469(1964)021<0201:TSOCIT>2.0.CO;2.

— (1987). *Geophysical Fluid Dynamics*. New York, NY: Springer. DOI: 10.1007/978-1-4612-4650-3.

Pfahl, S. et al. (2015a). "Importance of Latent Heat Release in Ascending Air Streams for Atmospheric Blocking". In: *Nature Geoscience* 8.8, pp. 610–614. DOI: 10.1038/ngeo2487.

Pfahl, S., P. A. O'Gorman, and M. S. Singh (2015b). "Extratropical Cyclones in Idealized Simulations of Changed Climates". In: *Journal of Climate* 28.23, pp. 9373–9392. DOI: 10.1175/JCLI-D-14-00816.1.

Priestley, M. D. K. and J. L. Catto (2022). "Future Changes in the Extratropical Storm Tracks and Cyclone Intensity, Wind Speed, and Structure". In: *Weather and Climate Dynamics* 3.1, pp. 337–360. DOI: 10.5194/wcd-3-337-2022.

Priestley, M. D. K. et al. (2020). "An Overview of the Extratropical Storm Tracks in CMIP6 Historical Simulations". In: *Journal of Climate* 33.15, pp. 6315–6343. DOI: 10.1175/JCLI-D-19-0928.1.

Raible, C. C. and R. Blender (2004). "Northern Hemisphere Midlatitude Cyclone Variability in GCM Simulations with Different Ocean Representations". In: *Climate Dynamics* 22.2, pp. 239–248. DOI: 10.1007/s00382-003-0380-y.

Raible, C. C., B. Ziv, H. Saaroni, and M. Wild (2010). "Winter Synoptic-Scale Variability over the Mediterranean Basin under Future Climate Conditions as Simulated by the ECHAM5". In: *Climate Dynamics* 35.2-3, pp. 473–488. DOI: 10.1007/s00382-009-0678-5.

Rasch, P. J. and J. E. Kristjánsson (1998). "A Comparison of the CCM3 Model Climate Using Diagnosed and Predicted Condensate Parameterizations". In: *Journal of Climate* 11.7, pp. 1587–1614. DOI: 10.1175/1520-0442(1998)011<1587:ACOTCM>2.0.CO;2.

Rhines, P. B. (1975). "Waves and Turbulence on a Beta-Plane". In: *Journal of Fluid Mechanics* 69.3, pp. 417–443. DOI: 10.1017/S0022112075001504.

Rivière, G. (2009). "Effect of Latitudinal Variations in Low-Level Baroclinicity on Eddy Life Cycles and Upper-Tropospheric Wave-Breaking Processes". In: *Journal of the Atmospheric Sciences* 66.6, pp. 1569–1592. DOI: 10.1175/2008JAS2919.1.

Robinson, W. A. (2000). "A Baroclinic Mechanism for the Eddy Feedback on the Zonal Index". In: *Journal of the Atmospheric Sciences* 57.3, pp. 415–422. DOI: 10.1175/1520-0469(2000)057<0415:ABMFTE>2.0.CO;2.

— (2006). "On the Self-Maintenance of Midlatitude Jets". In: *Journal of the Atmospheric Sciences* 63.8, pp. 2109–2122. DOI: 10.1175/JAS3732.1.

Schäfer, S. A. K. and A. Voigt (2018). “Radiation Weakens Idealized Midlatitude Cyclones”. In: *Geophysical Research Letters* 45.6, pp. 2833–2841. DOI: 10.1002/2017GL076726.

Schemm, S. (2023). “Toward Eliminating the Decades-Old “Too Zonal and Too Equatorward” Storm-Track Bias in Climate Models”. In: *Journal of Advances in Modeling Earth Systems* 15.2, e2022MS003482. DOI: 10.1029/2022MS003482.

Schneider, T. (2006). “The General Circulation of the Atmosphere”. In: *Annual Review of Earth and Planetary Sciences* 34.Volume 34, 2006, pp. 655–688. DOI: 10.1146/annurev.earth.34.031405.125144.

Schneider, T. and C. C. Walker (2006). “Self-Organization of Atmospheric Macroturbulence into Critical States of Weak Nonlinear Eddy–Eddy Interactions”. In: *Journal of the Atmospheric Sciences* 63.6, pp. 1569–1586. DOI: 10.1175/JAS3699.1.

Shaw, T. A. et al. (2016). “Storm Track Processes and the Opposing Influences of Climate Change”. In: *Nature Geoscience* 9.9, pp. 656–664. DOI: 10.1038/ngeo2783.

Simmons, A. J. and B. J. Hoskins (1978). “The Life Cycles of Some Nonlinear Baroclinic Waves”. In: *Journal of the Atmospheric Sciences* 35.3, pp. 414–432. DOI: 10.1175/1520-0469(1978)035<0414:TLCOSN>2.0.CO;2.

Sinclair, V. A. et al. (2020). “The Characteristics and Structure of Extra-Tropical Cyclones in a Warmer Climate”. In: *Weather and Climate Dynamics* 1.1, pp. 1–25. DOI: 10.5194/wcd-1-1-2020.

Solomon, A. (2006). “Impact of Latent Heat Release on Polar Climate”. In: *Geophysical Research Letters* 33.7. DOI: 10.1029/2005GL025607.

Spensberger, C. (2024). *Dynlib: A Library of Diagnostics, Feature Detection Algorithms, Plotting and Convenience Functions for Dynamic Meteorology*. Zenodo. DOI: 10.5281/zenodo.10471187.

Spensberger, C., C. Li, and T. Spengler (2023). “Linking Instantaneous and Climatological Perspectives on Eddy-Driven and Subtropical Jets”. In: *Journal of Climate* -1.aop. DOI: 10.1175/JCLI-D-23-0080.1.

Spensberger, C., T. Spengler, and C. Li (2017). “Upper-Tropospheric Jet Axis Detection and Application to the Boreal Winter 2013/14”. In: *Monthly Weather Review* 145.6, pp. 2363–2374. DOI: 10.1175/MWR-D-16-0467.1.

Suhas, D. L., J. Sukhatme, and N. Harnik (2022). “Dry and Moist Atmospheric Circulation with Uniform Sea-Surface Temperature”. In: *Quarterly Journal of the Royal Meteorological Society* 148.742, pp. 35–56. DOI: 10.1002/qj.4191.

Swanson, K. L. and R. T. Pierrehumbert (1997). “Lower-Tropospheric Heat Transport in the Pacific Storm Track”. In: *Journal of the Atmospheric Sciences* 54.11, pp. 1533–1543. DOI: 10.1175/1520-0469(1997)054<1533:LTHTIT>2.0.CO;2.

Tamarin, T. and Y. Kaspi (2016). “The Poleward Motion of Extratropical Cyclones from a Potential Vorticity Tendency Analysis”. In: *Journal of the Atmospheric Sciences* 73.4, pp. 1687–1707. DOI: 10.1175/JAS-D-15-0168.1.

Teubler, F. and M. Riemer (2021). “Potential-Vorticity Dynamics of Troughs and Ridges within Rossby Wave Packets during a 40-Year Reanalysis Period”. In: *Weather and Climate Dynamics* 2.3, pp. 535–559. DOI: 10.5194/wcd-2-535-2021.

Thorncroft, C. D., B. J. Hoskins, and M. E. McIntyre (1993). "Two Paradigms of Baroclinic-Wave Life-Cycle Behaviour". In: *Quarterly Journal of the Royal Meteorological Society* 119.509, pp. 17–55. DOI: 10.1002/qj.49711950903.

Tierney, G., D. J. Posselt, and J. F. Booth (2018). "An Examination of Extratropical Cyclone Response to Changes in Baroclinicity and Temperature in an Idealized Environment". In: *Climate Dynamics* 51.9, pp. 3829–3846. DOI: 10.1007/s00382-018-4115-5.

Trenberth, K. E. and D. P. Stepaniak (2003). "Covariability of Components of Poleward Atmospheric Energy Transports on Seasonal and Interannual Timescales". In: *Journal of Climate* 16.22, pp. 3691–3705. DOI: 10.1175/1520-0442(2003)016<3691:COCOPA>2.0.CO;2.

Vallis, G. K. (1992). "Mechanisms and Parameterizations of Geostrophic Adjustment and a Variational Approach to Balanced Flow". In: *Journal of the Atmospheric Sciences* 49.13, pp. 1144–1160. DOI: 10.1175/1520-0469(1992)049<1144:MAPOGA>2.0.CO;2.

— (2017). *Atmospheric and Oceanic Fluid Dynamics: Fundamentals and Large-Scale Circulation*. 2nd ed. Cambridge: Cambridge University Press. DOI: 10.1017/9781107588417.

Wang, P. K. (2013). *Physics and Dynamics of Clouds and Precipitation*. Cambridge: Cambridge University Press. DOI: 10.1017/CBO9780511794285.

Weijenborg, C. and T. Spengler (2020). "Diabatic Heating as a Pathway for Cyclone Clustering Encompassing the Extreme Storm Dagmar". In: *Geophysical Research Letters* 47.8, e2019GL085777. DOI: 10.1029/2019GL085777.

Wernli, H. and S. L. Gray (2024). "The Importance of Diabatic Processes for the Dynamics of Synoptic-Scale Extratropical Weather Systems – a Review". In: *Weather and Climate Dynamics* 5.4, pp. 1299–1408. DOI: 10.5194/wcd-5-1299-2024.

White, I. P., O. Lachmy, and N. Harnik (2024). "Influence of a Local Diabatic Heating Source on the Midlatitude Circulation". In: *Quarterly Journal of the Royal Meteorological Society* 150.765, pp. 5167–5187. DOI: 10.1002/qj.4863.

Wilks, D. S. (2016). ""The Stippling Shows Statistically Significant Grid Points": How Research Results Are Routinely Overstated and Overinterpreted, and What to Do about It". In: *Bulletin of the American Meteorological Society* 97.12, pp. 2263–2273. DOI: 10.1175/BAMS-D-15-00267.1.

Willison, J., W. A. Robinson, and G. M. Lackmann (2013). "The Importance of Resolving Mesoscale Latent Heating in the North Atlantic Storm Track". In: *Journal of the Atmospheric Sciences* 70.7, pp. 2234–2250. DOI: 10.1175/JAS-D-12-0226.1.

— (2015). "North Atlantic Storm-Track Sensitivity to Warming Increases with Model Resolution". In: *Journal of Climate* 28.11, pp. 4513–4524. DOI: 10.1175/JCLI-D-14-00715.1.

Wirth, V., M. Riemer, E. K. M. Chang, and O. Martius (2018). "Rossby Wave Packets on the Midlatitude Waveguide—A Review". In: *Monthly Weather Review* 146.7, pp. 1965–2001. DOI: 10.1175/MWR-D-16-0483.1.

WMO, W. M. O. (1966). *International Meteorological Tables*. Geneva.

Woollings, T., A. Hannachi, and B. Hoskins (2010). "Variability of the North Atlantic Eddy-Driven Jet Stream". In: *Quarterly Journal of the Royal Meteorological Society* 136.649, pp. 856–868. DOI: 10.1002/qj.625.

Woollings, T., B. Hoskins, M. Blackburn, and P. Berrisford (2008). "A New Rossby Wave–Breaking Interpretation of the North Atlantic Oscillation". In: *Journal of the Atmospheric Sciences* 65.2, pp. 609–626. DOI: 10.1175/2007JAS2347.1.

Woollings, T., L. Papritz, C. Mbengue, and T. Spengler (2016). "Diabatic Heating and Jet Stream Shifts: A Case Study of the 2010 Negative North Atlantic Oscillation Winter". In: *Geophysical Research Letters* 43.18, pp. 9994–10, 002. DOI: 10.1002/2016GL070146.

Woollings, T. et al. (2023). "Trends in the Atmospheric Jet Streams Are Emerging in Observations and Could Be Linked to Tropical Warming". In: *Communications Earth & Environment* 4.1, pp. 1–8. DOI: 10.1038/s43247-023-00792-8.

Xia, X. and E. K. M. Chang (2014). "Diabatic Damping of Zonal Index Variations". In: *Journal of the Atmospheric Sciences* 71.8, pp. 3090–3105. DOI: 10.1175/JAS-D-13-0292.1.

Yamada, R. and O. Pauluis (2015). "Annular Mode Variability of the Atmospheric Meridional Energy Transport and Circulation". In: *Journal of the Atmospheric Sciences* 72.5, pp. 2070–2089. DOI: 10.1175/JAS-D-14-0219.1.

— (2017). "Wave–Mean-Flow Interactions in Moist Baroclinic Life Cycles". In: *Journal of the Atmospheric Sciences* 74.7, pp. 2143–2162. DOI: 10.1175/JAS-D-16-0329.1.

Yao, Y., Y. Zhang, K. I. Hodges, and T. Tamarin-Brodsky (2023). "Different Propagation Mechanisms of Deep and Shallow Wintertime Extratropical Cyclones over the North Pacific". In: *Journal of Climate* 36.23, pp. 8277–8297. DOI: 10.1175/JCLI-D-22-0674.1.

Zhang, G. and N. A. McFarlane (1995). "Sensitivity of Climate Simulations to the Parameterization of Cumulus Convection in the Canadian Climate Centre General Circulation Model". In: *Atmosphere-Ocean* 33.3, pp. 407–446. DOI: 10.1080/07055900.1995.9649539.

Zhang, G. and Z. Wang (2018). "North Atlantic Extratropical Rossby Wave Breaking during the Warm Season: Wave Life Cycle and Role of Diabatic Heating". In: *Monthly Weather Review* 146.3, pp. 695–712. DOI: 10.1175/MWR-D-17-0204.1.

Zurita-Gotor, P., J. Blanco-Fuentes, and E. P. Gerber (2014). "The Impact of Baroclinic Eddy Feedback on the Persistence of Jet Variability in the Two-Layer Model". In: *Journal of the Atmospheric Sciences* 71.1, pp. 410–429. DOI: 10.1175/JAS-D-13-0102.1.

Appendix A

Supplementary material to Auestad et al. 2024

A.1 On the variability of the across-jet latent heating

As mentioned in Sect. 3.4, the jet conditional climatologies are coarse grained by binning the data and averaging over the members in each bin. Although the pattern clearly indicates more latent heating on the warm flank of the 3h-2D jets, the spread within each of the bins comprising Figs. 3.8, 3.9 is quite large (not shown). Figure A.1 summarises the results for 3h-2D jet cross sections by showing the difference in latent heating averaged over the cold side and subtracted from latent heating averaged over the warm side (ΔLH) when total latent heating is distinctively different from zero. There is an overweight of positive ΔLH occurrences (red), meaning that latent heating mostly strengthen the cross-jet temperature contrast. The distribution of ΔLH is negatively skewed and has similar extreme values on the positive and negative sides.

We can only trust Figs. 3.3-3.6 to be representative of the typical jet-latent heating relationship where the jet sample size is sufficiently large. Note that the number of 10d-Z jets poleward of 60° is particularly sparse and therefore might not be representative for jets there (Fig. A.2).

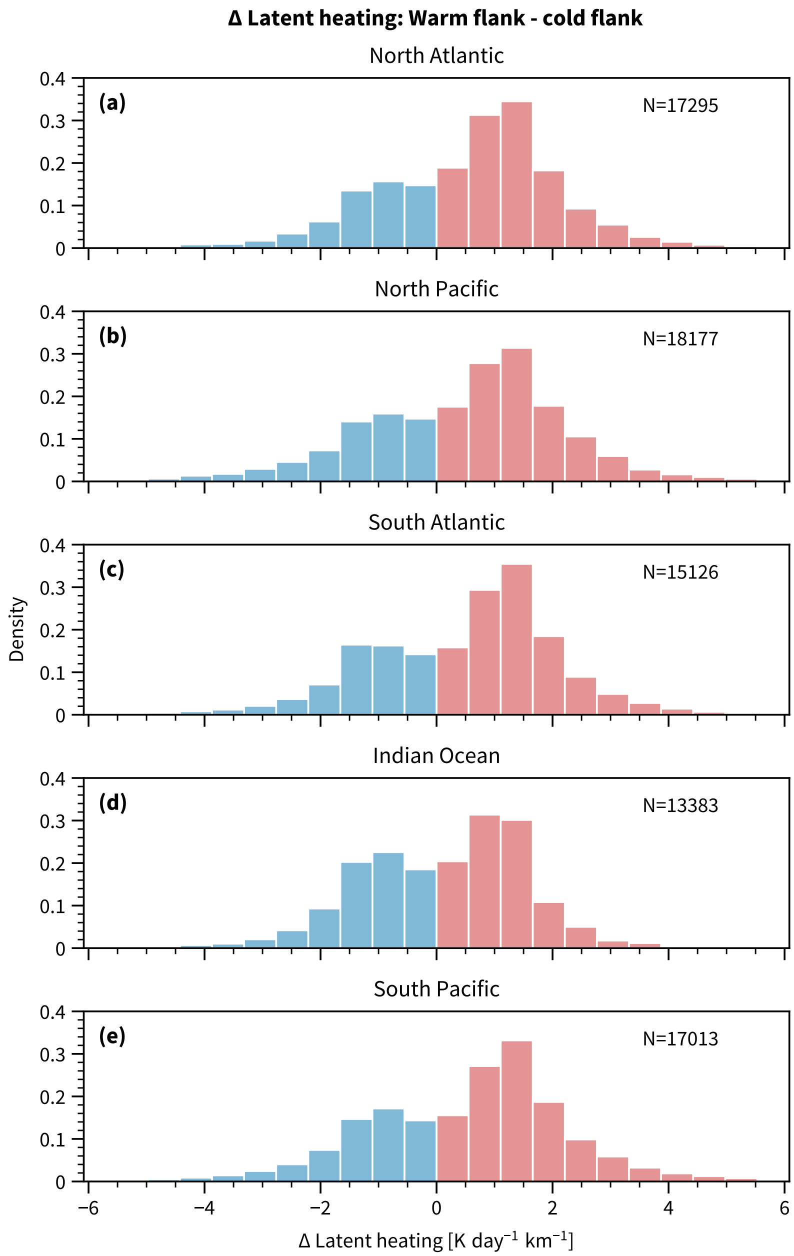

Figure A.1: Latent heating averaged over the warm flank minus latent heating averaged over the cold flank for the cross sections sampled for the 3h-2D jets for the five major storm track regions (see Fig. 3.8f) in their respective winter season. Red bars indicate a strengthening ($\Delta LH > 0$) and blue bars a weakening of the cross-jet temperature contrast ($\Delta LH < 0$). Only jet cross sections where the mean latent heating computed over both flanks exceeding 1 $K\ s^{-1}\ km^{-1}$ are shown, where N is the number of cross sections satisfying this criterion.

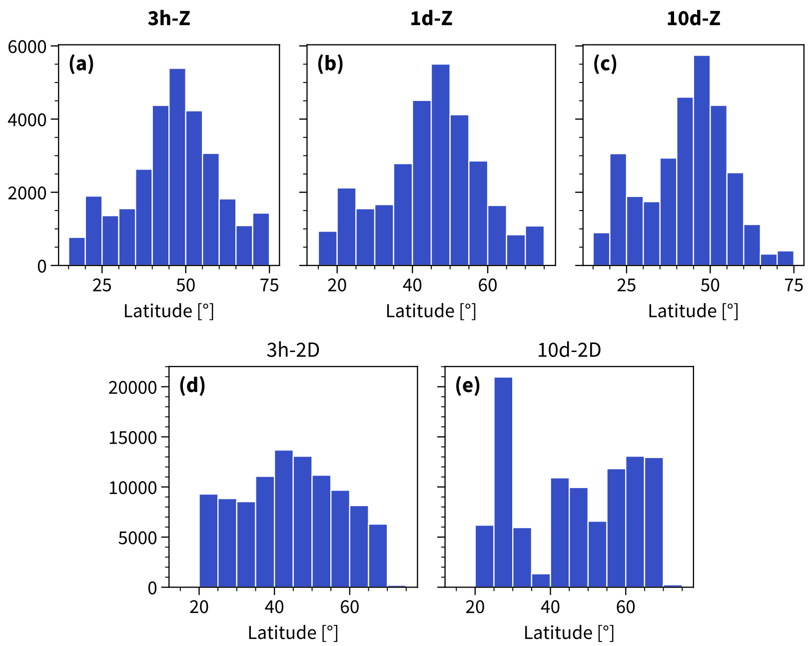

Figure A.2: Jet sample size as a function of latitude for the five different jet representations (Table 3.1). Showing the distribution of zonal jet latitudes (top row) and the latitudes of the two-dimensional jet cross-sections (bottom row).

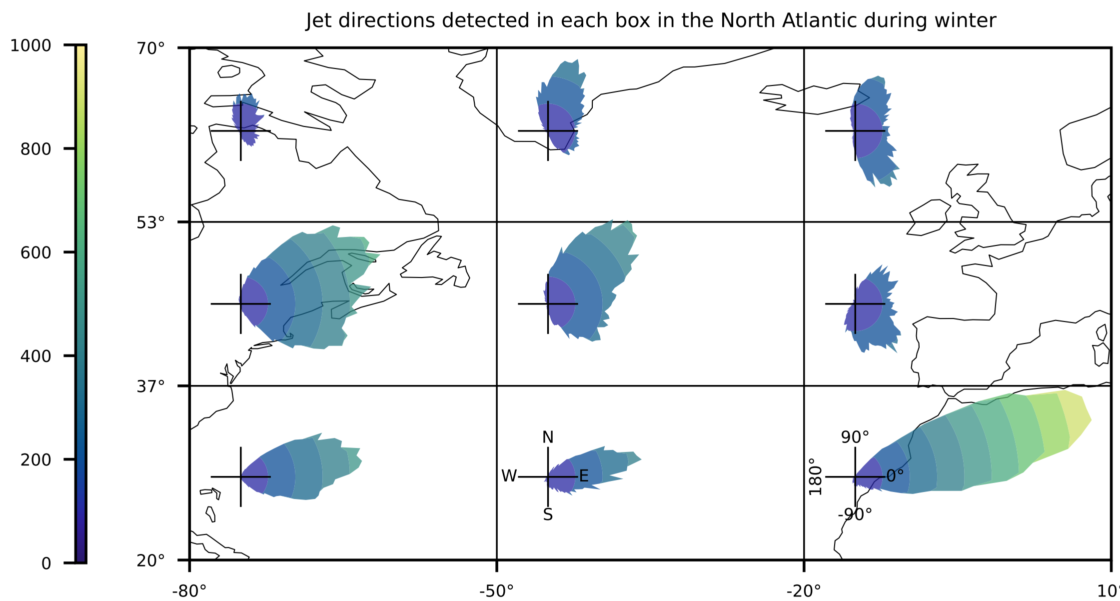

Figure A.3: Wind rose representation of the 3h-2D jet directions comprising the 100,000 cross sections sampled in the North Atlantic winter. Each wind rose represents the jet directions of the cross-sections in the respective box (black grid). The jet directions are binned in intervals of 1° and the colour shading refers the count over each bin. The lower middle and right panels show the cardinal directions and the corresponding jet directions for reference.

A.2 Easterly jets

Figure A.3 gives an overview of the 3h-2D jet directions. The African subtropical jet is most frequently detected, followed by a large number of jet directions between ±45° over and downstream of the Gulf Stream. Roughly 90 percent of the jets in the NA are westerlies. The remaining 10 percent are easterlies and are on average weaker than the westerly jets (Fig. A.4a). Updraft, moisture, latent heating, and large-scale precipitation are all larger on the warm side (outer circle) compared to the cold side (inner circle) for the poleward oriented jets (Fig. A.4b-e). The easterly jet directions in Fig. 3.1b seem to be associated with the bent back front of the easternmost cyclone. As the 3h-2D jet bends towards the east, the right flank must be warmer than the left

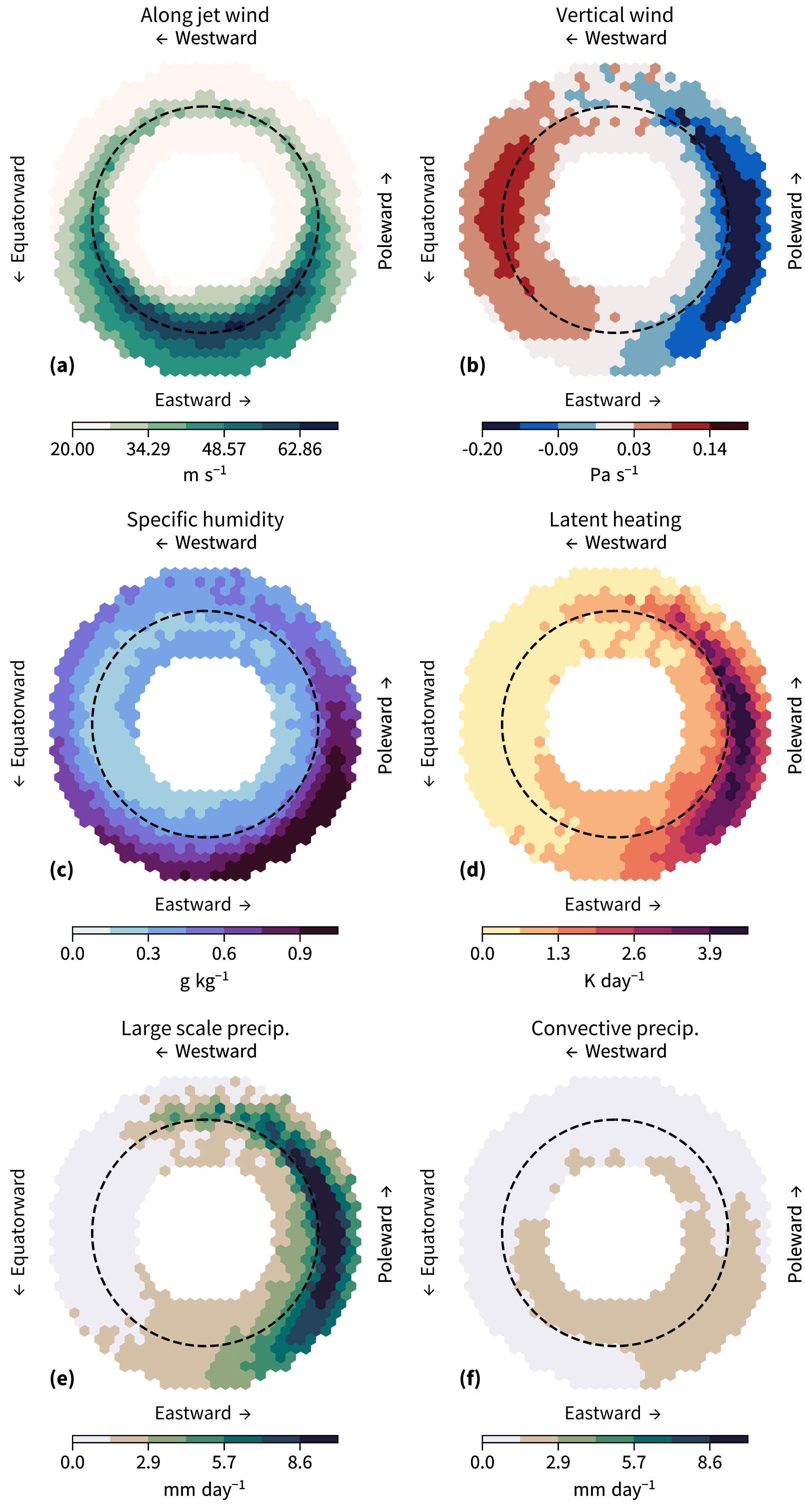

Figure A.4: Like Fig. 3.7, but for all jet directions.

flank by thermal wind, where also the heating occurs. To the north of the bent back front, another westerly jet exists, separating the warmer air over the bent back front from the colder air in the north.

Appendix B

Supplementary material to Auestad et al. 2025

B.1 June, July, and August

Figures B.1–B.4 show June, July, and August versions of Figs. 4.2–4.5.

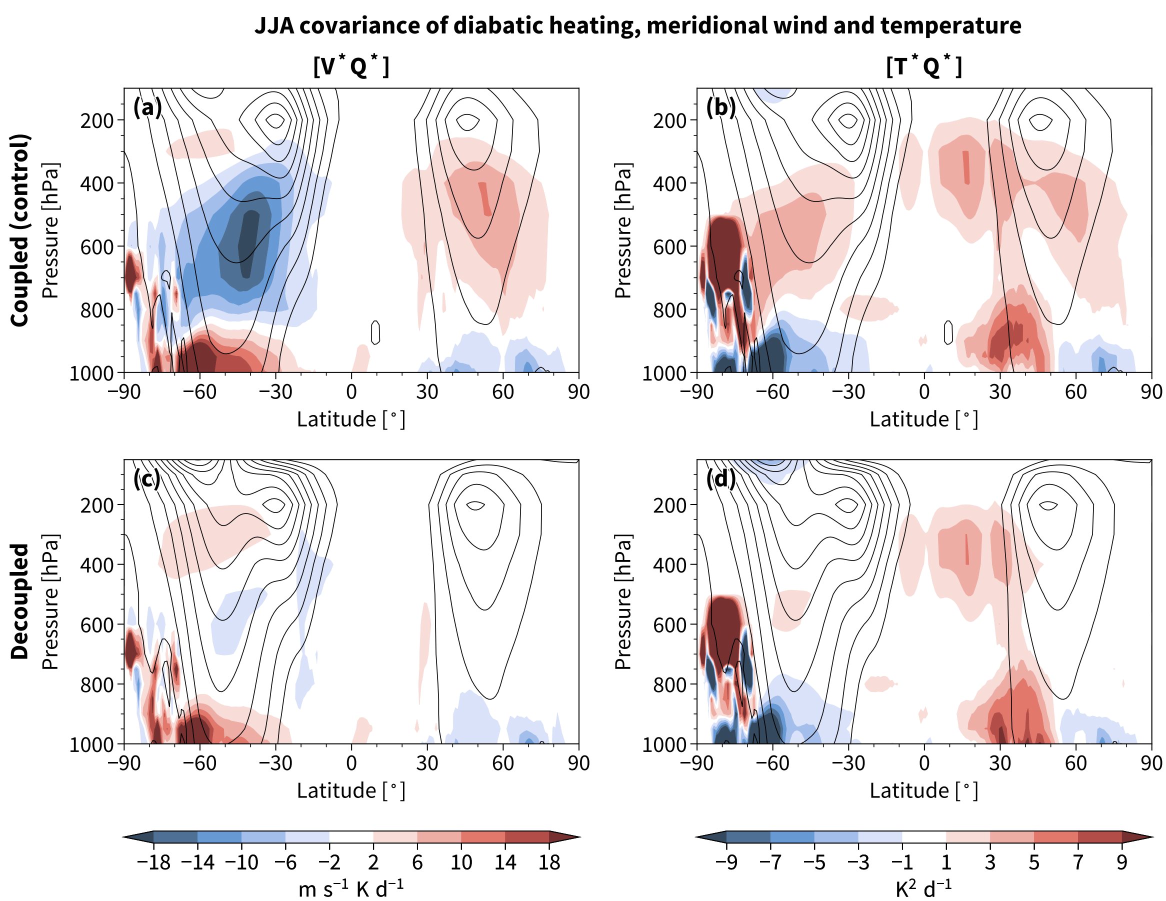

Figure B.1: Like Fig 4.2

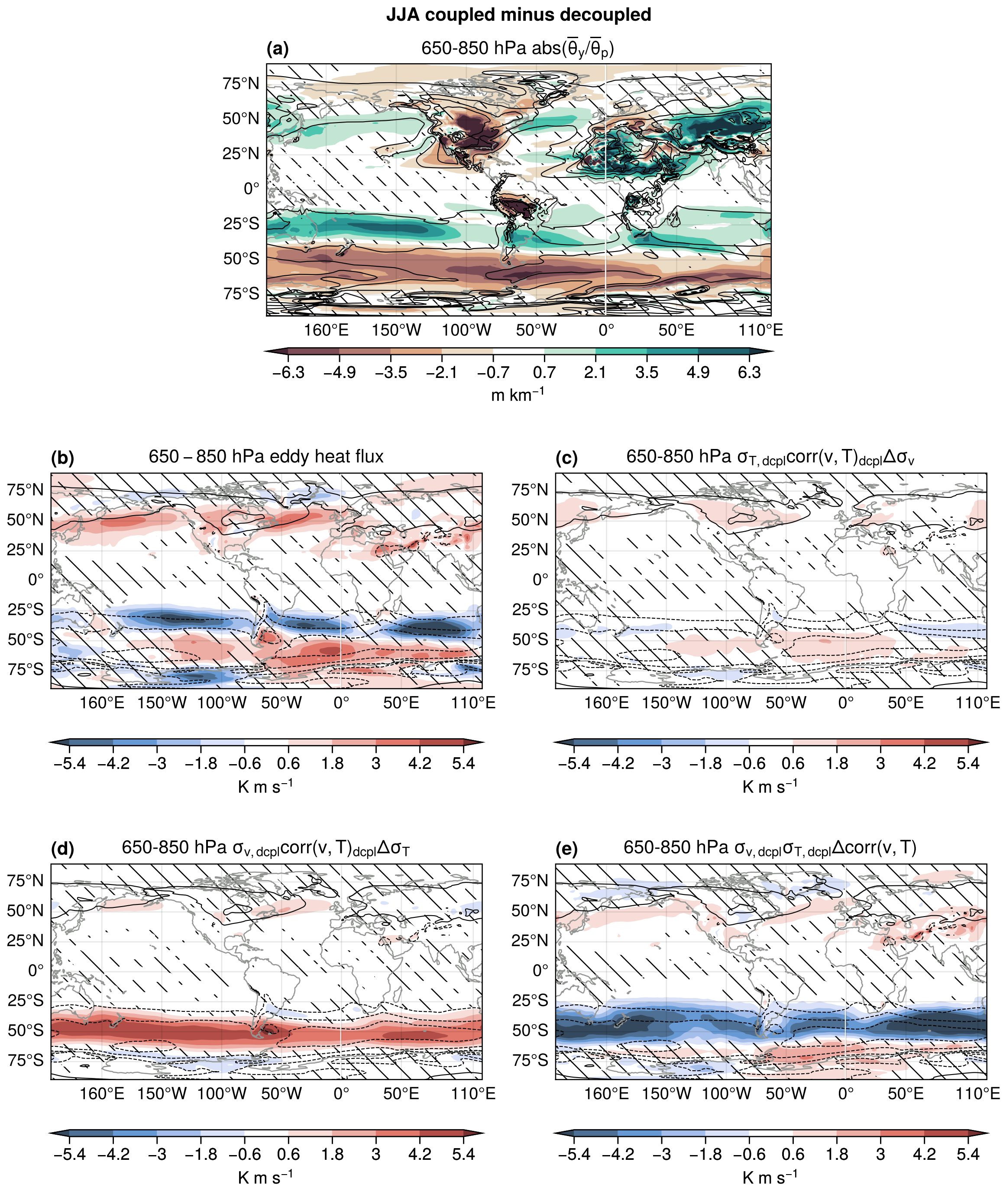

Figure B.2: Like Fig 4.3, without panel b and c in Fig 4.3.

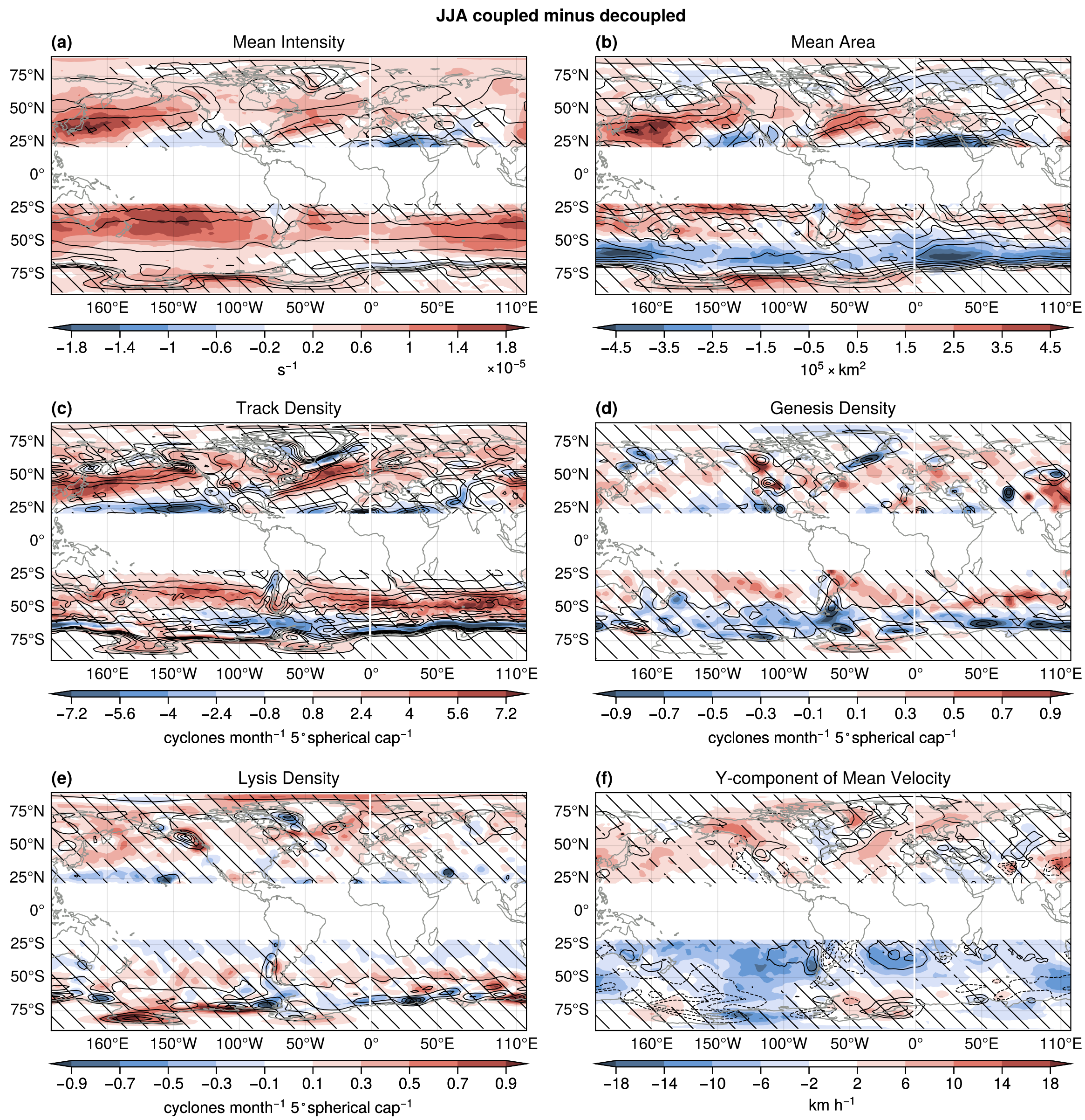

Figure B.3: Like Fig 4.4.

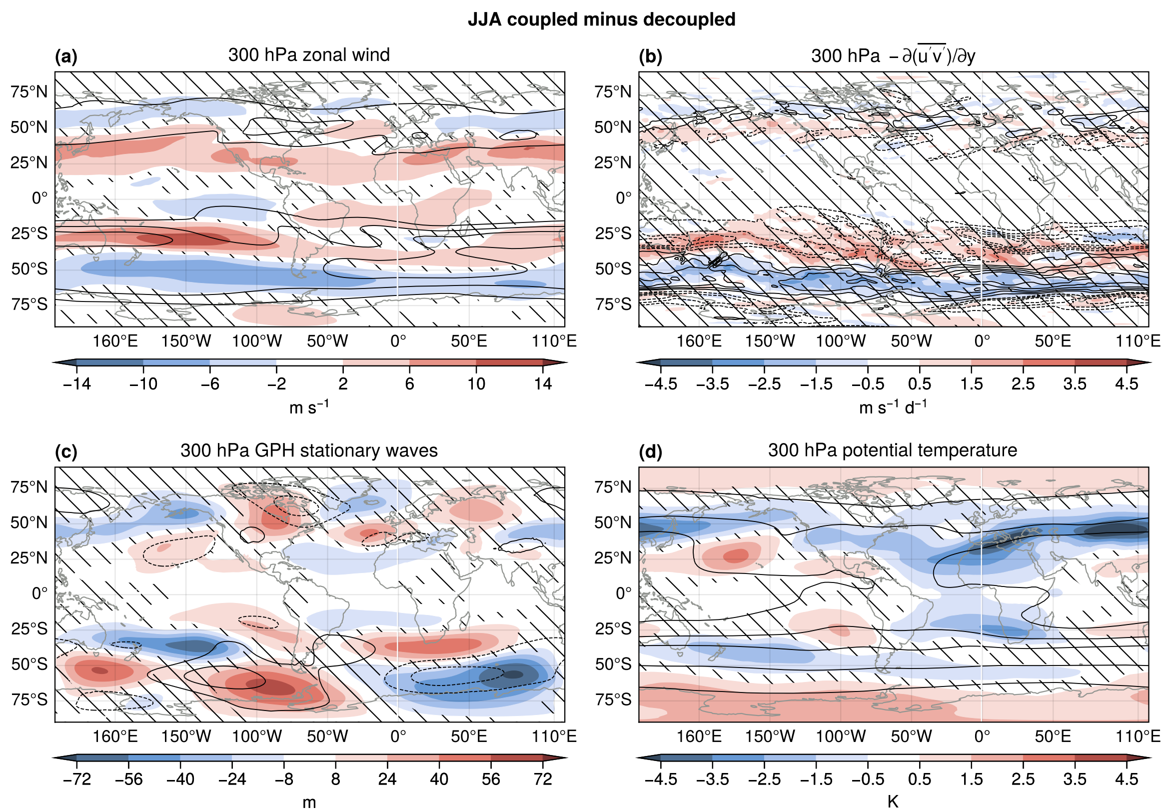

Figure B.4: Like Fig 4.5.

B.2 Zonal mean heat budget

Following Lachmy and Kaspi (2020), Figs. B.5–B.6 show diabatic and advection terms from the zonal mean temperature budget, as well as zonal wind differences for December, January, and February and June, July, and August, respectively.

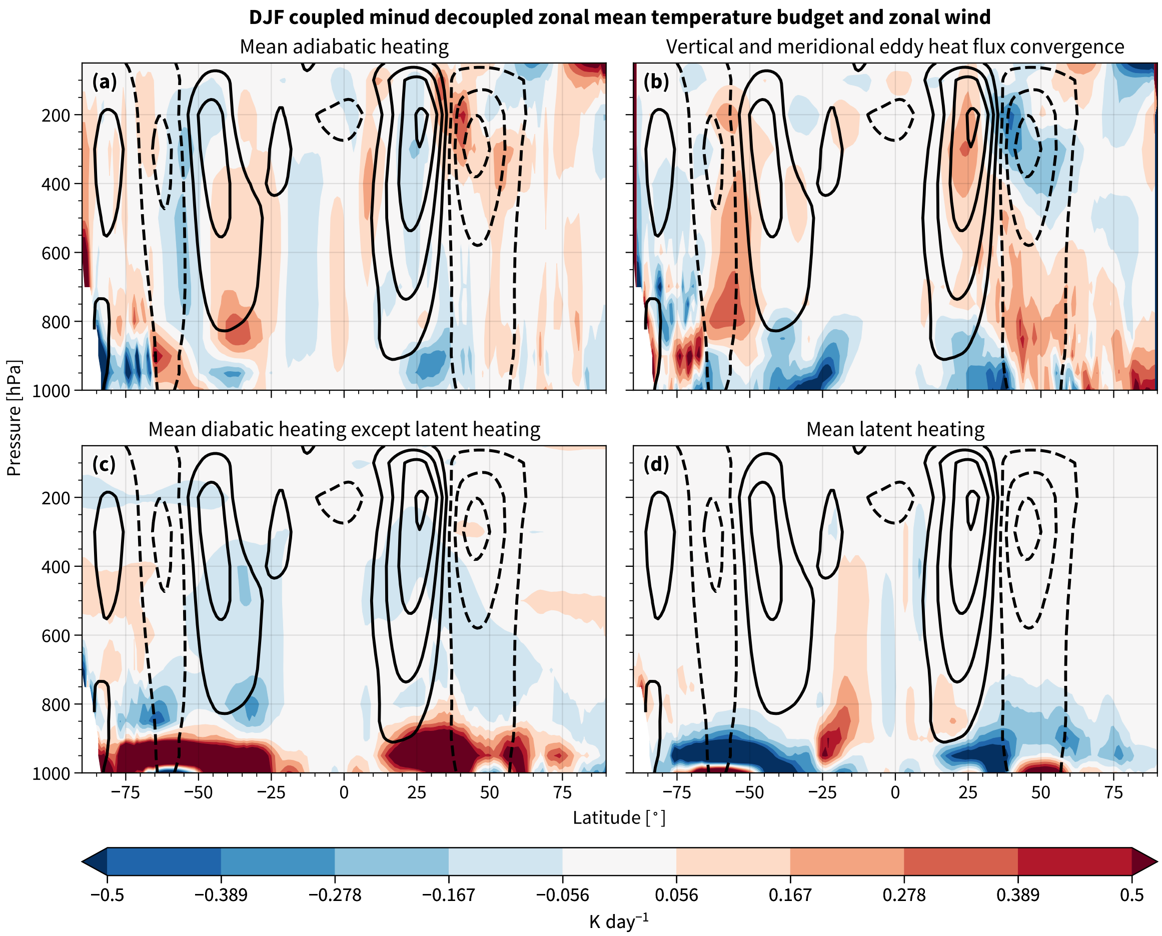

Figure B.5: Coupled minus decoupled zonal mean temperature budget in shading and zonal wind in contours at levels -7,-5, ..., 7 m/s. Values are from December, January, and February.

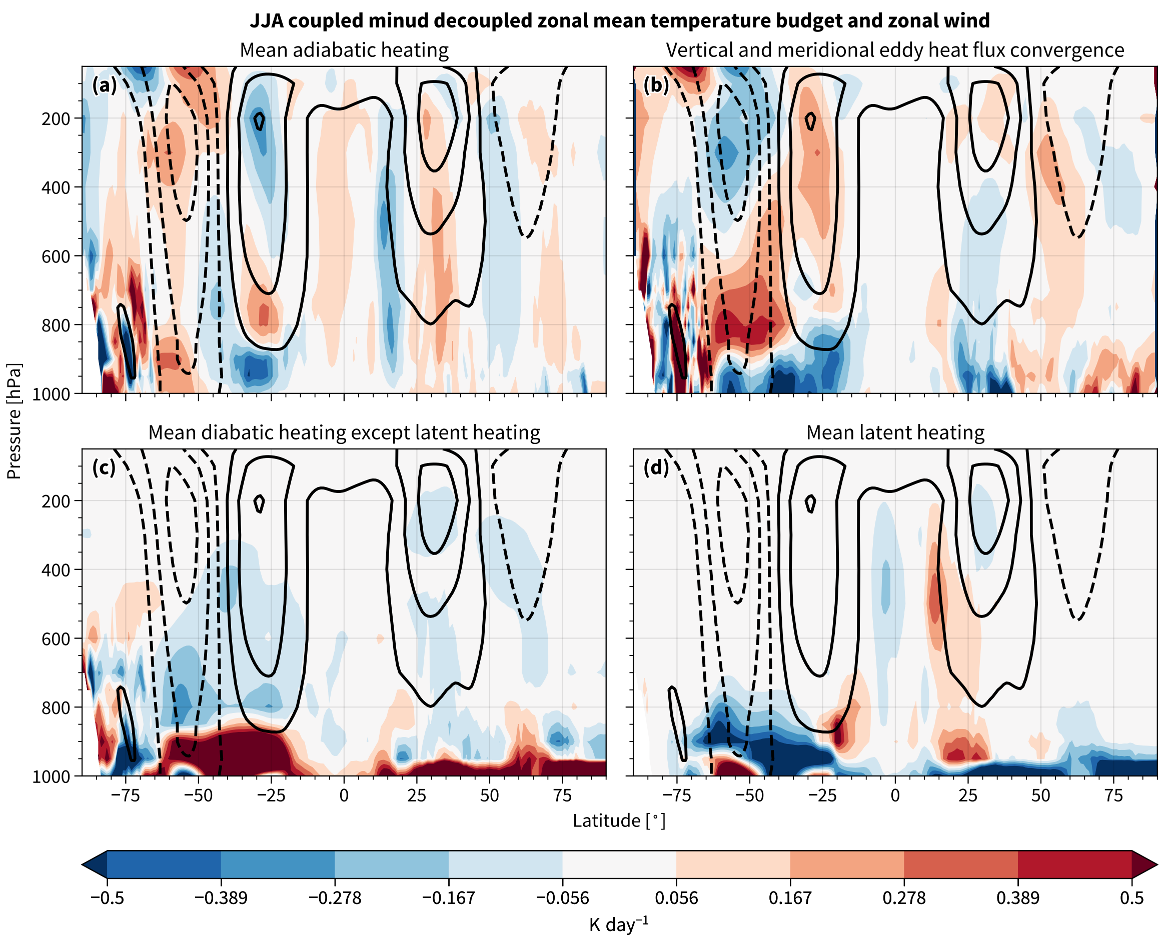

Figure B.6: Like Fig. S5 but showing values for June, July and August.